TECHNISCHE UNIVERSITÄT
CHEMNITZ

Micro and Nano Raman Investigation of Two-Dimensional Semiconductors towards Device Application

von der Fakultät für Naturwissenschaften der Technische Universität Chemnitz

Dissertation

Zur Erlangung des akademischen Grades

doctor rerum naturalium

(Dr. rer. nat.)

vorgelegt

der Fakultät für Naturwissenschaften der Technische Universität Chemnitz

von M. Sc. Mahfujur Rahaman

geboren am 21. Oktober 1985 in Chandpur, Bangladesch

Chemnitz den. 13.02.2018

Dedicated to my parents

Bibliographische Beschreibung und Referat

Inspiriert durch den großen Erfolg von Graphen haben zweidimensionale Halbleiter als neue Materialien für Bauelementanwendungen erneutes Interesse gefunden. Diese Materialien besitzen einzigartige und bemerkenswerte elektronische und optische Eigenschaften. Ihre starke In-Plane-Bindung und schwache Out-of-Plane-Wechselwirkungen ermöglichen die Herstellung einer einzelnen Atomschicht. Jüngste Fortschritte in der Charakterisierung und Herstellung von Nanostrukturen haben Möglichkeiten für Schicht-Halbleiter in der Nanoelektronik und Optoelektronik eröffnet. Aufgrund der starken Einschließung in der Schichtdicke werden die physikalischen Eigenschaften dieser Materialien stark von Parametern wie Dehnung, Defekten und Dotierung im Nanometerbereich beeinflusst. Daher ist das Verständnis der Auswirkungen dieser Parameter auf geschichtete Halbleiter die Voraussetzung für jede Geräteanwendung.

In dieser Doktorarbeit wird der Einfluss solcher Parameter auf die optischen Eigenschaften von Schichthalbleitern im Nanometerbereich untersucht. MoS_2, das bekannteste Übergangsmetall- Chalkogenide (TMDC) (n-Typ-Halbleiter), und p-Typ-GaSe, ein Vertreter der Metallmonochalkogenide (MMC), werden in dieser Arbeit untersucht.

Eine detaillierte Einführung in beide Materialien, einschließlich ihrer polytypischen, elektrischen und optischen Eigenschaften, wird im einführenden Kapitel dieser Arbeit behandelt.

p-Typ GaSe hat ein großes Potenzial auf dem Gebiet der Optoelektronik, nichtlinearer Optik und Terahertz-Anwendungen. Die Vergänglichkeit von atomarem dickem GaSe in Luft behindert jedoch den Forschungsfortschritt. Über die Umweltstabilität des Materials ist jedoch wenig bekannt.

Diese Arbeit befasst sich mit der Frage der Stabilität von GaSe in der Umwelt mittels Raman-Spektroskopie, Photolumineszenz und Röntgenphotoelektronenspektroskopie. Die Ergebnisse sind für die Anwendung der Vorrichtung sehr wichtig, da eine Monolage von GaSe unmittelbar nach dem Aussetzen an Luft oxidiert wird und sich mit der Zeit bis zu drei Schichten abbaut. Daher muss für die technologische Anwendung die oxidierende Dicke von GaSe berücksichtigt werden. Ein Teil dieser Arbeit kann in ***Semicond. Sci. Technol. 32 (2017) 105004*** gefunden werden.

Da bekannt ist, dass TMDCs großen Belastungen standhalten (6-11%), ist es vorteilhaft, diese Materialien für flexible optoelektronische Bauelemente der nächsten Generation zu betrachten. Des Weiteren zeigen MoS_2 starke spannungsabhängige optoelektronische Eigenschaften und wurden von mehreren Gruppen im Makro- und Mikrobereich untersucht. Insbesondere für die Nanotechnologie ist es jedoch notwendig, die eingebaute Dehnung im Nanometerbereich zu kennen. In dieser Arbeit wurde mit Hilfe der spitzenverstärkten Raman-Spektroskopie eine hoch

lokalisierte Dehnung in dreilagigem MoS_2 innerhalb der räumlichen Auflösung von nur 25 nm nachgewiesen. Ein Teil der Arbeit kann in ***Nano Lett. 17 (2017) 6027*** gefunden werden.

Die Untersuchung lokaler Heterogenitäten wird mit Hilfe des in dreilagigen MoS_2 gewonnenen Wissens auf Monolagen ausgedehnt. Monolagiges MoS_2 ist ein Halbleiter mit direkter Bandlücke und großer Exzitonenbindungsenergie. Aufgrund seiner starken Wechselwirkung mit leichten Materialien ist es eine ideale Plattform, um die optischen Eigenschaften von 1L-MoS_2 in einer Umgebung lokalisierter Oberflächenplasmonresonanz zu untersuchen, die von Metallnanopartikeln aufrechterhalten wird. Insbesondere, wie MoS_2 mit den von LSPR erzeugten Hotspots interagiert. Um solche Phänomene zu untersuchen, wird 1L-MoS_2 mit einem geeigneten plasmonischen Substrat aus Gold-Nanozylinders auf Silizium kombiniert.

Spitzenverstärkte-Raman-Spektroskopie wird angewandt, um die Phononenmodi von MoS_2 zu untersuchen. Im Raman-Mapping mit einem Verstärkungsfaktor von 10^8 wird eine räumliche Auflösung von 2.3 nm erreicht. Eine solche experimentelle Auflösung und Bildqualität ermöglicht einen beispiellosen Zugang zu den Hotspots, was zu einer Dotierung in 1L-MoS_2 in der Größenordnung von 10^{13} und der Strukturphase führt Wechsel von Halbleiter zu Leiter. Die Ergebnisse der Studie können für die grundlegende Untersuchung und Anwendung von 2D-Materialien wichtig sein. Insbesondere kann die durch Dotierung induzierte strukturelle Phasenänderung für die Anwendung der Bauelemente entscheidend sein. Ein Teil der Arbeit kann in ***Nanoscale, 10 (2018), 2755*** gefunden werden.

Schließlich wird im Ausblick eine Vorrichtung aus GaSe vom p-Typ mit wenigen Schichten und 1L-MoS_2 vom n-Typ diskutiert. Der Heteroübergang zeigt ein sehr gutes Rektifikationsverhältnis von 10^4 bei ± 1 V. Jedoch zeigt der Heteroübergang bei Beleuchtung mit unterer Bandlückenanregung einen photovoltaischen Effekt und deutet auf einen durch die Zwischenphase unterstützten Photostrom hin. Um den Transportmechanismus und den Ursprung des Photostroms zu verstehen, müssen temperaturabhängige I - V - Messungen und theoretische Berechnungen der Bandstruktur des Heteroübergangs durchgeführt werden.

Schlagwörter: Two dimensional materials, MoS_2, GaSe, tip enhanced Raman spectroscopy, TERS, plasmonics, environmental stability, oxidation, strain, doping.

Table of Contents

Abbreviation 11

List of figures 13

1. Introduction 15

2. An overview of crystal: electronic properties and preparation 19

2.1. Gallium Selenide (GaSe) 19

2.2. Molybdenum Disulfide (MoS_2) 21

2.3. Methods of Preparation 24

3. Experimental Methods 27

3.1. Atomic force microscopy (AFM) 27

3.2. Raman spectroscopy 30

3.3. Tip-enhanced Raman spectroscopy (TERS) 37

3.4. X-ray photoelectron spectroscopy (XPS) 38

4. Environmental stability of GaSe 41

4.1. Introduction / Motivation 41

4.2. Experimental details 42

4.3. Raman signatures of oxidation in bulk GaSe 43

4.4. Laser induced surface deformation of GaSe 44

4.5. Environmental stability of monolayer GaSe 47

4.6. Time evolution of GaSe oxidation 47

4.7. Time dependent photoluminescence 51

4.8. Imaging XPS study of oxidation in GaSe 52

4.9. Summary 54

5. TERS study of local heterogeneities of MoS_2: strain 55

5.1. Introduction / Motivation 55

5.2. Theoretical background of TERS 56

5.3. Experimental details 63

5.4. AFM study of the heterostructure 68

5.5. TERS imaging of the heterostructure 69

5.6. Investigation of localized strain 73

5.7. Influence of local heating in TERS spectra 77
5.8. Summary 79

6. TERS study of local heterogeneities of MoS_2: strain, and doping 81
6.1. Introduction / Motivation 81
6.2. Experimental details 83
6.3. Preparation of TERS tips 86
6.4. Morphology study of the heterostructure 89
6.5. Micro Raman study of the heterostructure 89
6.6. TERS imaging of the heterostructure 90
6.6.1 Determination of spatial resolution 92
6.6.2 Determination of enhancement factor 94
6.7 Investigation of local heterogeneities 96
6.8 Summary 99

7. Summary 101

Outlook 102

Appendix 105

Bibliography 109

Acknowledgements 135

Lebenslauf 136

Publications 137

Erklärung 139

Abbreviations

2D: Two dimensional

AFM: Atomic force microscopy

ALD: Atomic layer deposition

APD curve: Amplitude, phase vs distance curve

BZ: Brillouin zone

CVD: Chemical vapour deposition

EM: Electromagnetic

EMCCD: Electron multiplying charge coupled device

FEM: Finite element method

FWHM: Full width at half maximum

GaSe: Gallium selenide

HOPG: Highly ordered pyrolytic graphite

LA: Longitudinal acoustic

LSPR: Localized surface plasmon resonance

MBE: Molecular beam epitaxy

MMC: Metal monochalcogenide

MOCVD: Metal-organic chemical vapour deposition

MoS_2: Molybdenum disulphide

NC: Nanocylinder

NT: Nanotriangle

PDMS: Polydimethylsiloxane

PL: Photoluminescence

PS: Polystyrene sphere

SEM: Scanning electron microscopy

SERS: Surface enhanced Raman scattering

SOC: spin-orbit coupling

SOD: Second-order derivative

TERS: Tip enhanced Raman scattering/spectroscopy

TMDC: Transition metal dichalcogenide

vdW: van der Waals

XL (X= 1, 2, 3…): X layer

XPS: X-ray photoelectron spectroscopy

List of figures

Figure 2.1: Crystal structure of GaSe

Figure 2.2: Crystal structure of MoS_2

Figure 2.3: Schematic of mechanical exfoliation

Figure 3.1: Schematic of AFM

Figure 3.2: Simulation of force *vs* distance and APD curve

Figure 3.3: Schematic representation of Raman scattering process

Figure 3.4: Description of Raman spectrometer

Figure 3.5: Illustration of TERS principle

Figure 3.6: Sketch of photoemission process involved in XPS

Figure 4.1: Raman signatures of oxidation in bulk GaSe: role of excitation wavelength

Figure 4.2: Laser power dependent surface stability of GaSe

Figure 4.3: Raman spectra of monolayer GaSe

Figure 4.4: AFM topography and phase image of eight-layer GaSe

Figure 4.5: Time evolution study of oxidation of eight-layer GaSe using Raman spectroscopy

Figure 4.6: Penetration depth of oxidation in GaSe studied by Raman spectroscopy

Figure 4.7: AFM topographies and profiles of the flakes used in Figure 4.6

Figure 4.8: Time dependent PL of GaSe

Figure 4.9: Imaging XPS investigation of oxidation in trilayer GaSe (O1s peak)

Figure 4.10: Imaging XPS investigation of oxidation in trilayer GaSe (Ga 3d and Se 3d peak)

Figure 5.1: FEM simulation of plasmonic enhancement at the Au tip apex

Figure 5.2: FEM simulation of plasmonic enhancement in a gap-mode TERS configuration

Figure 5.3: FEM simulation of tip-sample distance *vs* local field enhancement

Figure 5.4: SEM and AFM topography of Au NTs

Figure 5.5: Illustration of mechanical exfoliation and AFM topography image of MoS_2/Au NTs heterostructure

Figure 5.6: Determination of the thickness of MoS_2 using micro-Raman spectra

Figure 5.7: TERS schematic and polarisation dependent local field confinement at the Au tip apex

Figure 5.8: determination of the spectral resolution of TERS experiments

Figure 5.9: AFM topography of the MoS_2/Au NTs heterostructure for the thickness determination of the flake

Figure 5.10: TERS map of one hexagonal unit of the MoS_2/Au NTs heterostructure and determination of spatial resolution of the measurements

Figure 5.11: FEM modelling of the experimental system for the calculation of TERS enhancement

Figure 5.12: Determination of local strain in MoS_2 using TERS: TERS spectra vs local areas

Figure 5.13: Determination of local strain in MoS_2 using TERS: fitted peak position of TERS modes vs local areas

Figure 5.14: Investigation of local strain distribution in MoS_2: local curvature image of the hexagonal unit of the MoS_2/Au NTs heterostructure studied in Figure 5.10

Figure 5.15: Investigation of local strain distribution in MoS_2: TERS spectra vs local areas (taken from local curvature image)

Figure 5.16: Temperature dependent Raman study of trilayer MoS_2

Figure 6.1: SEM and AFM topography images of Au NCs

Figure 6.2: AFM topography of monolayer MoS_2/Au NCs heterostructure

Figure 6.3: Confirmation of monolayer thickness of MoS_2 using micro-Raman and PL

Figure 6.4: Schematic of TERS

Figure 6.5: SEM images of Au tips used in TERS experiments

Figure 6.6: FEM simulation of Au tip radius dependent local electric field enhancement in gap-mode TERS configuration

Figure 6.7: Magnified SEM and AFM topography images of monolayer MoS_2/Au NCs heterostructure showing local deformation of the flake

Figure 6.8: Comparison of micro-Raman and TERS spectra of MoS_2/Au NCs heterostructure

Figure 6.9: Extended TERS image of MoS_2/Au NCs heterostructure

Figure 6.10: TERS image of monolayer MoS_2 on top of single NC for the determination of spatial resolution

Figure 6.11: FEM simulation of TERS enhancement of the experimental system

Figure 6.12: Determination of local strain, temperature rise and doping in monolayer MoS_2 using TERS

Figure 6.13: Demonstration of semiconducting to metallic transformation of monolayer MoS_2 due to plasmonic hot electron doping

Figure I: Demonstration of the formation of ultra-thin vertical p-n junction between p-type GaSe and n-type MoS_2

Chapter 1

Introduction

Layered materials are known to exist for billions of years and the history of the scientific research of them is about 150 years old.[1-3] However, it is only in the last decade the true potentials of these systems have been realized for advanced technological applications and the study of these materials has been speeded up.[4-9] The beauty of these layered systems is that when thinned down to their true physical limit (monolayer) each material shows unique / novel physical properties different from their bulk counterpart.[10-12] At their ultimate physical limit they are called two dimensional (2D) materials. Since Novesolov and Geim [4, 13] first successfully exfoliated graphene from graphite in the lab in 2004, it is the most studied 2D material mainly because of its extraordinary electronic or optoelectronic properties.[14-17] The biggest advantage of graphene is its ballistic conductivity with a mobility of 10^5 $cm^2/v.s$.[18] However, the main drawback of this material is the absence of a band gap which hinders graphene to be used in transistors, logic gates or any other semiconductor device as the active material. There are several experimental and theoretical studies so far reported on opening the band gap in graphene.[19-21] However, that became only successful with significant decrease in the mobility (200 $cm^2/v.s$ for 150 meV bandgap).[20, 22] Additionally the increase in off-state current due to edge roughness and loss of coherence also deteriorates the device performance as a consequence.[23-24] Following graphene, another 2D material, hexagonal boron nitride (hBN) grabbed the attention since it was theoretically predicted to induce band gap in graphene.[25-27] hBN has a band gap of about 6 eV[28] and therefore the only possible application of it is as gate insulator in a 2D device. This led to searching for 2D semiconductors which could have reasonable band gap and at the same time possess higher mobility as well. Rapidly following graphene and hBN, there is a special set of layered semiconductors which show a drastic change in band structures while thinned down to monolayer thickness and therefore brought further excitement.[29-30] This special set of materials are known as transition metal dichalcogenides (TMDC) and are now the primary focus of the research in 2D materials field. However, most of the TMDCs found in nature are intrinsically n-type semiconductors due to the presence of chalcogen vacancies.[31] For a semiconductor device application, the p-n junction is a fundamental building block. Although engineering extrinsic factors to achieve p-type conductivity in this materials have been demonstrated by several groups, obtaining high quality p-type ultra-thin film is very challenging.[31-34] Beyond TMDCs, there are other layered semiconductors like metal monochalcogenides (MMC) such as GaSe, GaS, InSe and

InS *etc.* which also have induced growing interest in recent times owing to their optoelectronic properties which can be tuned with the layer thickness.[35-38] Importantly, both GaSe and GaS are intrinsically p-type semiconductors due to the presence of lower lying defects states associated with Se vacancies.[39-40] These shallow defects states create an acceptor level lying 0.2 eV (approximately) above the top of the valance band. Therefore, they can provide a great platform to fabricate p-n van der Waals (vdW) heterojunctions to explore the potential in device application. Apart from these binary layered materials there are some monoelemental 2D semiconductors like silicene, phosphorene and germanene also getting attraction in the 2D research community.[41-43] However, the environmental stability of this monoelemental materials is the biggest challenge which hinders the extensive research of these materials.[44-45] This thesis work is devoted to investigating the properties of n-type MoS_2 (a member of TMDCs) and p-type GaSe (a member of MMCs) towards realizing a 2D p-n junction.

TMDCs have sizable band gap. These materials have excellent tuneable electronic and optical properties, high mechanical strength and chemical and thermal stability which offer a variety of applications.[30, 46-48] Among all TMDCs, MoS_2 is one of the most studied materials. It has an indirect band gap of 1.2 eV in bulk which is increased to a direct band gap of 1.8 eV in the monolayer.[46] This unique physical phenomenon of indirect to direct band gap transition yields a high photoluminescence efficiency and opens the door for various optoelectronic applications.[49-52] The field effect mobility of MoS_2 monolayer is determined to be 200 $cm^2/v.s$ at room temperature,[30] comparable to the mobility achieved for ultra-thin silicon films.[53-54] Another interesting application of MoS_2 and other TMDCs monolayer is in valleytronics.[55-56] The conduction band minima of these materials has two extremes at equal energies located at K and K′ points but at different positions in momentum space. Moreover, very strong spin-orbit coupling (SOC) splits the valance band edge to two sub-bands well-known as A and B bands containing electrons with opposite spins. Therefore, by controlling the valley polarization one can control the occupation of electrons in these valleys.

Like TMDCs, GaSe was also predicted to show thickness dependent optoelectronic properties such as non-linear optical emission[57] and band gap changing from 2 eV (bulk) to 4 eV (monolayer). [58] Therefore it provides a pathway towards novel responses emerging from heterostructures made of monolayers such as high performance hyperspectral emitters and photodetectors spanning from ultraviolet (UV) to the visible range.[59-60] Moreover, large and fast photoresponse was demonstrated in photodetectors fabricated from monolayer/ultrathin GaSe, as well as tunable heterojunctions with graphene.[35-36, 61]

A very recent trend in 2D materials research is combining them with plasmonic structures (metal nano particles, spheres, cavities etc.).[62-67] The localized surface plasmon (LSP) of plasmonic surfaces is known for its outstanding light trapping and electric field enhancement. As

demonstrated in recent years, the LSP of a nanostructure (also known as dipole oscillation) is used to increase the efficiency in energy harvesting, [68] photodetection, [69] photoctalysis, [70] waveguides[64] etc. when integrated with 2D materials. Plasmonic hot electrons are also known to dope and control the exciton binding energy of TMDCs. [67]

In ***Chapter 2***, the materials under investigation are introduced. An overview of their crystallography, group theory, Raman bands, and electronic properties are discussed. In ***chapter 3***, the experimental methods used in this thesis work are discussed. In ***chapter 4***, the environmental stability of GaSe, an important aspect of a practical device is addressed. The oxidation phenomena are investigated by monitoring the Raman bands of GaSe and its by-products in real time. The Raman findings are then compared with photoluminescence and X-ray photoelectron spectroscopy results. In ***chapter 5***, localized strain in a 3L-MoS_2/Au nanostructured system created during heterostructure fabrication is studied by tip-enhanced Raman scattering (TERS). Electronic properties of MoS_2 are reported to be very sensitive to applied strain.[71] Therefore, built-in strain at the nanoscale would influence the device performance (especially for nano-electronics). ***Chapter 6*** deals with heterogeneities of monolayer MoS_2 highly localized in a 2D/plasmonic heterostructure. With the aid of TERS, the influence of strain, doping, and heating on phonon properties 1L-MoS_2 is discussed. The effects are directly correlated to electrical and other optical properties of MoS_2. Finally, in the ***outlook***, the potential of a 2D p-n junction is addressed with future perspective in terms of fundamental studies and device application.

Chapter 2

An overview of crystal: electronic properties and preparation

The materials under investigation will be introduced in this chapter. Geometry, group theory, and electronic properties are reviewed for understanding the optical properties of the materials. The role of non-covalent interactions between the layers in the physical properties of the materials is discussed. There is a brief discussion of the methods of preparation of monolayer and multi-layer flakes at the end of this chapter.

2.1: Gallium Selenide (GaSe)

GaSe is a layered III-VI semiconductor (also known as metal monochalcogenide, MMC; or MX with M = Ga, In; X = S, Se, Te). Monolayer GaSe consists of covalently bonded stack of four atomic layers in which, two Ga atoms are sandwiched by two Se atoms in a sequence of Se-Ga-Ga-Se with a lattice constant of 0.374 nm and a thickness of 0.98 nm.[36, 72] Layers of GaSe are held together by a weak van der Waals force. Therefore, it is possible to prepare a single layer by simple mechanical exfoliation in a similar fashion as performed for graphene and other 2D materials. This material has received a growing interest due to its reduced dimensionality and attractive optoelectronic properties. Due to the absence of an inversion symmetric center in bulk GaSe, it shows nonlinear optical behavior and is used in second and third harmonic generation (SHG or THG) by several groups.[73-77] GaSe is also known to show strong photoresponse and therefore has potential in optoelectronics,[35-36, 78-79] photonics,[59, 80-81] and sensors applications.[82-83]

The stacking sequence of the four atomic layers named tetra-layers (TLs) determines the polymorphs of GaSe. There are four different crystalline polytypes for bulk GaSe: β-GaSe, γ-GaSe, δ-GaSe, and ε-GaSe.[35, 84] These crystalline structures are formed from the fundamental layer building block leading to different symmetry groups (β-GaSe: D_{6h}, γ-GaSe: C_{3v}, δ-GaSe: C_{6v}, and ε-GaSe: D_{3h}).[72, 85] Among these polytypes, γ-GaSe has a 3R stacking sequence. Whereas, both β-GaSe and ε-GaSe are hexagonally symmetric with a stacking sequence of 2H. The notations 3R and 2H represent the rhombohedral (C_{6v}^4 group) and hexagonal (D_{3h}^1group) crystal symmetry

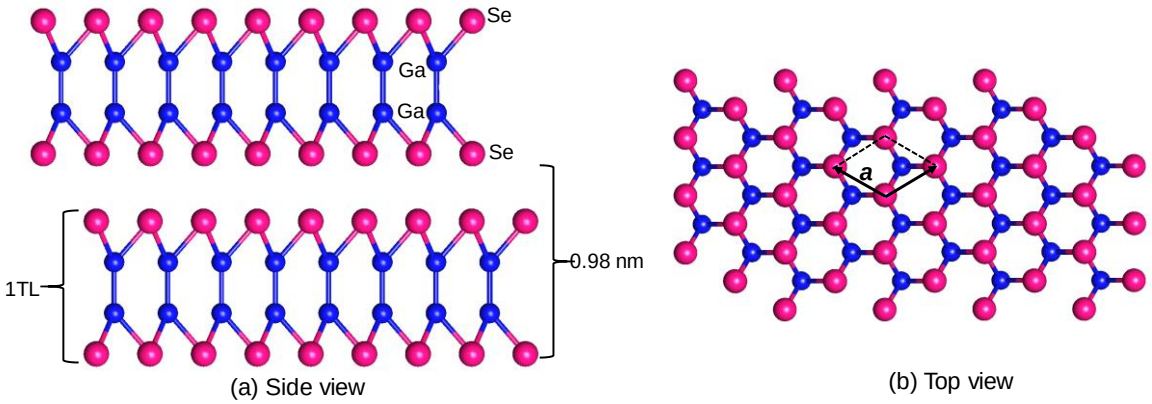

Figure 2.1: Crystal structure of ε-GaSe. (a) side view and (b) top view. Lattice constant $\boldsymbol{a}$ = 0.374 nm. A sequence of Se-Ga-Ga-Se forms one tetra-layers (1 TLs). Thickness of 1 TLs is 0.98 nm.

respectively; whereas, the number 3 and 2 stand for the number of layers in the crystallographic unit cell. There are two TLs in one-unit cell of 2H-GaSe. In β-GaSe, the second TLs is formed by rotation of the first TLs. In case of ε-GaSe, the modification is generated by translation of the basic TLs. In this thesis work, ε-GaSe grown by the Bridgman technique is used. The material was kindly provided by Professor Santos A. Lopez of the University of the Andes, Venezuela.

ε-GaSe is the main polytype formed during Bridgman or melting technique[39, 86-87] and has a direct band gap of (2.0 - 2.1) eV.[39, 72, 88-90] Figure 2.1 shows the typical hexagonal crystal structure of ε-GaSe. It is naturally a p-type semiconductor due to the native defects such as Se vacancies, interstitial Se atoms, Ga atoms on Se sites and external impurities such Cu and interstitial O atoms introduced during crystal growth.[39, 91] Like TMDCs GaSe is also known to show layer dependent electronic properties. In bulk it has an indirect band gap of about 25 meV below the direct band edge.[72, 89] Therefore, it is possible to transfer electrons easily between the two energy levels at room temperature. However, once the thickness is thinned down to monolayer the band gap of GaSe increases.[92] The indirect band gap of monolayer GaSe varies from (3 – 4) eV depending on the computational method[58, 93] and summarised in the literature.[72] The trend is opposite to what is observed for TMDCs. Experimental determination of the band gap of monolayer GaSe has not yet been reported from typical optical measurements. The challenge impeding such experiments is discussed in Chapter 4. The exciton binding energy in bulk GaSe is reported to be in the range of 20 meV.[73, 89] The acceptor concentrations in GaSe (both parallel and perpendicular to the crystal axis *c*) are in the range of 10^{16} cm^{-3}.[94-95] The hole mobility of bulk GaSe is reported to be in the range of (20 – 215) $cm^2 \cdot V^{-1} \cdot s^{-1}$.[39, 90, 95-96] However, compared to TMDCs, the mobility of monolayer

(0.6 $cm^2 \cdot V^{-1} \cdot s^{-1}$) and few layer (0.005 $cm^2 \cdot V^{-1} \cdot s^{-1}$) GaSe decreased drastically as reported by several groups.[72, 83, 97] This drastic change in mobility in monolayer or few layers was explained by several factors such as traps and impurities present in the gate oxide and instability of GaSe surface in air. Electrons can scatter in the traps and impurity states present at the interface and therefore degrade the mobility of the channel material. However, the instability of the atomically thin GaSe film in air due to oxidation,[98] can be the major factor for such drastic decrease in mobility of the charge carriers and is the subject of discussion in Chapter 4.

2.2: Molybdenum disulphide (MoS_2)

MoS_2 is a member of layered TMDC semiconductor. The generalized formula of TMDC is MX_2, in which M stands for transition metal from group 4 – 10 (most famous are Mo and W) and X stands for chalcogen (S, Se, or Te). TMDCs formed from group 4 – 7 are predominantly layered and those from group 8 – 10 are commonly found in non-layered structure.[99] Following the footsteps of graphene, (which does not have a band gap) TMDCs are the most extensively studied layered materials[3, 18, 26, 42, 54, 63, 66, 100-104] due to their unique physical properties.[12, 29, 46, 66, 105] Among all, MoS_2 is at the top of the material list due to its availability, distinctive physical properties, and stability in air.[30, 106-107]

Like graphene, MoS_2 has a hexagonal crystal structure. Each layer consist of hexagonally packed Mo atoms sandwiched by two S atoms in a sequence of S – Mo – S (tri-atomic layer). Intra-layer Mo – S bonds are covalent and inter-layer S – S atoms are coupled by a weak van der Waals force thus allowing the material to be cleaved layer by layer. The thickness of each layer is in the range of 0.6 - 0.7 nm. In bulk, MoS_2 can have three different polymorphs: 1T, 2H, and 3R referred to trigonal, hexagonal, and rhombohedral phase, respectively.[99] The digits corresponds to the number of tri-atomic layers in a particular phase. However, in monolayer, MoS_2 only has trigonal prismatic or octahedral phase. The former polymorph is the semiconducting, also known as 1H-MoS_2 and the later one is the metallic phase known as 1T-MoS_2. The metallic 1T-MoS_2 is a metastable state which relaxes to the thermodynamically stable 1H or 2H-MoS_2.The symmetry space group of bulk 2H-MoS_2 is $P6_3/mmc$ (corresponds to the point group of D_{6h}). Once thinned down to monolayer, the inversion symmetry is lifted and it belongs to the space group of *P6m2* (corresponds to the point group of D_{3h}).[99, 108] The octahedral phase of monolayer MoS_2 belongs to the point group of D_{3d}. The hexagonal crystal structure of MoS_2 is displayed in Figure 2.2. It should be noted that semiconducting 1H-MoS_2 is the main focus of the research activities. Nevertheless, the phase transition from semiconductor to metal also has potential applications in electronic devices to reduce the junction resistance.[109-112] Phase transition can be induced via chemical doping or strong hybridization with a metal substrate. However, a new route of semiconductor to metal phase transition via plasmonic hot electron doping will be discussed in Chapter 6.

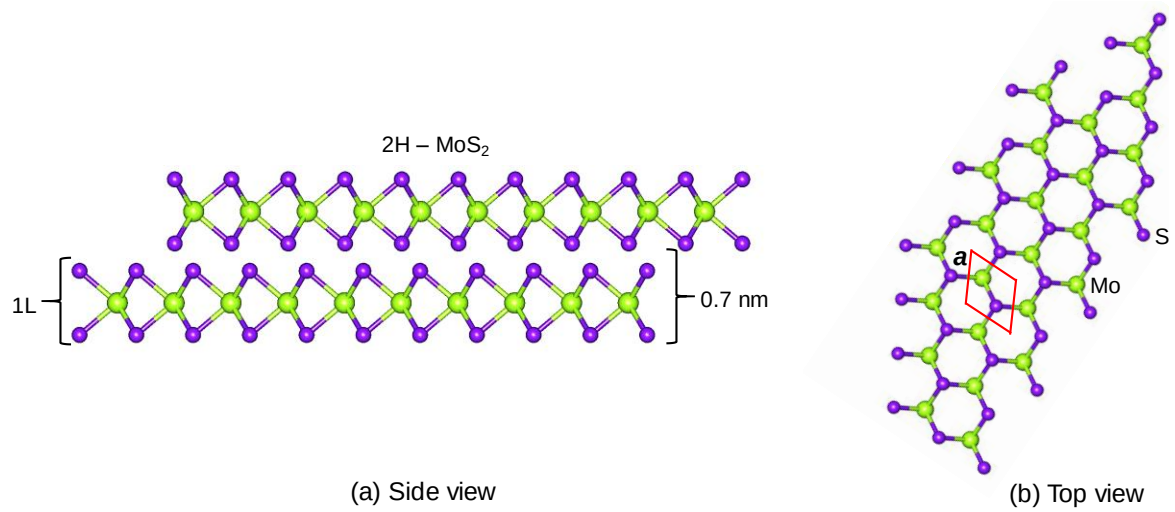

Figure 2.2: Crystal structure of 2H-MoS_2. (a) side view and (b) top view. Lattice constant $\boldsymbol{a}$ = 0.315 nm. A sequence of S-Mo-S forms one monolayer (1L). Thickness of 1L is 0.6 - 0.7 nm.

The unique physical characteristic of MoS_2 is the tuneable optoelectronic properties with respect to thickness. Bulk MoS_2 is an indirect band gap semiconductor with a value in the range of 1.3 eV. However, when thinned down to monolayer, the nature of the optical band gap becomes direct and the band gap increases to 1.9 eV, as demonstrated by experiments and supported by ab initio calculation in recent years.[46, 113-116] As predicted by ab initio calculation, the valence (conduction) band maximum (minimum) of bulk MoS_2 located at the Γ (Q) point of the Brillouin zone, where

Brillouin zone[i-iv]: The most important characteristic of a crystal is its invariance under certain translational, rotational, and reflection symmetries such that it can be represented as a periodic function of a certain operator called unit cell or primitive cell. The first Brillouin zone (or Brillouin zone, BZ) is the Wigner-Seitz primitive cell of the reciprocal lattice. It plays a major role in the theoretical understanding of the electronic band structure or phonon states in a material. The reason of introducing the reciprocal lattice is to represent the wavevector, $\boldsymbol{k}$ as a point in reciprocal space. The boundaries of this cell are defined by set of planes related to the points in reciprocal space known as Bragg planes. Since crystals are highly symmetric, the notion of BZ is often expanded to n-th BZ (BZ with a periodicity n) to describe the phonon or electronic states in a system.

The 1st BZ is expanded from $-\pi/a$ to π/a (a is the lattice constant in one dimension) such that BZ periodicity is given by $2\pi/a$. While, three dimensional BZ is expressed in terms of a set of primitive cell vectors: $\boldsymbol{a}$, $\boldsymbol{b}$, and $\boldsymbol{c}$. The center of the BZ (denoted by Γ) is surrounded by several high symmetry points also known as critical points. The number and the types of critical points vary depending on the lattice structure. Since MoS_2 and other 2D semiconductors possess hexagonal lattice, BZ of such systems is briefly addressed below:

[i] P. Yu and M. Cardona; Fundamentals of Semiconductors, 4th edition (Springer-Verlang Berlin Heidelberg 2010), p20-23
[ii] C. Kittle; Introduction to Solid State Physics, 7th edition (Wiley, New York 1995), p37
[iii] H. Zhu, Z. Xu, D. Xie, and Y. Fang; Graphene (Elsevier, Cambridge 2018), p77-78
[iv] Z. Wang; MoS_2 (Springer, Switzerland 2014), p42

The reciprocal of a simple hexagonal Bravais lattice with lattice constants, $a = b$ and c is also a hexagonal lattice. The lattice constants in reciprocal space become $4\pi/a\sqrt{3}$ and $2\pi/c$ rotated by 30° about the c axis. Therefore, it has three main critical points expressed as M and K and K' as shown in the Figure BZ. However, there is another critical point called Q can also be identified along the Γ- K line.

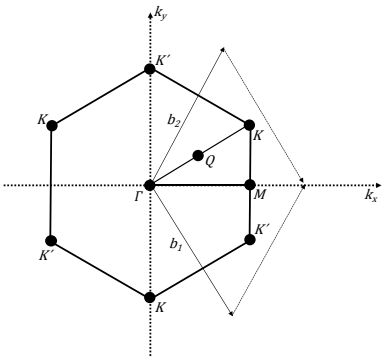

Figure BZ: Reciprocal lattice vectors and hexagonal Brillouin zone of MoS_2.

the Q point is located along the Γ-K line. Therefore, the optoelectronic transition along the Γ-Q line reveals the indirect nature of the band gap in bulk MoS_2. The valence band maxima at Γ point is diffused and is composed of both Mo 4d and S 3p orbitals of antibonding character; therefore, the band gap energy is strongly modulated by interlayer coupling. On the other hand, the valence and conduction bands at the K point are made up of Mo 4d type orbitals and are strongly localized on the central metal atom. Hence, the band energies at the K point have minimal sensitivity to the layer separation. As the layer thickness decreases from bulk to few layers, the valence (conduction) band energies at Γ (Q) point stabilize (destabilize), which results in the increase of the indirect band gap. However, the direct band gap at the K point remains unchanged. For monolayer, the direct band gap at the K point becomes smaller than the indirect band gap and thus yields strong photoluminescence. Another important factor of the strong confinement along ***z*** direction is the increase of the exciton binding energy. The exciton binding energy of bulk MoS_2 is in the range of (50 – 80) meV.[117-120] However, in monolayer the binding energy rises to a value ranging from 220 meV to 1 eV as reported in the literature (both experimental and theoretical).[121-127] Due to such high exciton binding energy, MoS_2 is a perfect platform to study many body effect such as trions, biexcitons, and polaritons.[47, 128-129]

The MoS_2 crystal used in this thesis work was purchased from 2D semiconductors, USA. Intrinsically, it is an n-type semiconductor due to the S vacancies in the crystal which introduce localized donor states inside the band gap.[130-132] The effective carrier concentration of monolayer MoS_2 is in the range of $10^{12} – 10^{13}$ cm^{-2}. The electron mobility is determined to be 200 $cm^2 \cdot V^{-1} \cdot s^{-1}$ at room temperature using a high-k dielectric top gate oxide for mechanically exfoliated 1L MoS_2.[30]

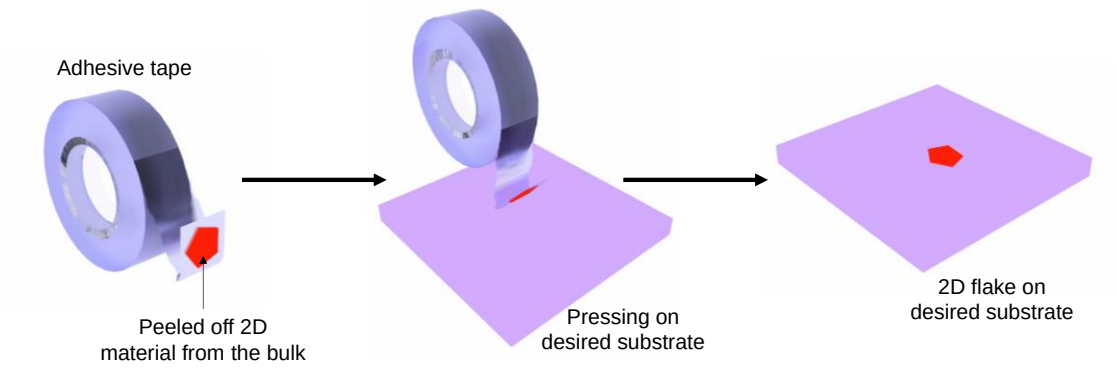

Figure 2.3: Schematic of the mechanical exfoliation method.

However, theoretically predicted electron mobility of 400 $cm^2 \cdot V^{-1} \cdot s^{-1}$ in 1L MoS_2 at room temperature is found to be dominated by optical phonon scattering in the material.[133] The difference between the theory and experiment can be explained by the defects and substrate optical phonon. The field effect carrier mobility in monolayer MoS_2 is reported to be 1000 $cm^2 \cdot V^{-1} \cdot s^{-1}$ at low temperature using vacuum annealing of the device.[134] The vacuum annealing improves the metal semiconductor contact by eliminating the Schottky barrier at the interface. However, CVD grown MoS_2 has significantly lower electron mobility.[135] In MoS_2, the central Mo atoms provide four electrons to fill the bonding states of TMDCs such that the oxidation states of the Mo and S atoms are +4 and −2, respectively. The lone-pair electrons of the S atoms terminate the surfaces of the layers, and the absence of dangling bonds renders those layers stable against reactions with environmental species.[99] Therefore, MoS_2 is stable in air.

2.3: Methods of Preparation

There are several techniques to prepare 2D semiconductor flakes from lab to industrial scale. However, large scale production of the 2D semiconductors is still in the optimizing stage. Some widely used preparation techniques of 2D semiconductors are discussed below.

Mechanical exfoliation: The most widely used preparation method for all 2D materials is the micromechanical cleavage. In fact, the first report on atomic crystal of 2D material, graphene, was prepared by this technique.[13] It is the most easy and straightforward approach for the preparation of monolayer and few layers of 2D semiconductors. Minerals of the 2D semiconductors can be used for this purpose in addition to crystals produced by the chemical vapour transport method. The schematic of the cleavage technique is presented in Figure 2.3. An adhesive tape is essential to peel

off monolayer and few layers of 2D flakes from the bulk crystal. After that, the tape is pressed on to the desired substrate to stamp the flakes on it. Over the years, this method has been modified to prepare not only a single flake but also heterostructures of different combination of the 2D materials on a desired substrate.[136-139] Though, this method is widely used to produce high crystalline flakes of 2D semiconductors, the use of this technique is limited to fundamental research due to its very low scalability and random size distribution. The maximum size of the monolayer flakes produced by this technique is in the range of few 10s micrometer. Therefore, other methods are developed to increase the dimension for industrial application.

Liquid exfoliation: It is another popular approach of synthesis for single layer and few layers of 2D materials in large quantities. Since 2D materials have relatively large separation between the layers, it is possible to intercalate various compounds such as alkali metals in between the sheets.[140-143] In this approach, the powder or crystal of the desired material is soaked in an organic alkali compound solution, resulting in the intercalation of the alkali metal in between the layers. The solution is then mixed with water. Gaseous hydrogen is released in a reaction and pushes the layers apart. The advantage of this method is that it can produce large quantities of monolayer dispersion. However, more often flakes prepared by this technique undergo structural modifications that lead to different physical properties.[143-145] Additionally, intercalation with lithium compounds can lead to the disintegration of the 2D materials into metal nanoparticles and precipitation of Li_2X (X = chalcogen).[140, 146] The alternative to the alkali intercalation is the ultra-sonication in an organic solvent or surfactant solution.[141, 143, 147] In this method, the surface tension of the surfactant needs to match closely to the surface energy of the desired layered material. This method can overcome the challenges of the alkali intercalation. However, the size of the monolayer flakes prepared by this technique is in the range of several 100s nanometer.

Large scale production: The excellent properties of the layered semiconductors offer great promise for future technological applications. Therefore, it is necessary to develop well controlled deposition techniques with large scale production. There are several deposition methods demonstrated so far as will be discussed in this section. However, all the techniques are still in the development and optimization stage. Chemical vapor deposition (CVD) is one of the vastly used techniques for large scale production of layered materials. Following the pioneer works published in 2012 by Zhan *et al.*[148] and Liu *et al.*[149] on MoS_2, the CVD technique attracted a lot of interest for other layered semiconductors as well. In this approach, solid MoO_2 or MoO_3 is placed with S powder in a furnace and heated under inert gas in atmospheric pressure. Solid precursors are then evaporated and react in vapor phase. In both works, however, the CVD technique had difficulties in achieving monolayer growth of MoS_2. Control over thickness and monolayer growth over large areas was reported by Lee *et al.*,[150] Zande *et al.*,[151] and Najmaei *et al.*[152] The growth of an atomically thin large area GaSe film was first reported by Lei *et al.*[35] in 2013. Though the CVD method is a

simple route to synthesize a monolayer film, it often suffers from thickness inhomogeneity and does not always have precise control over material growth. The films prepared using this technique are polycrystalline with lot of grain boundaries due to randomly oriented nucleation sites. Grain boundaries are known to impede electrical conductivity due to degradation of the carrier mobility. Moreover, the maximum size of the monolayer film is in the range of 100 μm, which is still far away from the technologically relevant scale.

Recently, wafer scale homogeneous films of monolayer MoS_2 and WS_2 were reported by Kang *et al.*[153] using metal-organic chemical vapour deposition (MOCVD). The reactions of the precursors ($Mo(CO)_6$ or $W(CO)_6$) in a furnace were maintained in a relatively low pressure (~ 10^{-4} mbar) resulting in high quality wafer scale monolayer films. The electron mobilities of MoS_2 and WS_2 were measured to be 30 $cm^2 \cdot V^{-1} \cdot s^{-1}$ and 18 $cm^2 \cdot V^{-1} \cdot s^{-1}$ at room temperature and offer great hope to industrial fabrication and device assembly.

With the rapid growth of this research field, the fundamental study of 2D materials goes beyond the individual compounds to focus on their heterostructures. By designing suitable vertical stacks of the van der Waals materials, it is possible to explore the unique optoelectronic properties of 2D semiconductors in novel device schemes.[154-158] Therefore, deposition techniques suitable to fabricate such heterostructures have become more popular. Van der Waals epitaxy is one of the techniques implemented to prepare such vertical stacking of layered materials.[159-161] In combination with chemical vapor deposition technique, the material formed is carried downstream by an inert gas onto a desired van der Waals substrate. The lateral size of the deposited film is limited by CVD parameters.

Another method used to prepare 2D semiconductors and their heterostructures is molecular beam epitaxy (MBE). MBE is a well-established technique to prepare high quality uniform epitaxial layers with precise control over thickness.[162-164] In MBE, high purity metals and chalcogens of the desired material are evaporated at a certain temperature and deposited onto a well cleaned substrate. In case of a van der Waals substrate, the material is generally first cleaved in air and then annealed in high vacuum for a certain time to remove surface contaminations. The lateral dimension of the film prepared by this technique can reach wafer scale with thickness uniformity.

Atomic layer deposition (ALD) is another technique adopted to prepare wafer scale monolayer TMDC.[165-169] A self-limiting reaction (which stops at monolayer coverage) between metal reagent (pulsed introduction) and H_2S provides monolayer films. The films produced by this method are generally amorphous. However, crystallinity can be achieved by annealing.

Chapter 3

Experimental Methods

In this chapter the experimental methods used to study the material properties are discussed.

3.1: Atomic force microscopy (AFM)

Atomic force microscopy (AFM) is one type of scanning probe microscopy (SPM), which provides very high-resolution imaging of materials (>1000 times better than the optical diffraction limit).[170] The success of the scanning tunnelling microscopy (STM), for which, Gerd Binning and Heinrich Rohrer shared the Nobel Prize in 1986,[171] opened the door for a host of other scanning probe techniques. STM requires conductive samples, thus it is limited to metals and semiconductors. The limitation can be overcome by designing a probe-sample system that can measure the forces (in atomic scale) acting between them. For example, the vibrational frequencies (ω) of atoms bound in a molecule or in a crystalline solid are generally 10 THz or higher.[172] Considering the mass of the atoms, 10^{-25} kg, the interatomic spring constant k, given by $\omega^2 m$, becomes 10 N/m. Therefore, by using a soft cantilever spring (typically k < 10 N/m), one can image atomic scale topography. Additionally, the applied force should not be too large to deform the atomic sites.

Figure 3.1 shows the simple schematic of an AFM system. A sharp probing tip is attached to a cantilever spring. At large separation between the tip and the probing substrate, the laser deflection from the cantilever is treated as the reference. Once the cantilever is brought down onto the sample surface, it bends due to the force acting between them. The laser deflection collected by the photodiode is digitized and compared with the reference. There are two modes of scanning of a sample surface: constant height mode and constant force mode. At constant height mode, tip-sample distance is kept constant by the feedback loop and the acting force is adjusted to image the substrate. It is opposite in constant force mode. The deflection value (x) of the cantilever is converted into force using Hook's law ($F = -k \cdot x$; where k is the spring constant of the cantilever). Assuming a cantilever spring constant of 1 N/m and the deflection measured by photodiode to be 1 Å, then the force acting between the tip and sample is 10^{-10} N. This is smaller than a typical interaction of two covalently bonded atoms (in the range of 10^{-9} N) at a separation of 1 Å.[173]

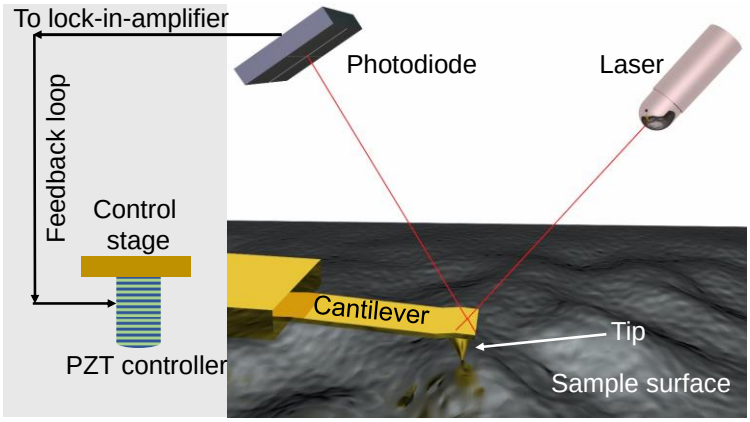

Figure 3.1: Schematic of AFM. The cantilever deflection is collected by the photodiode and send to lock-in-amplifier to be processed. A fraction of the signal is passed to PZT scanner via a feedback loop. The PZT controller is connected to either the sample stage or the cantilever chip.

Interaction between a tip and the sample can be approximated by the Lennard –Jones potential model.[174] Figure 3.2a presents the model in terms of force *vs* distance. As can be seen, it has two main regimes, known as attractive and repulsive regime depending on tip – sample distance. At large separation, the interactions are dominated by long range attractive forces such as van der Waals force, dispersion force, capillary force etc. Whereas, at a critical distance, known as inter-atomic distance (typical inter-atomic distance, $d_0 = 1$ Å), the interaction becomes repulsive due to overlapping of the electron orbitals. Based on the tip-sample distance, AFM can be operated either in contact mode or in non-contact mode. In contact mode AFM, sample imaging is performed by collecting the laser deflection from the cantilever. However, in non-contact mode, attractive forces between the tip and sample are substantially weak. Therefore, the tip is oscillating at or near the resonance frequency of the cantilever. The force interactions are measured either by the change in amplitude of the oscillation or the change in the resonant frequency. Both modes have advantages and disadvantages. Due to strong tip-sample interaction forces, contact mode AFM provides high resolution. However, this mode is prone to sample modification or damage due to dragging during scanning. This issue can be avoided by using non-contact AFM, better suited for soft and liquid samples. Besides these two forms of operation, there is another mode called intermittent contact mode (also known as tapping mode). The typical working zone of this mode is marked by the greenish shaded area in Figure 3.2a. Like in non-contact AFM, the tip oscillates at or near resonance frequency of the cantilever in tapping mode. This mode has been developed to combine the advantage of both contact and non-contact AFM. The tip is alternatively in contact with the sample to gain high resolution and the lift of the tip off the substrate avoids damage due to dragging across the surface.

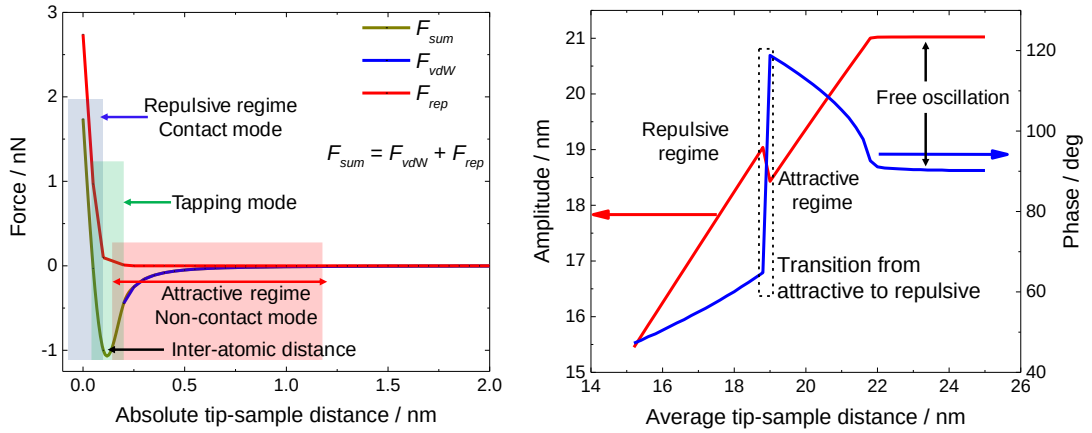

(a) Force vs distance curve

(b) Amplitude, phase vs distance curve

Figure 3.2: (a) A typical Force vs absolute tip-sample distance (*F vs d*) curve. F_{sum}, F_{vdW}, and F_{rep} were calculated using the tip-sample interaction force described in ref.[344-336] Details of the calculation of the forces acting between tip and sample are given in Appendix A-1. The *F vs d* curve is divided into two regimes, attractive and repulsive. AFM operating in the attractive regime is called non-contact mode and in repulsive regime it is called contact mode AFM. To combine the advantages of the both modes, tapping mode AFM was developed (greenish shaded area). (b) Simulated amplitude, phase vs average tip-sample distance (APD) curve using the analytical solution for the tip-sample system described in ref.[346-347] The simulation method is discussed in Appendix A-2. Transition from attractive to repulsive regime is shown by dashed rectangle. As can be seen, the phase curve has a larger response to the shift in the tip-sample interaction. Therefore, it is more sensitive to local chemical and morphological change of the sample.

Besides topography, there are two additional images can be acquired in dynamic mode AFM (both non-contact and tapping mode) by measuring the change in amplitude and phase of the oscillation. In fact, phase measurements are needed for proper topographic imaging in dynamic mode AFM. A typical amplitude, phase vs distance (APD) curve is plotted in Figure 3.2b. In tapping mode, the tip oscillates within a small range of tip-sample interaction distance switching from attractive to repulsive regime. Both amplitude and phase curves have a transition while the tip oscillation shifts from dominant attractive to dominant repulsive regime. However, the phase transition is more sensitive to such shift as shown in the APD curve. Therefore, one should use phase images to diagnose the regime of tip-sample interaction to ensure that the height images are a reasonable approximation of the true topography. Moreover, for the same reason, the phase image is sensitive to sample heterogeneities and change in morphology; thus often used to distinguish two physical components in the probed samples.[175-178]

In this work, Agilent 5420 and AIST-NT scanning probe systems were used for AFM measurements using tapping mode AFM.

3.2: Raman spectroscopy:

Raman spectroscopy is a non-destructive optical method for probing vibrational frequencies of a material. Depending on the energy of the photon scattered, one can distinguish between elastic Rayleigh (photon energy is preserved after scattering), and inelastic Brillouin and Raman (photon energy is not preserved) scattering. Similar to Rayleigh, Raman scattering also occurs when light interacts with the material. When monochromatic radiation of an angular frequency, ω_i, is shined onto a material, it interacts with the matter to create or destroy one or more lattice vibration quanta or phonons. The energy, $\hbar\omega_0$ gained or lost by the lattice is compensated by the increase or decrease of the frequency of the scattered light, $\hbar\omega_s$, known as Raman scattering and expressed by

$$\left.\begin{aligned} \hbar\omega_s &= \hbar\omega_i \pm \hbar\omega_0 \\ \boldsymbol{k_s} &= \boldsymbol{k_i} \pm \boldsymbol{q} \end{aligned}\right\} \qquad 3.1$$

$\boldsymbol{k}_s$, $\boldsymbol{k}_i$, and $\boldsymbol{q}$ are the wavevectors of the scattered light, incident light, and phonon, respectively. The phenomenon of such scattering was first postulated by A. Smekal in 1923.[179] However, the effect is named after C.V. Raman who first reported the experimental observation of inelastic scattered light from a solid in 1928.[180] The efficiency of Raman scattering is in the order of 1 in 10^7 of the excitation photons.[181] Therefore, a sophisticated technological advancement is required to acquire Raman signals. Before going into the technological details of the technique, the theoretical aspect of Raman spectroscopy is addressed in the following sections.

The excitation lasers used in the Raman experiments have a wavevector given by (taken from ref.[182]),

$$|\boldsymbol{k_i}| = \frac{2\pi n}{\lambda} \qquad 3.2$$

where, n is refractive index, and λ is the excitation wavelength. For an incident photon of 500 nm wavelength and a medium of refractive index of 4.5 (refractive index of 1L-MoS_2 at this wavelength[183]) , the wavevector, $|\boldsymbol{k_i}|$ becomes 5.6 x 10^5 cm^{-1}. This is very small compared to the

extent of a Brillouin zone in a solid crystal given by, $\boldsymbol{q} = \frac{\pi}{\boldsymbol{a}}$; $\boldsymbol{a}$ is the lattice constant of a Brillouin zone (for a lattice constant, $|\boldsymbol{a}|$ = 2 Å, $|\boldsymbol{q}|$ becomes 1.6 x 10^8 cm^{-1}). Hence, the phonons involved in the first order Raman effect have a very long wavelength compared to the lattice constant. Due to the long wavelength, they are not influenced by the dispersive effect of the short-range forces such as interatomic restoring forces thus they can be assumed as infinite wavelength phonons. Therefore, first order Raman in a solid is limited to phonon frequencies at $\boldsymbol{q} = 0$ or center of the Brillouin zone (Γ).[182, 184] However, due to crystal imperfections such as defects or impurities, this rule can be lifted (such as D band in graphite originated from defects).[185]

Raman scattering has been described both in terms of classical and quantum theory by several authors.[186-189] A sinusoidal polarization, $\boldsymbol{P}(\boldsymbol{r}, t)$ induced in a medium by a sinusoidal plane electric field, $\boldsymbol{E}(\boldsymbol{r}, t)$ can be expressed by,

$$\boldsymbol{P}(\boldsymbol{r},\ t) = \varepsilon_0 \chi(\boldsymbol{r},\ t)\boldsymbol{E}_i(\boldsymbol{r},\ t) \tag{3.3}$$

$$\text{with, } \boldsymbol{E}_i(\boldsymbol{r},\ t) = \boldsymbol{E}_i(\boldsymbol{k}_i,\ \omega_i)\cos(\boldsymbol{k}_i \cdot \boldsymbol{r} - \omega_i t) \tag{3.4}$$

ε_0, and χ are the dielectric constant of vacuum and the electric susceptibility of the medium, respectively. The electric susceptibility χ can be expressed in terms of the applied electric field as $\chi(k_i, \omega_i)$. The frequency and the wavevector of the induced polarization are the same as the incident radiation and the amplitude is given by reforming the equation 3.3 as,

$$\boldsymbol{P}(\boldsymbol{k}_i,\ \omega_i) = \varepsilon_0 \chi(\boldsymbol{k}_i,\ \omega_i)\boldsymbol{E}_i(\boldsymbol{k}_i,\ \omega_i) \tag{3.5}$$

In case of a finite temperature, there are fluctuations in the susceptibility χ due to thermally excited atomic vibrations (phonons) in the medium. The phonon assisted atomic displacements, $\boldsymbol{Q}(\boldsymbol{r}, t)$ can be expressed as,

$$\boldsymbol{Q}(\boldsymbol{r},\ t) = \boldsymbol{Q}(\boldsymbol{q},\ \omega_0)\cos(\boldsymbol{q} \cdot \boldsymbol{r} - \omega_0 t) \tag{3.6}$$

ω_0 is the frequency of the phonon. The frequency of the phonons ω_0 is much smaller than the characteristic electronic frequency ω_i which determine the susceptibility. Therefore, according to

The mathematical interpretations of Raman scattering have been described with help of Ref.[186] in this section.

the adiabatic approximation χ can be taken to be a function of $\boldsymbol{Q}$. The susceptibility χ can be expanded as a Taylor series in $\boldsymbol{Q}(\boldsymbol{r}, t)$ as followings:

$$\chi(\boldsymbol{k}_i,\ \omega_i,\ \boldsymbol{Q}) = \chi_0(\boldsymbol{k}_i,\ \omega_i) + \left(\frac{\delta\chi}{\delta\boldsymbol{Q}}\right)_0 \boldsymbol{Q}(\boldsymbol{r},\ t) + \cdots \qquad 3.7$$

The first term in equation 3.7 is the susceptibility with no fluctuation and the second term is the oscillating susceptibility induced by the phonon. Now substituting equation 3.7 into equation 3.5, the induced polarization, $\boldsymbol{P}(\boldsymbol{r}, t, \boldsymbol{Q})$ in the medium becomes,

$$\boldsymbol{P}(\boldsymbol{r},\ t,\ \boldsymbol{Q}) = \varepsilon_0 \begin{bmatrix} \chi_0(\boldsymbol{k}_i,\ \omega_i)\boldsymbol{E}_i(\boldsymbol{k}_i,\ \omega_i)\cos(\boldsymbol{k}_i\cdot\boldsymbol{r} - \omega_i t) \\ +\left(\frac{\delta\chi}{\delta\boldsymbol{Q}}\right)_0 \boldsymbol{Q}(\boldsymbol{r},\ t)\boldsymbol{E}_i(\boldsymbol{k}_i,\ \omega_i)\cos(\boldsymbol{k}_i\cdot\boldsymbol{r} - \omega_i t) \end{bmatrix} \qquad 3.8$$

The first term inside the bracket is the polarization oscillating in-phase with the applied field and the second term is the polarization induced by the phonon. In order to determine the frequency and the wavevector of the phonon induced polarization, one can rearrange the second term of equation 3.8 as follows:

$$\begin{aligned} \boldsymbol{P}_{ind}(\boldsymbol{r},\ t,\ \boldsymbol{Q}) &= \varepsilon_0 \left(\frac{\delta\chi}{\delta\boldsymbol{Q}}\right)_0 \boldsymbol{Q}(\boldsymbol{q},\ \omega_0)\cos(\boldsymbol{q}.\boldsymbol{r} - \omega_0 t) \times \boldsymbol{E}_i(\boldsymbol{k}_i,\ \omega_i)\cos(\boldsymbol{k}_i\cdot\boldsymbol{r} - \omega_i t) \\ &= \frac{1}{2}\varepsilon_0 \left(\frac{\delta\chi}{\delta\boldsymbol{Q}}\right)_0 \boldsymbol{Q}(\boldsymbol{q},\ \omega_0)\boldsymbol{E}_i(\boldsymbol{k}_i, \omega_i t) \times \begin{Bmatrix} \cos[(\boldsymbol{k}_i - \boldsymbol{q})\cdot\boldsymbol{r} - (\omega_i - \omega_0)t] \\ +\cos[((\boldsymbol{k}_i + \boldsymbol{q})\cdot\boldsymbol{r} - (\omega_i + \omega_0)t)] \end{Bmatrix} \end{aligned} \qquad 3.9$$

Equation 3.9 has two sinusoidal waves for phonon induced polarization. The first term has a wavevector $\boldsymbol{k}_i - \boldsymbol{q}$, and a frequency $\omega_i - \omega_0$ known as **Stokes scattering**. The second term with wavevector of $\boldsymbol{k}_i + \boldsymbol{q}$ and frequency of $\omega_i + \omega_0$ is called **anti-Stokes scattering**. The Raman scattering frequency is determined by $\omega_s = \omega_i \pm \omega_0$.

For a phonon mode to be Raman active the polarizability (or susceptibility) must have a nonzero value ($^{\delta\chi}/_{\delta r} \neq 0$) during the vibration. Intensity of the Raman signal depends on the induced polarizations of the incident radiation $\boldsymbol{P}_{ind}$ as,

 The mathematical interpretations of Raman scattering have been described with help of Ref.[186] in this section.

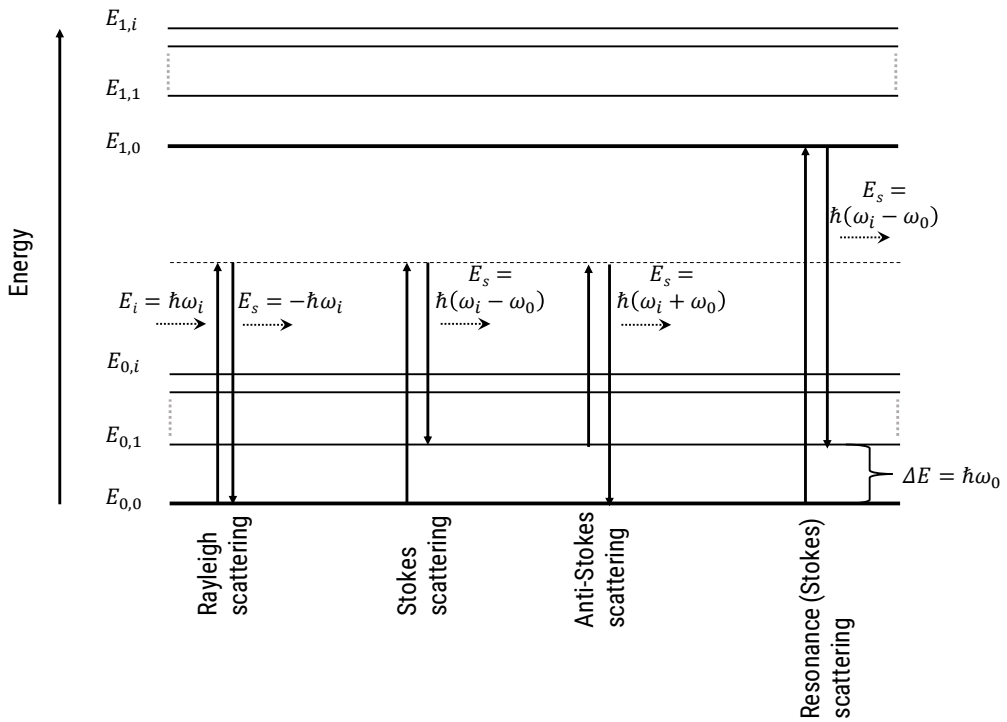

Figure 3.3: Schematic representation of the Raman scattering process in a material. In case of Rayleigh scattering no energy is lost. In Stokes scattering process, electrons relax to an excited phonon state ($E_{0,1}$) and loose an energy equal to $\Delta E = \hbar\omega_0$. Anti-Stokes is the opposite phenomena in which electrons gain the same amount of energy. In case of resonant Raman scattering relaxation happens via a real electronic state ($E_{1,0}$).

$$\left.\begin{aligned} I_R &= |\boldsymbol{P}_{ind} \,.\, \boldsymbol{e}_s|^2 \\ &= \left|\boldsymbol{e}_i \,.\, \left({}^{\delta\chi}/_{\delta\boldsymbol{Q}}\right)_0 Q(\omega_0) \,.\, \boldsymbol{e}_s\right|^2 \\ &= |\boldsymbol{e}_i \,.\, \mathfrak{R} \,.\, \boldsymbol{e}_s|^2 \end{aligned}\right\} \qquad 3.10$$

here, $\boldsymbol{e}_i$ and $\boldsymbol{e}_s$ are the polarization unit vectors of the incident and scattered light, respectively. The middle term in equation 3.10 is simplified by taking $\boldsymbol{q} = 0$ for first order Raman modes. It is also known as the Raman tensor $\mathfrak{R}$ obtained by a contraction of the atomic displacement and the first order derivative of the susceptibility with respect to it. Therefore, by measuring the dependence of the Raman intensity on the incident and scattered polarization it is possible to deduce the symmetry of the Raman tensor and hence the symmetry of the corresponding Raman-

The mathematical interpretations of Raman scattering were described with help of Ref.[186] in this section.

active mode. Since the difference between the incident and scattered wavelength is small, equation 3.10 can be simplified by neglecting the angular and polarization dependence of the Raman tensor together with the vectorial character of both electric fields. In such a case the Raman intensity can be scaled approximately with the fourth power of the incident electric field as,

$$I_R \approx E_i^4 \qquad 3.11$$

Phonons are defined as the eigenfrequencies in terms of quanta of lattice vibration. In the case of Rayleigh scattering, light does not require a real electronic transition. Therefore, electrons are considered to fall back to the electronic ground state after being promoted to a virtual electronic state. A schematic of the scattering process involving Rayleigh and Raman scattering is presented in Figure 3.3. In the case of Rayleigh scattering, incident and scattered light have the same photon energy since no change of energy occurred. In the Raman process, the scattering of a photon can occur via relaxation of electrons from the ground state to the phonon states or vice versa ($E_{0,0}$ to $E_{0,1}$ or vice versa). If the electrons relax to an excited vibrational state, the scattering process is called Stokes scattering. The electrons absorb energy (energy difference is negative) during this process. On the other hand, in the anti-Stokes process, electrons relax back from an excited vibrational state to the electronic ground state and release energy (energy difference is positive). The value of energy difference in both scattering processes is the same because the energy lost or gained is from the same vibrational quantum state. In order to observe anti-Stokes scattering, it is necessary to have some excited states in the system. Excited vibrational states can only be thermally populated, which is true at room temperature. However, it is clearly evident that phonons in ground states are much higher than the excited states. Therefore, the Stokes scattering intensity is always higher than the anti-Stokes scattering. Eventually, Raman scattering can also occur via real electronic states. The process is called resonant Raman scattering. In such case, the scattering process experiences a change in electronic density in the crystal lattice resulting in an enhanced intensity of Raman modes due to the electron phonon coupling (for a brief discussion the process is rather complex and more details can be found in refs[189-190]).

Figure 3.4 displays a schematic of a typical confocal Raman spectrometer system. An interferential band pass filter is used to block anything other than the laser frequency. The optical density filter controls the laser power at the sample surface. Excitation and collection of photons are achieved by an objective of a certain numerical aperture. Often a high numerical aperture is used to increase the collection angle. Since Raman signals are typically 1 in 10^7 of incident photons, Rayleigh scattering needs to be filtered. This is accomplished by an edge filter (low pass for Stokes and high

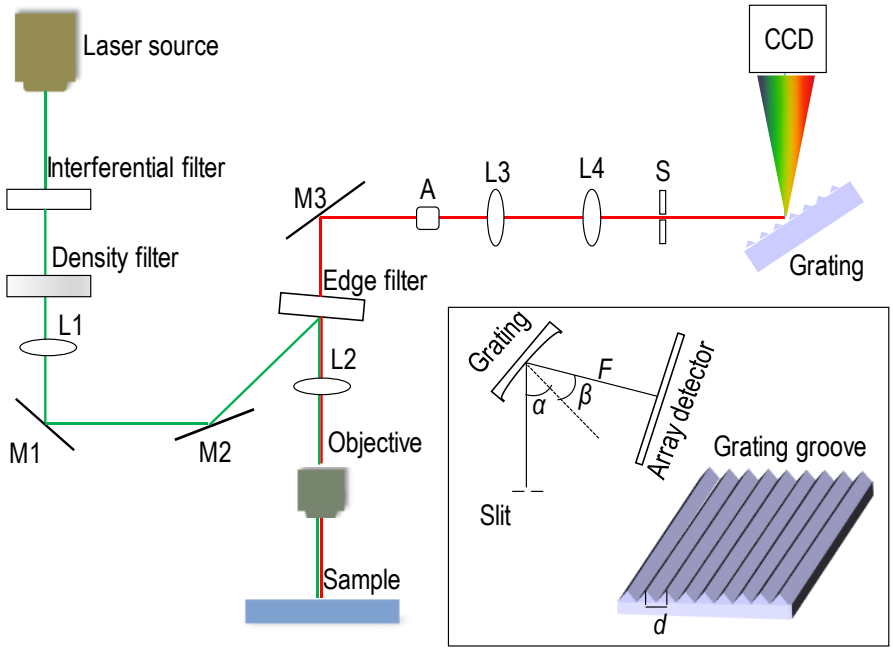

Figure 3.4: Sketch of a typical Raman spectrometer. L stands for lens, M for mirror, A is a confocal aperture, S is the entrance slit to the spectrometer. Inset; the light diffraction mechanism of a grating is shown.

pass for anti-Stokes scattering) as shown in the Figure 3.4. After filtering the Rayleigh signals, often a confocal aperture as marked by "A" in the sketch is used in modern Raman microscope systems to increase the spatial resolution of the analysis volume (both in XY and Z axes). By controlling the aperture diameter, one can also perform depth profiling of the probed material. There are three key components of a Raman spectrometer. These are 1) slit, 2) grating, and 3) detector. Slits control the light flux projected onto the detector. They also determine the spectral resolution, especially when the image size of the slit is larger than the pixel width of the detector array. Therefore, the typical slit width used in Raman measurements is 100 μm to balance the light throughput and the optical resolution. The grating is the second key component which determines the spectral resolution and the wavelength range. Both parameters are greatly influenced by the amount of grooves / lines per mm, also known as groove / lines density or groove / line frequency. The wavelength range of a spectrometer is inversely proportional to the dispersion of the grating due to its fixed geometry. Therefore, reducing the line frequency leads to an increase of wavelength range at the cost of spectral resolution. The angular dispersion of a grating can be written as

$$\frac{d\beta}{d\lambda} = \frac{m}{10^6 \cdot d \cdot cos\beta} \quad 3.12$$

with, β is the diffraction angle, λ is the incident wavelength, d is the groove period of a concave grating as shown in Figure 3.4, and m the diffraction order. Assuming that the detector is placed at the focus point of the grating, and $d\beta \rightarrow 0$, equation 3.12 becomes

$$\frac{d\lambda}{dL} = \frac{10^6 \cdot d \cdot cos\beta}{m \cdot F} \quad 3.13$$

here, dL is the differential length. The wavelength range of the spectrometer is therefore

$$\lambda_{max} - \lambda_{min} = L_D \frac{d\lambda}{dL} = L_D \frac{10^6 \cdot d \cdot cos\beta}{m \cdot F} \quad 3.14$$

where, L_D is the detector length. The spectral resolving power or resolution of the grating is given by,

$$\frac{d\lambda}{\lambda} = \frac{d}{mL_g} = \frac{1}{mN} \quad 3.15$$

with L_g the grating length and N the total groove numbers in the grating. According to equations 3.14 and 3.15, for a given dimension of the detector, the spectral resolution of the spectrometer depends on the focal length of the grating, groove density of the grating and the excitation wavelength as follows:

1) If the focal length increases, spectral resolution increases and wavelength range decreases.
2) If the line density increases, spectral resolution increases and wavelength range decreases.
3) and, if the excitation wavelength increases, spectral resolution also increases, and wavelength coverage decreases.

In this work, gratings of 2400 l/mm, 1200 l/mm, and 600 l/mm are used in Raman measurements depending on the demand of the experiments. The dispersed signals are projected onto the

Discussion of the Raman spectrometer is based on the help taken form http://bwtek.com/spectrometer-introduction/ dated 12.12.2017

detector. An electron multiplying charge coupled detector is used to image the spectral dispersion. This is performed by striking the individual pixels across the CCD with incident photons. Each pixel represents a portion of the spectrum with photoresponse of the pixels then converted into intensity by the software. Since the efficiency of the Raman scattering is very low, it may be necessary to integrate the signal for a long period of time. This requires cooling of the charge couple detector (CCD) in order to reduce the dark noise. In practical devices, CCDs are cooled either by liquid nitrogen or thermoelectric (TE) cooling.

3.3: Tip-enhanced Raman spectroscopy (TERS)

Raman spectroscopy is a powerful tool to probe chemical information of a sample by measuring the phonon modes which can be used for molecular structural analysis and quantification. However, it has two major limitations. As discussed in the previous section Raman spectroscopy suffers from very low sensitivity since typically 1 in every 10^7 photons is counted for Raman signal. An improvement in this aspect came with the introduction of surface-enhanced Raman spectroscopy (SERS). SERS uses metallic nanostructures to cause a localized surface plasmon resonance (LSPR) resulting in a strong electromagnetic (EM) field enhancement at the metal surfaces. The nano-areas with the strongest EM field on the metal nanostructured surfaces are also known as hotspots. The SERS enhancement factor at these hotspots can be written as $EF = (E_{LSPR}/E_i)^4$. Experimentally, the SERS EF has reached on the order of 10^6 ~ 10^8 till date enabling single molecule detection.[191] Even though SERS can surpass the low Raman cross section of many different molecules, it cannot overcome the second major limitation of conventional Raman spectroscopy (or simply known as Raman spectroscopy). The optical diffraction limit prevents Raman spectroscopy (also true for SERS using conventional microscope) from spatially resolving materials beyond few hundreds nm. The spatial resolution of Raman spectroscopy is defined by

$$SR = \frac{0.61\lambda}{N.A.} \qquad 3.16$$

where, $N.A.$ is the numerical aperture of the objective and λ is the excitation wavelength. Equation 3.16 is also known as Abbe diffraction limit. For example, for an objective of 0.9 $N.A.$, a minimum spot size of 350 nm can be achieved with an excitation wavelength of 514 nm. To overcome these two major limitations the concept of near-field optical probing was proposed by Wessel in 1985.[192] Wessel's idea of TERS was to combine the use of a single metal nanoparticle with a SPM. While, the metal nanoparticle serves as the SERS source, introduction of the SPM ensures the atomic

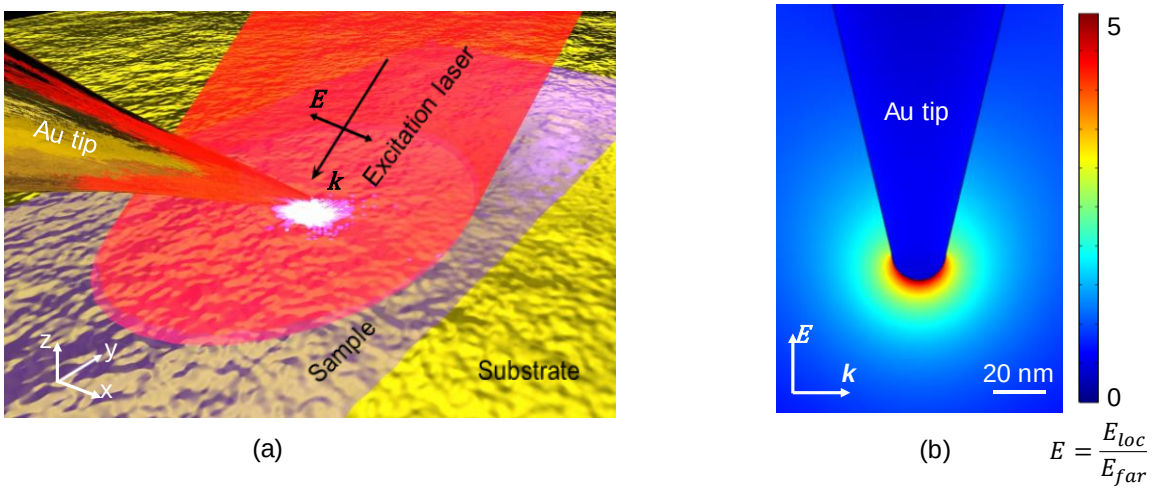

Figure 3.5: (a) Schematic illustration of TERS principle in a side illumination geometry combining the chemical sensitivity of SERS and lateral resolution of SPM. (b) Simulated EM field enhancement map at the vicinity of an Au tip illuminated with a light source of 638 nm wavelength. The electric field is parallel to the tip long axis. E_{loc} and E_{far} are the EM fields generated by plasmonic oscillation and the optical excitation, respectively.

resolution of topographic information of the probing materials. Thus, sensitivity and spatial resolution of Raman spectroscopy can be markedly improved by combining these two techniques. Since the first experimental realization of TERS in the early 2000s, it has emerged as a powerful nanoanalytical tool for nanoscale chemical characterization over the past two decades. Figure 3.5a presents a schematic of a TERS experiment in the side illumination geometry. TERS harnesses the combination of LSPR and lightning rod effect to generate a strong EM field at the apex of a sharp metallic tip.[193] LSPR of a metallic tip is wavelength dependent; while lightning rod effect is geometry dependent. A finite element method (FEM) simulated EM field enhancement at the apex of an Au tip (radius R = 10 nm) is presented in Figure 3.5b. The simulation was performed using the COMSOL Multiphysics platform. The EM field enhancement can reach several orders of magnitude and be confined within a few nanometers at the vicinity of the tip apex (see chapter 5 and 6). In this chapter the concept of TERS is briefly addressed. Details of the theoretical aspects of this method are discussed in chapter 5.

3.4: X-ray photoelectron spectroscopy (XPS)

X-ray photoelectron spectroscopy (XPS) is a surface sensitive spectroscopy technique extensively used to study the surface chemistry of a material. When an atom or molecule absorbs X-ray

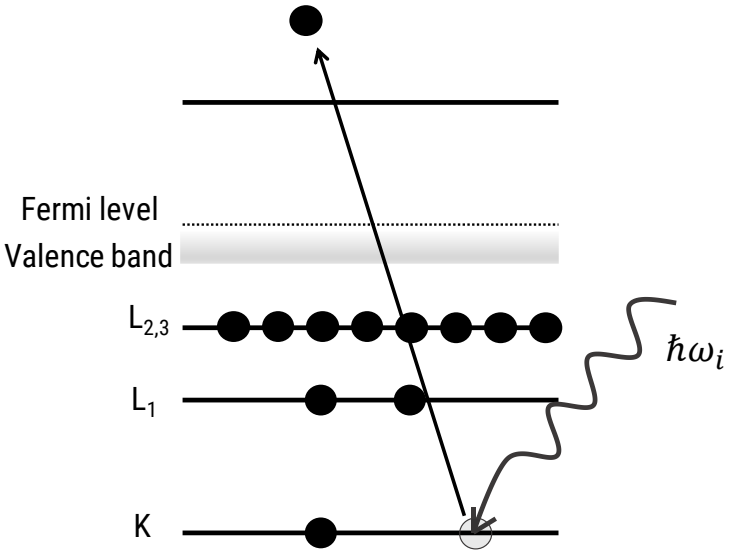

Figure 3.6: A sketch of a photoemission process involved in XPS.

photons, it can emit electrons with a certain kinetic energy. The kinetic energy (KE) of the electrons depends on the excitation energy and the binding energy (BE) of the electron as

$$KE = \hbar\omega_i - BE - \phi \qquad 3.17$$

here, ϕ is the work function of the spectrometer. The binding energy of electrons depends on a number of factors, such as

- the element from which it is ejected,
- the orbital from which it is emitted,
- the chemical environment of the atom.

Therefore, by knowing the binding energy of the electrons, it is possible to determine the elemental composition, chemical, and electronic state of a material. Even though X-ray can penetrate several 100s nm to μm inside a material, the information which the ejected electrons carry is from few nanometers of the film due to the short inelastic mean free path of electrons.[194] Therefore this technique is extremely surface sensitive.

Chapter 4

Environmental stability of GaSe

Most of the work discussed in this chapter is published in ***Semiconductor Science and Technology***, 32, 2017, 105004

In this chapter, the environmental stability of GaSe from bulk to monolayer is discussed. The experimental tools used in this study are Raman spectroscopy, atomic force microscopy (AFM), photoluminescence, and X-ray photoelectron spectroscopy (XPS). The chapter starts with an introduction and motivation of the work. The experimental parameters used in the investigation are addressed. The results and discussion part consists of Raman spectroscopy of bulk GaSe, investigation of laser induced surface modification, Raman spectroscopy of monolayer GaSe, time dependent Raman spectroscopy of few layer GaSe, time dependent photoluminescence, and micro-XPS imaging of GaSe.

4.1: Introduction and Motivation

Similar to TMDCs, GaSe is also predicted to show thickness dependent optoelectronic properties such as non-linear optical emission[57] and band gap variation from 2 eV (bulk) to 4 eV (monolayer).[58] Therefore it can be used for high performance hyperspectral emitters and detectors spanning from ultraviolet (UV) to the visible range when fabricated in heterostructures.[59-60] Moreover, large and fast photoresponse was demonstrated in photodetectors fabricated from monolayer/ultrathin GaSe as well as tunable heterojunctions with graphene.[35-36, 61] Therefore, GaSe is gaining more and more attention. Thinning down the thickness in practical device application is the ultimate goal for such materials.

However, under ambient conditions, the surface of GaSe is known to degrade over time.[195] As shown by Drapak *et al.*,[195] storing of undoped GaSe bulk crystals for prolonged time leads to the formation of several compounds such as Ga_2O_3, SeO_2, SeO_3, Se_2O_5, $Ga_2(SO_3)_3{\cdot}6H_2O$ *etc.* at the surface. Moreover, if heated to temperatures near 450 ^oC the oxidation occurs instantaneously[196] with Ga_2O_3, Ga_2Se_3, SeO_2, and amorphous selenium (*a*-Se) as byproducts which are thermodynamically more favourable. Like other ultrathin semiconductors, both the electrical and

optical properties are markedly influenced by oxidation. Therefore, the environmental stability of GaSe with similar thicknesses needs to be assessed. The degradation of optical properties of few nm thick GaSe over time was reported by Zamudio *et al.*[197], while Beechem *et al.*[198] investigated the physical process of GaSe degradation with thicknesses varying from few nm to few hundreds nm in air. In that report, Beechem *et al.* showed that the oxidation process occurs in two steps: (1) $12GaSe + 3O_2 \rightarrow 4Ga_2Se_3 + 2Ga_2O_3$ and (2) $4GaSe + 3O_2 \rightarrow 2Ga_2O_3 + 4Se$; and further oxidation takes place *via*: $2Ga_2Se_3 + 3O_2 \rightarrow 2Ga_2O_3 + 6Se$. Recently Bergeron *et al.*[199] studied the oxidation dynamics of GaSe in air for thicknesses varying from 10 nm to 200 nm. In their experiment they observed that both Raman and PL intensities rapidly decreasing upon continuous laser irradiation and the Raman signatures of Ga_2Se_3 and β-Ga_2O_3 appeared in the spectra. An interesting observation from their experiments is that the measurements were performed using 532 nm excitation which is above the band gap of GaSe and with a high power density of 6 mW/μm². Therefore, the oxidation they observed is probably due to local photo-oxidation and is thus not the full story of the environmental stability of GaSe. Especially, the thicknesses of the films used in the previous reports were above the ultimate goal targeted in practical devices (monolayer or few layer). Therefore, it is important to investigate the material stability before considering it for an application. This vital question is addressed in this chapter. The environmental and time resolved stabilities of GaSe flakes with thickness varying from monolayer to few layers are investigated.

The polytype used for the investigation in this work is ε-GaSe having a D_{3h} symmetry.[200] This phase has twelve vibrational modes at the center of the Brillouin zone represented by the irreducible representation of the corresponding space group. Among these, eight are in-plane modes (E' and E'') and four are out-of-plane modes (A' and A''). There are two in-plane modes in the lower frequency range: one mode around 35 cm^{-1} (E_{2g}) and another at 59 cm^{-1} (E_{1g}). Both of them are out of reach for the experimental setup due to the cut-off of the edge filter used in the Raman spectrometer. There are three dominant peaks in the Raman spectrum of GaSe: two of them are out-of-plane modes (A^1_{1g} = 132 cm^{-1} and A^2_{1g} = 306 cm^{-1}) and one in-plane mode (E_{2g} = 211 cm^{-1}). In the case of inherent or natural oxidation, a very thin layer of oxide is formed at the surface which is noticeable in the Raman spectrum by the features of a-Se that is a by-product of the oxidation. Since a-Se has a high Raman cross section under red excitation,[201] it can be easily recognized in the Raman spectra as a broad feature around 250 cm^{-1}. Therefore, this feature is monitored as an indication of the oxidation in real time.

4.2: Experimental Details

Bulk ε-GaSe is exfoliated using the scotch tape method on highly ordered pyrolytic graphite substrate (HOPG, purchased from Anfatec). After optical examination, monolayers of GaSe are

identified and confirmed later by thickness determination using intermittent contact mode (tapping mode) atomic force microscopy (AFM) imaging with an AIST-NT system. Immediately after exfoliation, the Raman spectra of GaSe are acquired in a HORIBA Xplora plus system under 638 nm laser excitation with 18.4 μW power (equivalent to a power density of 0.234 mW/μm^2) measured at the sample under a 100x / 0.9 NA objective. In the case of the Raman spectra of bulk GaSe, additionally, the excitation wavelength of 532 nm and 9.8 μW power was chosen. A 1200 l/mm grating is used to disperse the light onto an electron multiplier charge coupled device (EMCCD) detector. The PL emission spectra are taken using a HORIBA LabRam HR 800 system utilizing 514.7 nm excitation with 1 mW power and a liquid nitrogen-cooled back illuminated charge coupled device (CCD). XPS measurements were performed with a Thermo Fisher ESCALAB 250 Xi equipped with a monochromatized Al Kα X-ray gun. The imaging XPS spectra were acquired with a pass energy of 25 eV resulting in an energy resolution of 0.6 eV. For the detection of the photoelectrons from the sample a channel plate detector with 128 x 128 pixels was exposed to a sample area of 100 x 100 μm^2 resulting in a pixel size of 0.78 x 0.78 μm^2.

4.3: Raman signatures of oxidation in bulk ε-GaSe

Selection of excitation wavelength

The characteristic Raman features of bulk ε-GaSe are presented in Figure 4.1 for both 532 nm and 638 nm laser excitations. The peaks at 134 cm^{-1}, 211 cm^{-1}, and 306 cm^{-1} are the characteristic Raman modes of GaSe representing the A^1_{1g}, E_{2g}, and A^2_{1g} modes. Additional to these peaks, there is a small shoulder at the high frequency side of A^1_{1g} mode around 155 cm^{-1}. The origin of this feature is the out-of plane A_1 mode of Ga_2Se_3,[202] formed due to the oxidation of GaSe at the surface and it is in good agreement with previous literature reports.[201] Additionally, in the case of Raman spectra acquired under 638 nm excitation, a broad feature appears around 255 cm^{-1}. The origin and the reason of this broad feature at this excitation bear a significant importance considering the investigation of natural oxidation. The byproducts of natural oxidation of GaSe create an ultrathin film at the surface. Therefore, the material volume probed by the excitation laser is very small. Hence one needs to choose an excitation wavelength for which the Raman sensitivity is the highest. Even though one can see the Raman modes of Ga_2Se_3 with 532 nm excitation, the relative intensity with respect to the noise level is low. In order to increase the signal intensity, one needs to either increase the laser power or accumulation time. Both of which are drawbacks for the objective of this investigation. Moreover, the 532 nm excitation is larger than the band gap of GaSe; thus, accelerates the photoinduced oxidation. On the other hand, no Raman features originating from Ga_2O_3 are observed. Given that the thickness of the oxidized film is 1 to 2 nanometers and optically transparent to the probing lasers (both 638 nm and 532 nm), one should not expect to see the Raman features of Ga_2O_3 in this case. Therefore, the Raman band around 255 cm^{-1} is discussed in

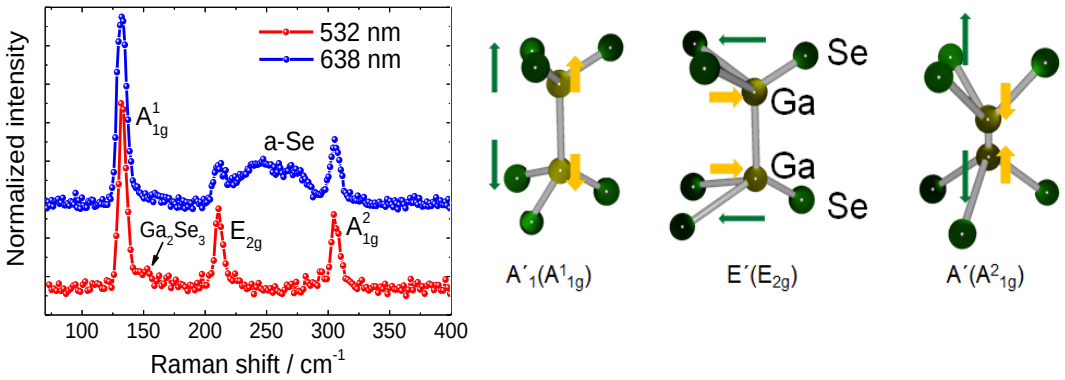

Figure 4.1: Raman spectra of bulk GaSe taken after 10 days of exposure to air. With 532 nm excitation, the three main features of GaSe are observed with a tiny shoulder of Ga_2Se_3 at the high frequency side of the A^1_{1g} mode. At 638 nm excitation, however, additionally a broad feature of *a*-Se appears around 250 cm^{-1} since *a*-Se is in resonance with red excitation. The incident laser powers were 9.8 µW for 532 nm excitation and 18.4 µW for 638 nm excitation. The accumulation time of the Raman signal were 25 minutes for both spectra.

the following sub-section to justify the focus on this mode to monitor the natural oxidation of GaSe. Previous reports showed that the broad feature around 255 cm^{-1} is the contribution of *a*-Se originating from the inter-chain bond stretching of disordered selenium.[201, 203-204] The band gap of *a*-Se is around 1.5 eV - 1.7 eV[204-206] with a broad dispersion covering the red spectral range. Hence, *a*-Se has a high Raman yield with red excitation due to the resonance condition and Raman spectroscopy is sensitive to an ultra-low amount.

4.4: Laser induced surface deformation of GaSe

Beechem *et al.* showed that GaSe can be photo-oxidized by laser irradiation (above band gap) with high laser power. So, in order to monitor the natural oxidation in GaSe, it is necessary to carefully select the excitation wavelength and laser power for the Raman measurements. In these experiments, the excitation wavelength of 638 nm is chosen because first it is below the band gap of GaSe and secondly *a*-Se has a high Raman cross-section at this excitation. Figure 4.2 displays the influence of the laser power on the surface stability of GaSe. The AFM topography, phase, and optical images of the flake after Raman spectra acquisition at different power densities are presented in Figure 4.2a-e. The thickness of the flake is (19 ± 0.3) nm and the height profile is presented in the inset of Figure 4.2a. As can be seen from the topography and optical images, there

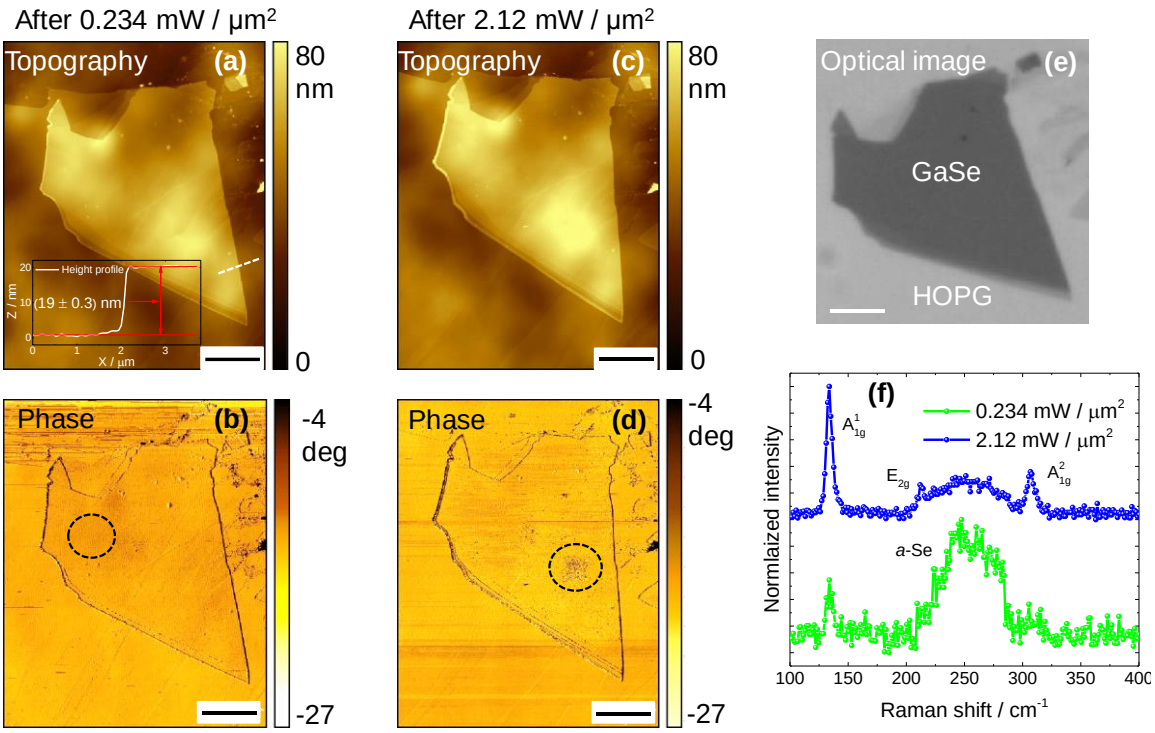

Figure 4.2: Laser induced surface stability of GaSe. Topography (a) and phase image (b) of a flake after 0.234 mW/µm² laser irradiation. The height profile of the flake along the white dashed line is presented in the inset of (a). (c) and (d) are the topography and phase image after 2.12 mW/µm² irradiation. The dashed circles drawn in the phase images are the area of the laser irradiation. Optical image (e) and the Raman spectra (f) of the flake at the two power densities with 638 nmexcitation. The spectral acquisition times were 120 s x 2. The scale bar in all images is 5 µm.

is no damage visible on the sample surface due to laser irradiation. In case of 0.234 mW/µm² irradiation, the phase image also remains homogeneous. But in the case of 2.12 mW/µm² illumination, there is a clear change visible in the phase image marked by a circle in Figure 4.2d. As discussed in section 3.1, the phase image is in particular sensitive to the variation in chemical and physical environments between tip and sample due to changes in adhesive force and friction. Hence, any change in the homogeneity or uneven surface or change of chemical nature of the substrate should be visible. Therefore, the change one can observe in the phase image in the case of 2.12 mW/µm² irradiation originates from photoinduced deformation similar to the phenomenon observed by Beechem *et al.*[198] So it can be concluded that 0.234 mW/µm² laser irradiation is not strong enough to cause modification at the surface; thus, the influence of laser power in the oxidation of GaSe can be excluded for this case. In this investigation, unless mentioned otherwise,

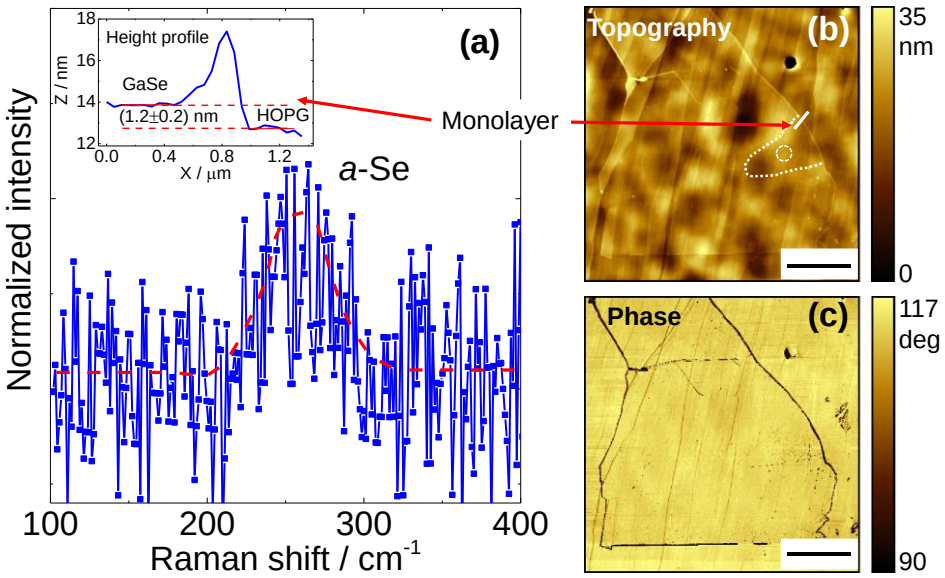

Figure 4.3: Raman spectra of the GaSe monolayer obtained immediately after exfoliation (a). The red dashed line is drawn as the guide to the eye of the peak around 250 cm^{-1}. The corresponding AFM topography and the phase image (b). The white dashed circle is the spot where the Raman spectrum is taken. The dotted lines indicate the GaSe monolayer. The height profile of the flake is shown in the inset of Figure (a). The hump at the border is due to the sharp edge resulting from mechanical exfoliation. All scale bars are 5 µm.

the 638 nm laser line with a power of 18.4 µW equivalent to a power density of 0.234 mW/µm² is used. One may wonder about the relative Raman intensity of *a*-Se with respect to GaSe in case of 2.12 mW/µm² laser irradiation (see Figure 4.2f), as the Raman intensity is proportional to the incident power density. The reason of the relatively weak Raman response of *a*-Se in the case of 2.12 mW/µm² can be explained by the photoinduced volume change[207] at this power density. The acquisition time used for each Raman spectrum is 120 s (similar to the time used for time evolution of oxidation of GaSe in section 4.6). The challenge for this experiment is acquiring Raman spectra from the sample without making any photo-induced modification. Therefore, the laser power is significantly reduced. However, the decrease of the laser power results in low Raman signals. Hence, to increase the Raman signal, one can keep the acquisition time infinitely long. In this experiment, since time resolved stability of GaSe is investigated, prolonging the acquisition time would be a drawback for this purpose. Therefore, a trade-off was made by choosing an acquisition time of 120 s such that the acquired results are conclusive enough.

4.5: Environmental stability of monolayer GaSe

The Raman spectrum of monolayer GaSe immediately after exfoliation is displayed in Figure 4.3a. The time between the exfoliation and mounting the sample under the Raman microscope is 2 minutes. The spectrum is taken with an acquisition time of 150 s and of 2 accumulations. The spectral acquisition time is increased by 30 s compared to the previous section due to very low signal (probing volume in monolayer is much smaller than 19L of GaSe discussed in the previous section). The AFM topography and the phase image are shown in Figure 4.3b-c. The thickness of the monolayer GaSe is determined to be around 1 nm (precisely 1.2 nm ±0.2 nm as determined from linear fits) in agreement with literature values.[36] The slight increase of the monolayer thickness (0.2 nm in this case) can be due to the presence of absorbents such as water molecules at the surface in air during the measurement. The hump at the border of the flake is due to the sharp edge originating from exfoliation. Notice that the height scales in the AFM image in Figure 4.3b, and the profile in Figure 4.3a, are offset due to the hole defect in HOPG at the top right side that dominates the lowest values of the height contrast. As can be seen from Figure 4.3a, no GaSe phonon modes are visible in the spectrum, while a broad feature around 255 cm^{-1} is observed characteristic for *a*-Se. The band observed originates from the oxidation of GaSe. We did not observe any peak corresponding to other phases such as Ga_2Se_3. This could be due to the very small amount of material which is not sensitive to the chosen excitation wavelength. There is no visible change observed in the topography as well as in the phase image of the flake. So it can be concluded that there is no photoinduced damage in the GaSe flake; hence, no photooxidation.

Among all 2D materials, graphene and h-BN are known to be the most stable ones at room conditions.[208] However, h-BN nanosheets have higher temperature stability than graphene, since the former material can tolerate temperatures as high as 850 °C.[209] Similarly, MoS_2, WS_2, and others also exhibit high resistance against oxidation even though these materials age with time. Gao *et al.*[210] investigated the aging in transition metal dichalcogenides (TMDCs) and observed that the oxidation started at the grain boundaries, sheet edges and the chalcogen atom vacancies. After that, oxygen atoms penetrate gradually into the crystal lattice and replace chalcogen atoms. A similar explanation can also hold for GaSe. But contrary to TMDCs the GaSe surface oxidizes much more rapidly.

4.6: Time evolution of the GaSe oxidation

It is shown in the previous section that monolayer GaSe oxidizes almost immediately (due to preparation and Raman acquisition time of 270 s) after exposure to air. Therefore, it is interesting to see the oxidation dynamics in few layer GaSe, particularly how fast and deep this oxidation

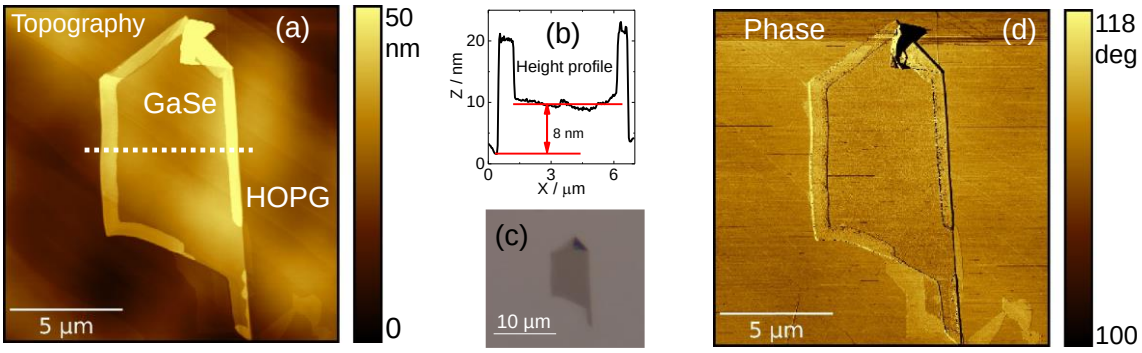

Figure 4.4: AFM topography (a) of the GaSe flake used for the time evolution of oxidation in Figure 4.5. The height profile of the flake (d) along the dashed line in (a). The optical (c) and phase (d) images of the flake.

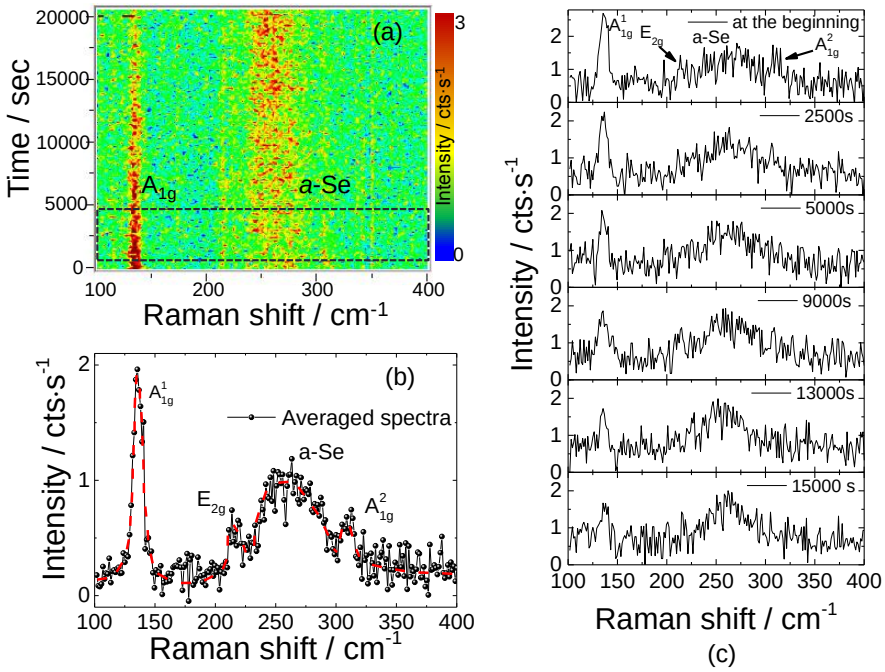

Figure 4.5: Time evolution map of the Raman spectra of the flake (a) and averaged Raman spectrum taken from the rectangle area (a). The red dashed line is drawn as the guide for the eye. Raman spectra taken at different times from the evolution map (c). Each Raman spectrum was acquired with 120 s x 2 of accumulation time.

penetrates into the GaSe layers. In order to investigate the inherent oxidation, a thin flake (8 L) of GaSe is exfoliated on HOPG and the time evolution of the Raman spectra is monitored. The AFM topography, phase, and the optical image of the flake are shown in Figure 4.4a - d. The AFM scan

is performed after the time evolution map. The height profile along the white dashed line in Figure 4.4a is presented in Figure 4.4b. In Figure 4.4d, a homogeneous phase image is observed, meaning no morphological deformation resulting from the laser irradiation. Therefore, one can conclude that the Raman spectra solely represent the change due to natural oxidation. The time evolution result is displayed in Figure 4.5a and an averaged Raman spectrum is shown in Figure 4.5b. The averaged Raman spectrum is created by averaging 20 individual spectra inside the rectangular box shown in Figure 4.5a. The red dashed line in Figure 4.5b is drawn as a guide to the eye. As can be seen in Figure 4.5a, the intensity of the A^1_{1g} mode of GaSe gradually decreases with time while the intensity of the broad *a*-Se Raman feature increases. The opposite trend of both peaks indicates that over time more and more selenium atoms are replaced by oxygen. As a consequence, the intensities of these two bands change in opposite directions. This opposite trend is even better visible in the Raman spectra of the flake taken from the time evolution map as shown in Figure 4.5c. One can see that the intensity ratio of GaSe A^1_{1g} to the broad *a*-Se peak is gradually decreasing as time progresses. Since the intensity of the Raman mode is proportional to the probed volume of the material, one can conclude that the effective GaSe thickness gradually decreased due to oxidation.

Interestingly, as shown in Figure 4.6a, the intensities of both A^1_{1g} and *a*-Se peaks remained constant after 16500 s (ca. 4.6h). Therefore, it can be argued that the oxidation is self-limiting and stops at that time. In order to prove this statement, Raman experiments on different GaSe flakes, with different thicknesses varying from monolayer to a few layers, after 13 days of exposure to air were performed. Hence, if the oxidation is self-limiting then one would notice a thickness dependency for ultra-thin GaSe such that up to certain thicknesses the whole flake would be oxidized after 5 hours of exposure to air. Thus, no Raman modes of GaSe are observed up to this thickness. Beyond this thickness, the Raman modes of GaSe appear in the spectrum and remain unchanged over time. This is demonstrated in Figure 4.6b where the Raman spectra for four GaSe flakes of different thickness are shown. It is systematically found that for all GaSe layers with a thickness of less than 3 nm no GaSe modes were observed showing a spectrum similar to the monolayer in Figure 4.3a. While for layers with thicknesses of 3 nm or higher, the modes of GaSe were present at least immediately after the flake was deposited. For the particular set of samples used in Figure 4.6b, the Raman spectra of the samples are purposely not taken right after exfoliation in order to completely rule out any influences of laser irradiation in the aging process. In this way, one could obtain the purely native degradation time of the flakes and the thickness at which the oxidation reached saturation unaffected by light irradiation. The corresponding AFM images and height profiles of the flakes from 3 L to 8 L are presented in Figure 4.7 together with their optical images. Starting from 8 L, one can see the characteristic features of GaSe together with the broad feature of *a*-Se. Once thinned down to 3 L, the Raman modes of GaSe disappeared completely. Therefore, it can be concluded that the oxidation of GaSe reaches saturation at this

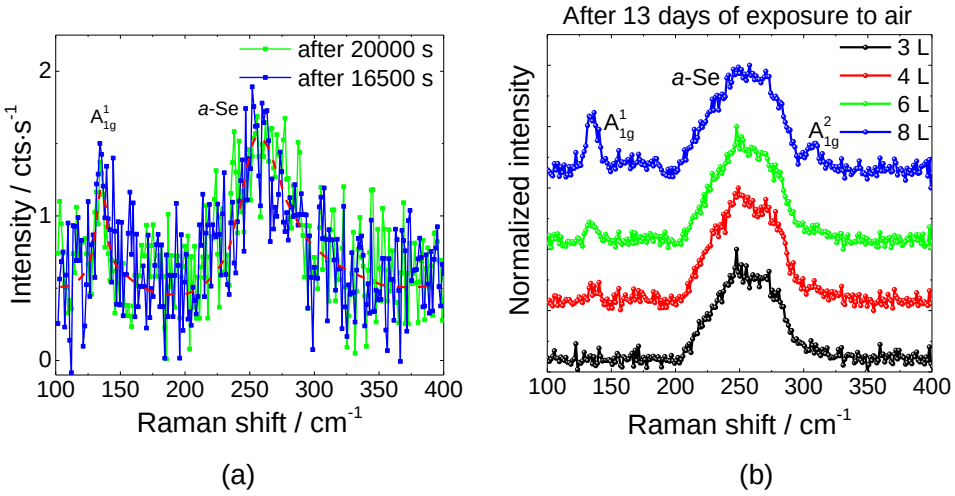

Figure 4.6: Raman spectrum of 8 L GaSe taken at two different times during time evolution map shown in Figure 4.5a (a). Red dashed line is drawn as a guide for the eye. The constant intensity ratio of of A^1_{1g} and *a*-Se peaks indicates that oxidation stops after approximately 16500 s. Thickness dependent Raman spectra of GaSe for oxidation investigation (b). Each spectrum was taken with 700 s x 3 of accumulation time.

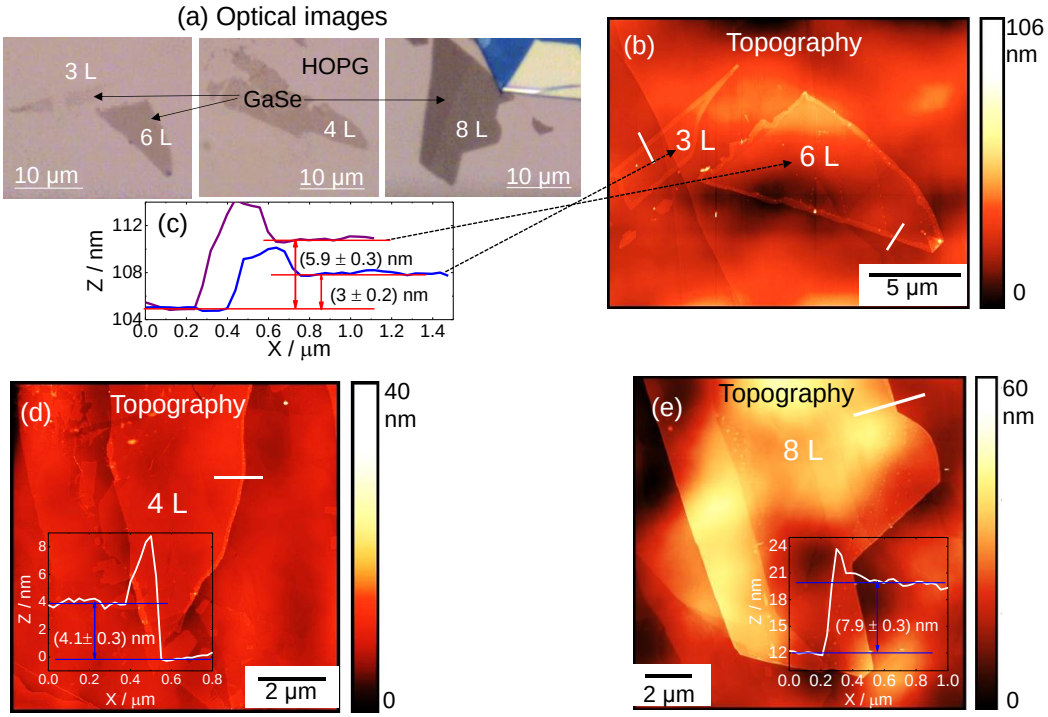

Figure 4.7: Optical images (a) and AFM topography and height profiles (b – e) of GaSe flakes used for Raman study after 13 days of exposure to air. Height profiles of all flakes have humps at the edge of the flake originating from the sharp edges created during exfoliation. All AFM measurements are performed in tapping mode. The waviness of the AFM images originate from the of HOPG substrate which has a well-known wavy surface and the difficulties of the flattening of the images by an image processing software (in this case Gwyddion) due to waviness of the substrate.

thickness. There are two possible causes for this effect. First, it was already reported that the oxidation starts at defects in TMDCs.[210] Moreover, the defect concentration is much higher at the surface due to the exfoliation process during deposition. Hence, the oxidation is much faster at the surface and slows down since the defect density reduces deeper in the flake. So the oxidation process also slows down and stops at some point. Secondly, it is well known for silicon or aluminium that the native oxide at the surface creates a diffusion blocking layer for oxygen and therefore stops further oxidation. In this case Ga_2O_3 and *a*-Se may create a diffusion blocking layer for oxygen that impedes the progress of oxidation once a certain oxide layer thickness is reached.

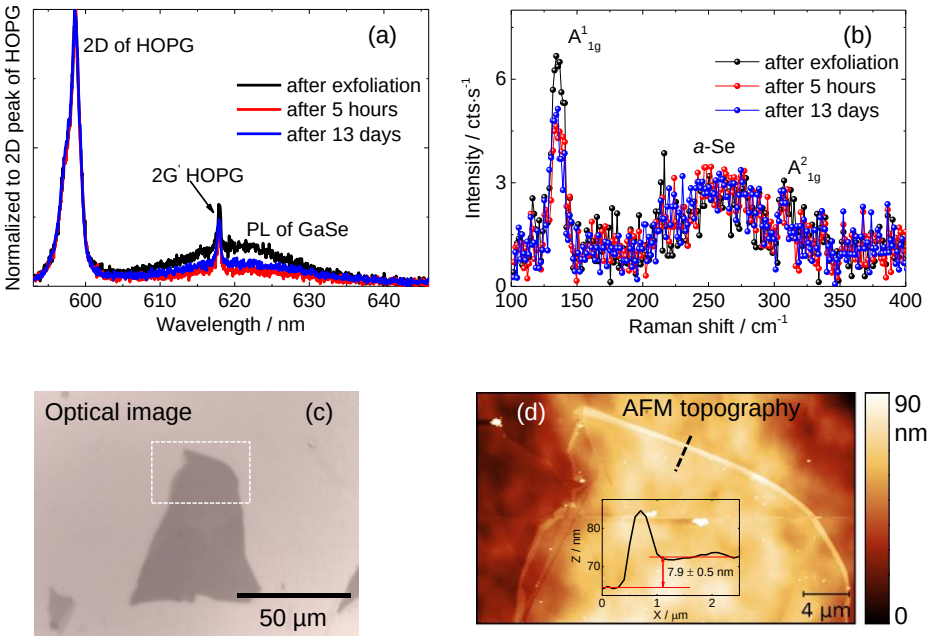

Figure 4.8: Time dependent PL spectra (a) and corresponding Raman spectra (b) of 8 L GaSe. As can be seen, PL and Raman intensities of GaSe after 5 hours and 13 days of exposure to air do not change significantly in a very good agreement with the Raman results. The optical image (c) and AFM topography (d) of the flake. The height profile along the black dashed is presented in the inset of (d).

4.7: Time dependent photoluminescence

A complementary time dependent photoluminescence investigation was carried on a 8 L GaSe (similar to the flake used in the time evolution Raman map). The results are presented in Figure 4.8a and the corresponding Raman spectra in Figure 4.8b. The optical image and the AFM cross section of the flake are presented in Figure 4.8c-d. The excitonic PL emission of GaSe is around 620 nm (2 eV). The PL spectra are normalized to the 2D Raman band of the HOPG substrate since the peak intensity is independent of the GaSe oxidation, but only sensitive to the intensity of the

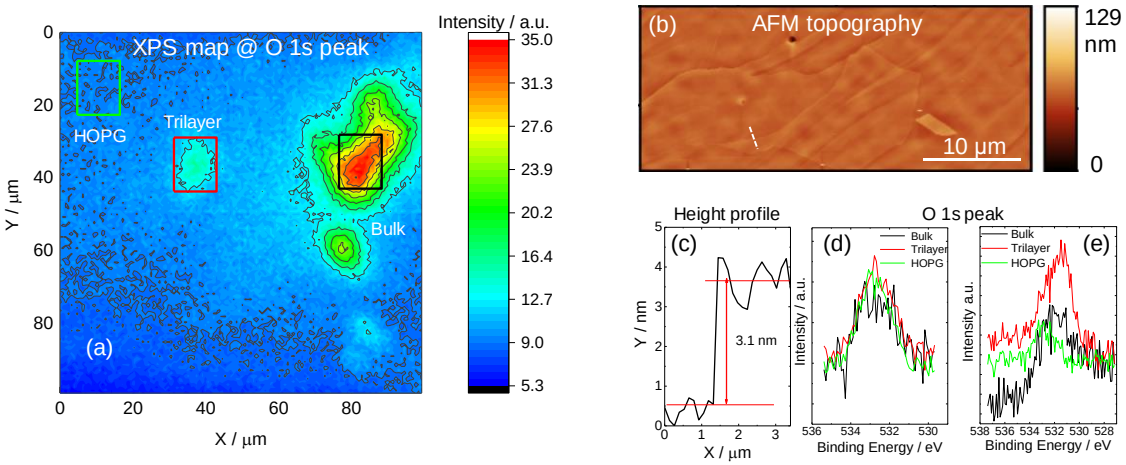

Figure 4.9: O 1*s* XPS integrated intensity map of the sample after 6 h of exposure to air (a). A similar map is acquired immediately after exfoliation. The AFM topography (b) and the height profile along the white dashed line in topography image (c) of the 3 L GaSe flake shown in the map. The O 1*s* peaks extracted from the map from three different regions marked by rectangle (d)-(e). It is evident that both 3 L and bulk GaSe accumulated more oxygen after 6 h of exposure to air.

laser irradiation. The PL spectrum after 5 hours shows a clear decrease in intensity compared to the spectrum acquired immediately after exfoliation. The significant decrease of PL can be attributed to the interaction of the top layers of GaSe with water and oxygen in the atmosphere. Such process leads to the change of the material properties in the form of oxidation. Therefore, the effective layer thickness of GaSe is also reduced. The PL intensity after 13 days of exposure to air shows no significant change with respect to the PL spectrum after 5 hours and indicates no further reduction of the film thickness. This is in very good agreement with the Raman spectroscopy results. Comparing these results with the findings of Zamudio *et al.* there is a certain disagreement. As they showed, the PL intensity of GaSe with thickness from 10 to 25 nm goes to zero after 100 hours of exposure to air. This is not the case in our experiments as both Raman and PL measurements clearly show the presence of GaSe in 5 to 8 nm thick flakes.

4.8: Imaging XPS study of the oxidation in GaSe

In order to provide additional confirmation of the results obtained from the Raman and PL experiments, XPS imaging on a tri-layer GaSe at two different times are performed: immediately after exfoliation and after natural oxidation (sample is kept in air for 6 hours in order to facilitate

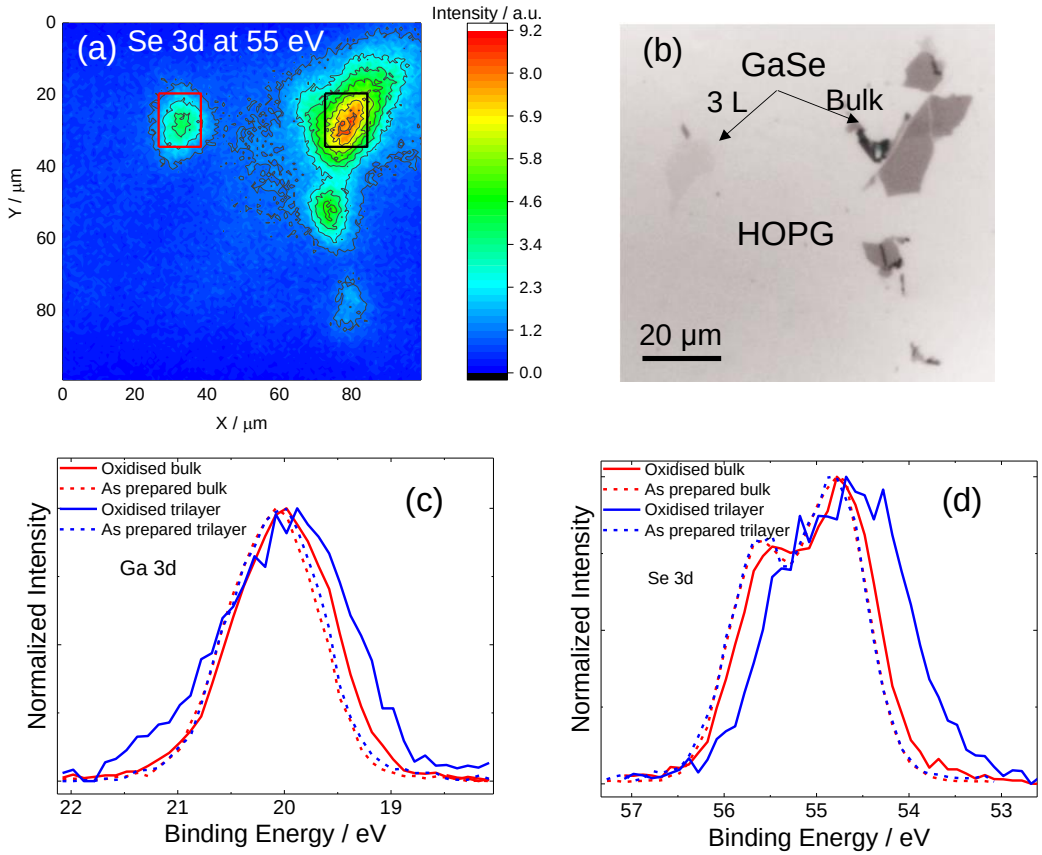

Figure 4.10: Se 3*d* map (a) and optical image (b) of the sample shown in Figure 4.9. XPS spectra of Ga 3*d* (c) and Se 3*d* (d). The XPS measurements were performed in imaging mode and the spectra are averaged from an area over the flakes marked by rectangles.

the natural oxidation). An XPS integrated intensity image of O 1*s* taken from the sample after 6 h of exposure to air is displayed in Figure 4.9a. The sample has three different regimes reflected in the image: bulk like GaSe, 3 L GaSe, and HOPG substrate. Figure 4.9b-c present the AFM image and height profile of the 3 L GaSe flake. The O 1*s* peak extracted from three different positions of the sample (marked by rectangles in Figure 4.9a) immediately after exfoliation and after 6 h of exposure to air are shown in Figure 4.9d-e. From Figures 4.9d-e is clearly evident that both bulk and 3 L GaSe accumulated more oxygen after 6 h of exposure to air; whereas the O 1*s* peak remains almost the same on HOPG. The accumulation of the oxygen by both 3 L and bulk GaSe is an indication of the surface oxidation. In order to investigate the oxidation process in more detail both Ga 3*d* and Se 3*d* core levels are mapped at the two above mentioned times. Figure 4.10a represents the Se 3*d* integrated intensity map ranging from 52 eV to 58 eV, while Figure 4.10b is the optical

image of the sample. Figure 4.10c-d are the XPS spectra extracted from the area marked by the rectangles in the image shown in Figure 4.10a. As shown in Figure 4.10c - d, the XPS spectra of the freshly cleaved bulk and the 3 L GaSe are overlapping almost perfectly. If now one compares the spectra of freshly cleaved and the oxidized bulk flake of GaSe, one can see that both have a similar line shape; even though the peak is slightly broadened. The broadening can be related to the oxidation as seen for the tri-layer. However, for 3 L GaSe the changes in line shape and peak position are far more pronounced. In the case of Se 3*d*, the shifting and broadening of the peak are explained by the formation of *a*-Se, a byproduct of the oxidation process. The doublet is not well separated indicating an amorphization of selenium in good agreement with the Raman spectroscopy results. But in the case of Ga 3*d*, the changes observed are more complex to understand. As can be seen, a shoulder appears at the higher binding energy, indicating the presence of Ga_2O_3 at the surface. However, the overall spectral position moves towards lower binding energy which is unusual for an oxidized material. The exact reason for this unexpected behaviour is not clear at the moment. Drapak *et al.* studied the GaSe surface using XRD after exposure to air and showed that compounds such as Ga_2O_3, $Ga_2(SeO4)_3$, and $Ga_2(SeO3)_3{\cdot}6H_2O$ can form. Given the complexity in which Ga 3*d* chemical state can exist, it is very difficult to deconvolute the Ga 3*d* spectra and clarify the position shifting from XPS results alone. For that, a deeper investigation and dedicated experiments are required which are beyond the scope of this work.

4.9: Summary

The time evolution of GaSe oxidation from bulk to monolayers is investigated by means of Raman spectroscopy, photoluminescence, and XPS. The results show that the oxidation of GaSe is a rapid process with a monolayer reaching an oxidized state almost immediately after exposure to air. For mechanically exfoliated GaSe, the penetration depth of oxidation is determined to be around 3 L with a time required to reach such thickness of roughly five hours. The Raman spectroscopy analysis shows that GaSe decomposes into Ga_2Se_3 and *a*-Se during oxidation. No Raman mode related to Ga_2O_3 is observed due to its transparency under 638 nm excitation. The present work demonstrates the stability of GaSe ultrathin layers and explains as well why the typical Raman modes of GaSe were absent in previous reports on monolayers.[78]

Chapter 5

TERS study of local heterogeneities of MoS_2: Strain

Most of the work discussed in this chapter is published in ***Nano Letters***, 17, 2017, 6027

In this chapter, the investigation of local heterogeneities of MoS_2 using tip-enhanced Raman spectroscopy will be discussed. A 3L MoS_2 combined with a periodic gold nano structured substrate creates a 2D/plasmonic heterostructure. Due to the height difference in the plasmonic substrate, biaxial strains are induced in the MoS_2 sheet during deposition. These strains are highly localized. Therefore, a special method (TERS) is used to detect and quantify the strain. This chapter starts with a motivation of the work. After that, the theoretical background of TERS is introduced. The experimental details and the results are discussed at the end of this chapter.

5.1: Introduction and Motivation

Since the last half decade transition metal dichalcogenides (TMDCs) have been in the focus of extensive research due to their unique physical properties. [12, 29, 46, 66, 105] Following the footsteps of graphene [5] (which does not have a band gap), TMDCs have been studied in various applications such as FETs, [54, 100] photodetectors, [101] photovoltaics, [211] photocatalysis, [103] valleytronics, [104, 212-213] spin valves, [214] piezoelectrics, [215] photonics, [66, 216] flexible electronics [18] *etc.* Due to the strong confinement effect, monolayer TMDCs offer an ideal platform to study quantum confinement semiconductor physics. [29, 217-218] When thinned down from bulk to monolayer, new properties emerge including indirect to direct band gap transition, [29, 46] valley specific circular dichroism, [219] excitonic effects, [47, 220] and enhanced nonlinear optical response. [221-222] The strong Columbic interaction between the electon-hole pairs results in tightly bound excitons which are stable at room temperature thus providing advantages for optoelectronic applications. [12, 216]

Another interesting observation in TMDCs is the ability to tune the electronic properties by applying strain. The band gap of some monolayer TMDCs changes from direct to indirect as the strain increases and they become metallic at a threshold strain. [71, 223-225] Biaxial strain is expected

to have greater influence than uniaxial strain. [226-231] The TMDC materials withstand a large mechanical deformation before rupture; thus, triggering the interest in strain engineering. So far, significant efforts have been devoted to studying the effects of uniaxial and biaxial tensile and compressive strains on the optoelectronic properties of TMDCs. However, experimental studies mostly focused on strain in macro or microscale configurations. [71, 228-229, 231-236] Recently, strain engineering at the nanoscale opened up opportunities to study quantum photonics in TMDCs.[237] Therefore, it is necessary to know the strain acting in these materials with a local spatial resolution in the nanoscale regime.

Among all TMDCs, MoS_2 is the most studied 2D semiconductor. It has an indirect band gap of 1.2 eV in bulk form and a direct optical band gap of 1.8 eV in the monolayer.[46-47] It has a breaking strain of 6 – 11% as measured by nanoindentation and also supported by theory. [238] Raman spectroscopy is one of the most common tools for studying strain in materials. [239-240] Depending on the strain, both peak position and full width at half maximum (FWHM) of the vibrational modes change compared to pristine materials. However, the drawback of conventional Raman spectroscopy, as any other optical spectroscopy method, is that it cannot probe differences in a material below the diffraction limit of the excitation wavelength. Therefore, tip-enhanced Raman spectroscopy has been developed over the last decades to use the localized surface plasmon resonance (LSPR) of a sharp metallic tip as a nano-optical source for signal enhancement. [241] TERS combines both Raman spectroscopy and scanning probe microscopy (SPM). Upon illumination with a suitable wavelength, the electric field strength at the tip apex strongly increases due to LSPR. Therefore, the Raman signal of the probed material is enhanced strongly in the vicinity of the tip. However, TERS is a fairly new technique and is still in its developing phase. Organic molecules, graphene, and carbon nanotubes (CNTs) are the most studied materials in TERS until now.[242-246] Moreover, the characterization of localized strain in crystalline silicon thin films was also demonstrated. [247] Very recently, TMDCs were also probed by TERS to study local heterogeneities such as defects, doping, *etc.* [248-250] In this chapter, the investigation of highly localized strain in ultra-thin MoS_2 when combined with a hexagonal periodic array of gold nanotriangles is discussed.

5.2: Theoretical Background of TERS

The interaction of metals with electromagnetic radiation is mainly dictated by the free electron gas in metals. According to the Drude model, this electron gas oscillates 180° out of phase relative to the driving electric field. Therefore, most metals possess a negative dielectric constant at optical frequencies which causes very high reflectivity. Moreover, at optical frequencies, free electrons can sustain surface or volume charge density oscillations called plasmons with distinct resonance frequencies. Once the metal structures are reduced to a dimension much smaller than the optical

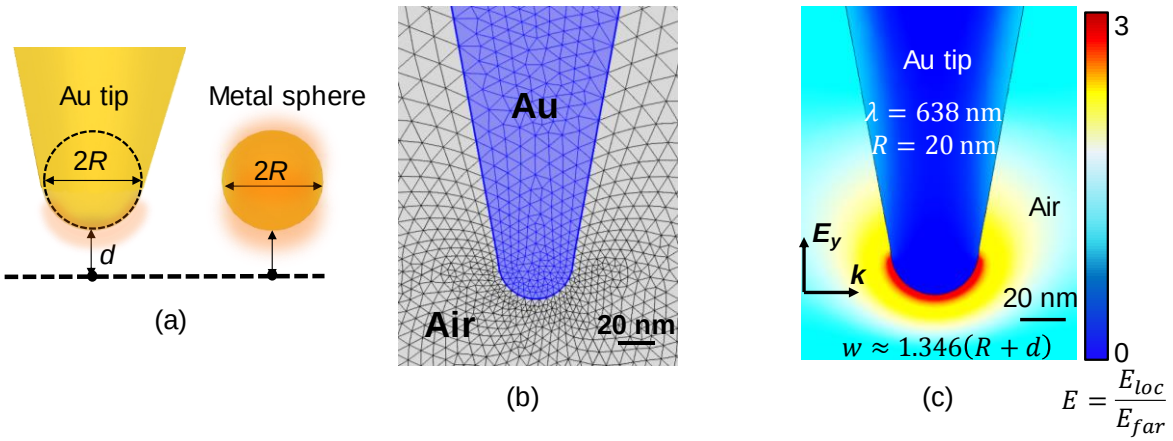

Figure 5.1: Schematic representation of the geometric structure and an equivalent metal sphere of the Au tip (a). Red shaded area demonstrates the electric field distribution. A complete 2D mesh of the FEM model for electric field distribution calculation at the tip apex (b). The simulated electric field enhancement, E around the tip of radius R = 20 nm for an excitation wavelength of 638 nm (c).

wavelength, the confined electron gas is known to exhibit strong interaction at a certain optical frequency which is also known as localized surface plasmon resonance (LSPR) and those metal nanostructures are called plasmonic structures. LSPRs have been studied over the last few decades due to their ability to fundamentally alter the light mater interaction and their potential application in surface enhanced Raman spectroscopy (SERS).[251-255] Like SERS, tip enhanced Raman spectroscopy (TERS) is also based on the LSPR of the sharp tip apex used in scanning probe microscopy (SPM) techniques. A sharp metal tip (such as Ag or Au) is positioned at the centre of the laser focus and the electromagnetic field at the tip apex is confined and enhanced due to the combination of LSP and lightening rod effect. As a consequence, the tip apex will serve as a nano-optical source and enhance the Raman signal from the specimen in the vicinity of the tip-apex. The concept of TERS was first proposed by Wessel in 1985 [192] and was experimentally realised in 2000.[256] TERS combines the chemical sensitivity of SERS with spatial resolution of SPM and enables chemical imaging of the sample surface on the nanometer scale where conventional Raman spectroscopy fails due to the diffraction limit of light.

In order to understand the theory and explain the experimentally observed TERS results, a detailed theoretical study is conducted by solving Maxwell's equations numerically using the finite element method (FEM). In classical theory, the plasmonic response of a nanostructure includes the electric field distribution and spectral response of the field around it. Figure 5.1a displays the schematic of the geometry used for the calculation. The calculation is conducted by a commercially available

simulation platform, COMSOL multiphysics 5.2a. The desired structures are created directly in COMSOL using a 2D model. Figure 5.1b presents a mesh image of a gold tip of radius, $R = 20$ nm. A trigonal element type is chosen for meshing with a smallest element size of 0.1 nm. In order to simulate the experimental conditions, a plane wave excitation of 638 nm with an electric field component of $E_y = 1\,V \cdot m^{-1}$(parallel to the tip longitudinal axis) is applied in the model. A Perfectly matched layer (PML) is chosen as the boundary condition to absorb all the outgoing waves. The model is solved using Maxwell's equation in the frequency domain as follows:

$$\nabla \times \mu_r^{-1}(\nabla \times \boldsymbol{E}) - k_0^2 \left(\varepsilon_r - \frac{j\sigma}{\omega \varepsilon_0}\right)\boldsymbol{E} = 0 \qquad 5.1$$

where $\omega, \mu_r, \varepsilon_r$, and σ are the excitation frequency, relative permeability, relative permittivity, and electrical conductivity respectively. The frequency dependent relative permittivity of Au, $\varepsilon_{Au} = \varepsilon_r - i\varepsilon_i$ is taken from Johnson *et al.* [257] The calculated confined electric field at the tip apex is displayed in Figure 5.1c. The calculation of the confined electric field (which is also known as local electric field, E_{loc}) can be simplified by an equivalent sphere approximation. Hence, the intensity of E_{loc} is described by its polarizability due to incident electric field (which is also known as far electric field or far field, E_i) as follows:[258]

$$\alpha_m = 4\pi\epsilon_0 R^3 \frac{\epsilon_{Au} - 1}{\epsilon_{Au} + 2} \qquad 5.2$$

where $\varepsilon_0$is the permittivity of the vacuum. The local electric field, $\boldsymbol{E}_{loc}$at a position $\boldsymbol{r}$ near the tip apex is obtained by the polarised dipole moment ($\boldsymbol{P}_m = \alpha_m \boldsymbol{E}_i$) as: [258-259]

$$\boldsymbol{E}_{loc} = \boldsymbol{E}_i + \frac{\epsilon_{Au} - 1}{\epsilon_{Au} + 2}\left(\frac{R}{r}\right)^3 [3(\boldsymbol{E}_i \cdot \boldsymbol{r})\boldsymbol{r} - \boldsymbol{E}_i] \qquad 5.3$$

The full width at half maximum of E_{loc} can be simplified as, $w \approx 1.35(R + d)$,[258] with d being the distance from the tip apex. The maximum field intensity is obtained when $d = 0$ and the minimum width of the confined field is proportional to R. Therefore, in general approximation when only the tip is considered in a TERS experiment, the spatial resolution is limited by the tip radius. However, in practise both the local field intensity and the spatial resolution in TERS depend not only on the tip but also on the optical properties and geometry of the surface. Both can be improved by forming

 The COMSOL Multiphysics 5.2a software used in this thesis work is owned by Semiconductor Physics group of Chemnitz University of Technology

a nano gap (image dipole) in a configuration of so-called gap-mode TERS as shown in Figure 5.2a. In such a case the local electric field intensity can be expressed as: [260-261]

$$E_{loc} = \left(\frac{2R + d}{d}\right) E_i \qquad 5.4$$

With $d \approx 0$, the equation 5.4 becomes,

$$E_{loc} \approx \left(\frac{2R}{d}\right) E_i \qquad 5.5$$

Therefore, the local electric field is dramatically enhanced when the tip moves closer to the sample. The full width at half maximum of the confined electric field is then given by:

$$w = 2\sqrt{Rd} \qquad 5.6$$

In such cases, the spatial resolution of a TERS experiment is much better than the tip radius. The simulation of the local electric field distribution in gap mode TERS is presented in Figure 5.2b-d. Figure 5.2b presents the mesh image of a tip-sample system used in the simulation. The smallest mesh element is chosen to be 0.1 nm to resolve finest details in the simulation. For better understanding, Si with a native oxide, a common substrate in TERS experiments is introduced in the simulation and compared with a flat gold substrate. The gap between the tip and the substrate is 1 nm. As can be seen finite element sizes are much smaller than the narrow gap between tip and sample to give an accurate result in the simulation. Figure 5.2c present the simulation result of an Au-Au system. Comparing the simulation results between Figure 5.1c and 5.2c, one can see that the electric field intensity is enhanced by a factor of 10 in the so-called gap mode TERS. The enhancement is due to the local potential gradient at a distance, d (in this case 1 nm) induced by the electric field at the tip apex, E_{loc}. The width of the confined electric field is also decreased dramatically. In order to determine the width of the confined electric field a cross section is taken along the spatial distribution of the electric field 0.1 nm below the tip apex (white dashed line in Figure 5.2b-c). A Voigt function is used to fit the field distribution in both cases. The width of the confined electric field in case of Au-Au tip-sample system is determined to be (8.6 ± 0.1) nm; very good agreement with equation 5.6. In the case of the Au-Si tip-sample system, the electric field

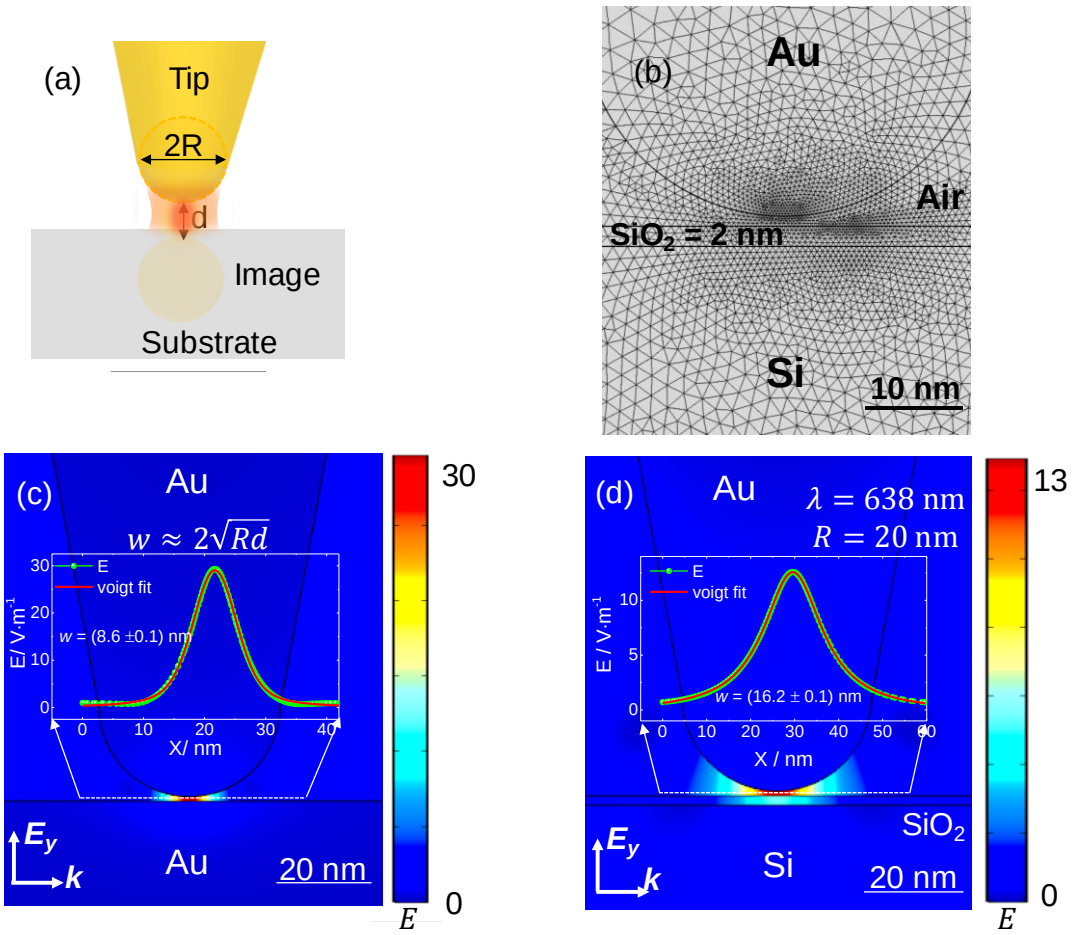

Figure 5.2: Schematic of the image dipole formation between a tip and a metal substrate (a). The red shaded area demonstrates the confined field. The mesh image of the tip-sample system used in the simulation in Figure 5.2d (b). Electric field enhancement map of an Au-Au system (c) and Au-Si system (d). The definition of E is given in Figure 5.1. The tip-sample gap is 1 nm. A native oxide of 2 nm is assumed in the simulation in 5.2d. Both intensity and width of the confined electric field is improved compared to the simulation result shown in Figure 5.1b. The width of the confined electric field, w is shown by an arrow in (c).

amplitude is reduced by a factor of 2.3 due to reduced coupling. This is owing to the fact that 1) Si is a semiconductor with much less density of surface conduction electrons, and 2) additionally, the surface of Si is passivated by a native oxide of 2 nm which exponentially decays the field going through it. Therefore, the dipole gradient at the surface is also reduced. Due to the same reason, the width of the confined electric field is also broadened (see Figure 5.2d). The width is determined to be (16.2 ± 0.1) nm from the calculation.

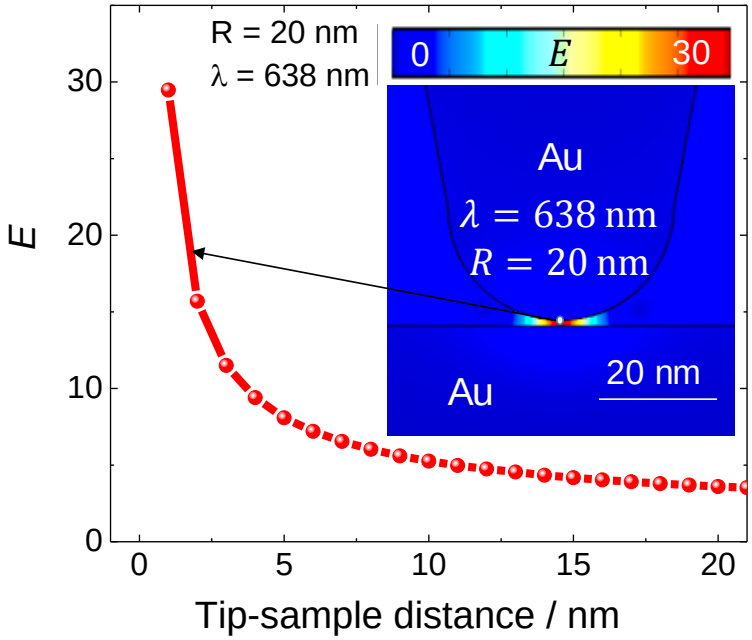

Figure 5.3: Local electric field enhancement, *vs* tip-sample distance. The white dot is the position in the model from where the field is calculated at each tip-sample distance. The definition of E is given in Figure 5.1.

The local electric field dampens exponentially by a factor of $E_{loc} \sim e^{(kd)}$, with k is the wavenumber which determines the propagation or decay length of the electric field and d is the tip-sample distance.[259] Figure 5.3 shows the calculated local electric field enhancement E with respect to d for the system described in Figure 5.2c. As can be seen, E dampens dramatically (about 70%) if the tip-sample distance changes from 1 nm to 5 nm. Since the TERS enhancement is described by E^4, the Raman intensity detected from the probing molecules would decrease by 99% at 5 nm gap. At 20 nm tip-sample distance, E is equal to the value calculated in Figure 5.1c; meaning that there is no tip-sample coupling at this tip-sample distance. If one now considers the equations 5.5 and 5.6, the maximum intensity and spatial resolution of a TERS experiment can be achieved at $d = 0$. In such a case, the intensity of the local electric field would go to infinite and the width of the confined electric field becomes zero. Both of these are obviously not realistic. When the tip-sample distance enters the sub-nanometer gap, classical models cannot explain the surface plasmon anymore. The phenomena can be explained properly with the aid of quantum mechanical models. At sub-nanometer gap, quantum effects such as electron tunnelling and nonlocal screening effects (interaction with all neighbouring charged particles) become important and influence the plasmonic response of the nanostructures. Therefore, there is a minimum tip-sample gap (in the range of 0.3 nm), for which one can get maximum TERS enhancement and spatial resolution.

Below that limit both enhancement and spatial resolution decrease due to quantum confinement effects (more details can be found in the references[258, 262-264]).

TERS enhancement factor: The simplified form of TERS enhancement is expressed as

$$E = \frac{E_{loc}}{E_i} \tag{5.7}$$

According to equation 3.11 TERS enhancement factor in terms of electric field can be written as

$$EF = \frac{E_{loc}^4}{E_i^4} = E^4 \tag{5.8}$$

However, in practice, dealing with the Raman intensity is more straightforward. Therefore, the calculation of the TERS enhancement factor using the Raman intensity is more popular. The TERS enhancement factor in terms of Raman intensity can be written as

$$EF = \left(\frac{I_{near}}{I_{far}}\right)\frac{V_{far}}{V_{near}} \tag{5.9}$$

in which, I_{near}, and I_{far} are the Raman intensity of the probed material when tip is in contact with the sample and far away from the sample respectively. V_{far} is the volume probed by far field illumination, and V_{near} is the volume probed by local field. The first term on the right-hand side of equation 5.9 is also known as TERS contrast which determines the quality of the TERS image. Since the thickness of the probed material is often ranging from few angstroms to few nanometers in TERS configuration, the depth is always ignored. Therefore, equation 5.9 becomes

$$EF = \left(\frac{I_{near}}{I_{far}}\right)\left(\frac{A_{focus}}{A_{tip}}\right) \tag{5.10}$$

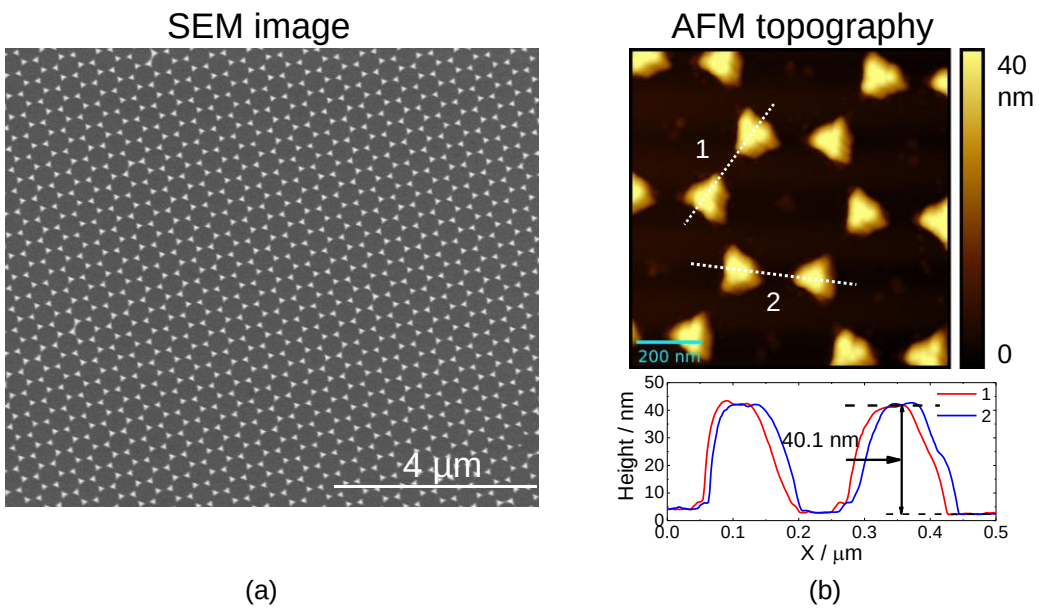

Figure 5.4: SEM image (a), and AFM topography and height profile (b) of the gold nanotriangles on silicon substrate prepared by nanosphere lithography. The sides and height of the nanotriangles are approximately (120 ± 5) nm and (40 ± 1) nm.

where, A_{focus} is the laser illuminated area, and A_{tip} is the cross section of the tip apex.

5.3: Experimental Details

Preparation of the plasmonic substrate: The plasmonic substrate used in this work is made of Au nanotriangles. These nano triangles are prepared by nanosphere lithography (NSL). At first an aqueous suspension of commercially available 450 nm monodispersed polystyrene spheres (PS) from Postnova Analytics GmbH (art. No. Z-PS-POS-006-0,450) is diluted in 1:1 ratio with ethanol. The solution is then used to produce a large area monolayer PS on a water surface by a method adopted from Vogel *et al.* [265] After that the monolayer is collected on a p-type silicon (111) substrate of 1x1 cm² size by immersing it into the DI water and then slowly lifting it from underneath of the PS monolayer as it adheres to the substrate. Once the substrate is dry, it is then transferred to a metal deposition chamber where gold is evaporated at normal incidence and at a base pressure of 10^{-6}mbar. After the evaporation, the PS layer is mechanically removed by scotch tape. We obtain

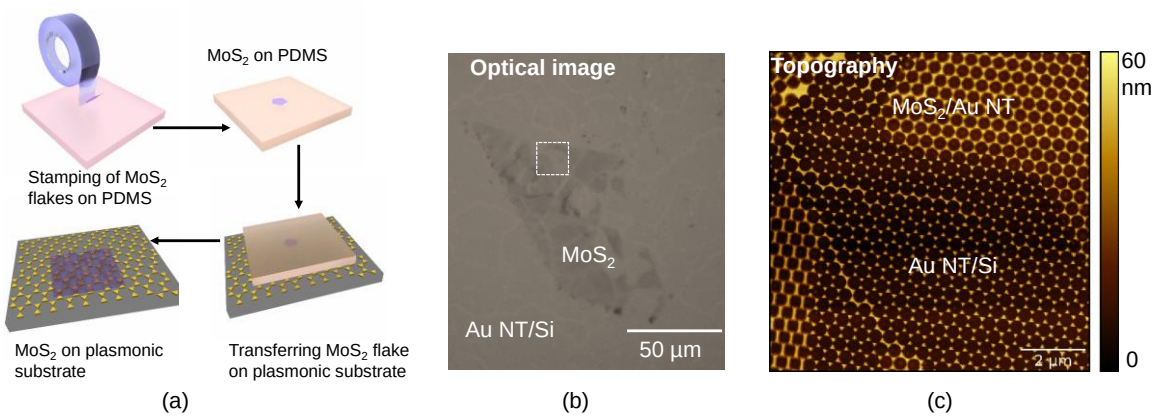

Figure 5.5: Schematic of MoS_2 transfer method on plasmonic substrate (a). Optical image (b) and AFM topography of the area marked by a white dashed rectangle in (b) (c) of the MoS_2 flake transferred onto plasmonic substrate.

a hexagonally packed periodic array of gold nanostructures with triangular shape ("nanotriangles", NTs) on the Si substrate. The sides of the triangles are approximately 120 nm in length and the height is 40 nm as deduced from scanning probe microscopy observations. The scanning electron microscopy (SEM) and AFM images of such structure are presented in Figure 5.4.

Sample preparation: An ultrathin (3 layers) MoS_2 film is transferred onto the plasmonic substrate by the deterministic transfer technique.[266] The transfer method is based on the mechanical exfoliation technique described in section 2.3. A single crystal 2H-MoS_2 is used for the experiment. The bulk crystal of 2H-MoS_2 was purchased from 2D Semiconductors. At first MoS_2 flakes of different thicknesses are deposited onto a polydimethylsiloxane (PDMS) substrate by scotch tape technique. Upon optical investigation, ultrathin MoS_2 flakes are identified and later transferred to the plasmonic substrate by pressing gently the PDMS substrate onto the sample. The schematic of the sample transfer process is presented in Figure 5.5a. The optical image of the MoS_2 flake on the plasmonic substrate is shown in Figure 5.5b. The AFM topography of the flake within the rectangular box marked by white dashed lines in the optical image is displayed in Figure 5.5c. The AFM image nicely resolves both the hexagonal array of the Au nanotriangles and the MoS_2 flake on top of it. The AFM image is scanned in tapping mode AFM using a commercially available Si tip of a nominal radius of 8-10 nm purchased from Tipsnano.

 The sample is prepared in collaboration with Tobias Korn of Universität Regensburg, Germany

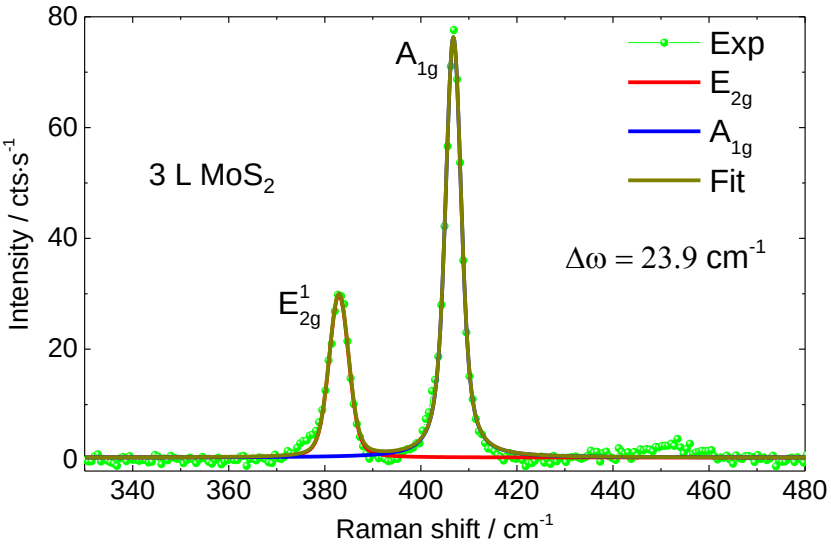

Figure 5.6: Micro Raman spectra of the MoS_2 flake on plasmonic substrate to confirm the thickness. In order to determine the frequency difference accurately, the spectrum was fitted with a Voigt function. The frequency difference between the two Raman modes is determined to be (23.9±0.1) cm^{-1} equivalent to 3L of MoS_2.

Determination of the layer thickness using Raman spectroscopy: Nondestructive Raman spectroscopy has been widely used to determine the thickness of two-dimensional materials including graphene and TMDCs. In this study, micro Raman spectroscopy in the backscattering geometry is deployed to determine the thickness of the MoS_2 flake under investigation. For this, a solid-state laser line of 532 nm excitation is combined with a 2400 l/mm grating for dispersing the scattered Raman signal. This configuration provided a spectral resolution of 1 cm^{-1} determined from the width of the gas emission line of a Xe calibration lamp. A Horiba Xplora Raman system coupled with an electron multiplying charge-coupled detector is used for the measurement. The laser power used for the measurement is 105 µW to avoid any photoinduced damage of the sample. A typical Raman spectrum of MoS_2 taken on the flake is presented in Figure 5.6. There are four first order Raman modes in 2H-MoS_2. The interlayer shear breathing mode (E^2_{2g}) around 30 cm^{-1} is out of reach because of the cut-off of the edge filter. The in-plane, E_{1g} mode is forbidden in back scattering geometry. The two mostly studied Raman modes are E^1_{2g} and A_{1g} as shown in the Raman spectrum. The A_{1g} mode hardens with increasing number of layers; whereas, the E^1_{2g} mode softens. The opposite trend of these two modes leads to an increase in frequency difference with increasing number of layers and is used to determine the layer thickness. [106, 267-268] In order to determine the frequency difference accurately, the Raman spectrum is fitted using Voigt functions. In this study, the frequency difference between the two

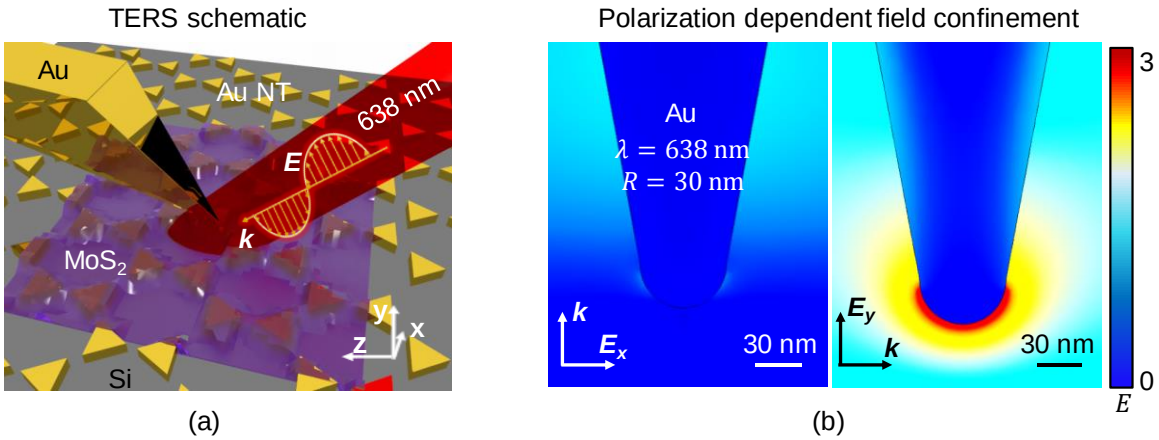

Figure 5.7: Schematic of the experimental TERS set up (a). Incident light is polarized along the tip longitudinal axis to give TERS signals. COMSOL simulation of polarization dependent local field enhancement at the gold tip apex (b). Tip radius is assumed to be 10 nm. Since $\sigma_{yy} \gg \sigma_{xx}$, local field enhancement is much higher when the incident light is parallel to the tip long axis. The definition of E is given in Figure 5.1.

modes is determined to be (23.9 ± 0.1) cm^{-1} equivalent to 3L of MoS_2. [106, 267] The hardening behaviour of the A_{1g} can be explained by the restoring force constant perpendicular to the basal plane due to van der Waals interactions with increasing number of layers. On the other hand, since the in-plane E^1_{2g} mode involves the vibration of both Mo and S atoms in the basal plane, it is strongly influenced by the long-range coulomb interaction of the Mo atoms. Therefore, with the increase number of layers, the Mo-Mo interaction decreases due to increased screening and thus softens the mode.

TERS Methods: TERS measurements are performed on a NanoRaman Platform (HORIBA Scientific/former AIST/NT) consisting of an atomic force microscope (SmartSPM) combined with a Raman spectrometer (Xplora) inside illumination geometry. The schematic of the experimental setup is displayed in Figure 5.7a. Excitation and collection is realized through a long working distance objective, 100x, 0.7 NA. The angle of incident and collected light is 65° with respect to the surface normal. Therefore, the laser focus is non-symmetric and enlarged to an ellipsoidal area of 1.7 μm^2 approximately. A *p*-polarized monochromatic laser of 638 nm wavelength is focused onto an inclined gold tip. This excitation geometry enables the electric field to be polarized parallel to the tip longitudinal axis. The tip is highly anisotropic with polarizability along the long axis being much stronger than along the short axis ($\sigma_{yy} \gg \sigma_{xx}$) as shown in Figure 5.7b. Figure 5.7b shows a COMSOL simulation of the polarization dependent electric field confinement at the apex of a gold

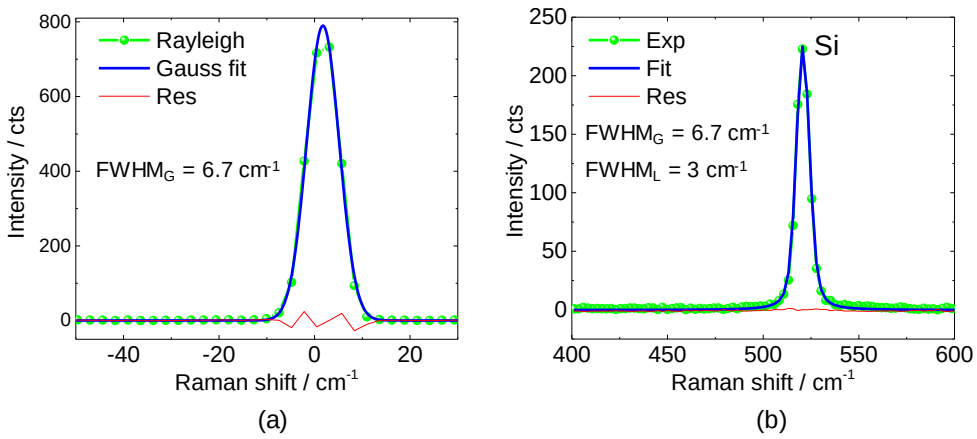

Figure 5.8: Determination of spectral resolution (a) and fit parameters (b) for the TERS spectrum analysis. Both Rayleigh and Si peaks are acquired using the same experimental parameters used in the TERS measurements. The red curve is the fit error or residual of the fitting.

tip of 30 nm radius (similar to the tip radius used in the experiment). As can be seen, when the excitation field is polarized along the tip short axis, the local field enhancement factor is comparable to the far field. Moreover, the enhanced field is far away from the apex confined at the sides of the tip. Therefore, it is essential for the incident light to be polarized along the tip longitudinal axis in order to obtain TERS signal from the sample. Thus, the TERS geometry adopted in this study gives a high electric field enhancement in the vicinity of the tip apex due to the LSPR and lightning rod effect.[269]

TERS experiments are conducted using a commercially available gold TERS probe with a radius of 25 – 30 nm purchased from HORIBA. As discussed in section 5.2, the maximum enhancement occurs when the tip is in contact with the sample (strongest enhancement at a gap in the range of 0.3 nm). Therefore, it is desirable to operate the system in contact mode while performing TERS imaging. However, in this study, contact mode scanning is abstained in order to avoid surface modification by the tip. Instead, TERS imaging is performed in the so-called hybrid mode. During TERS measurements the system is running in intermittent contact (AC) mode (or tapping mode) and the spectra are taken at the moment of the tip touching the surface. The contact time (or touching time) is defined by the spectral acquisition time which is 0.5 s. TERS images are acquired with a 10 nm step size over an area of 0.7 x 0.7 μm² using a 638 nm excitation. The Raman signals are dispersed by a 1200 l/mm grating onto an electron multiplying charge coupled detector (EMCCD).

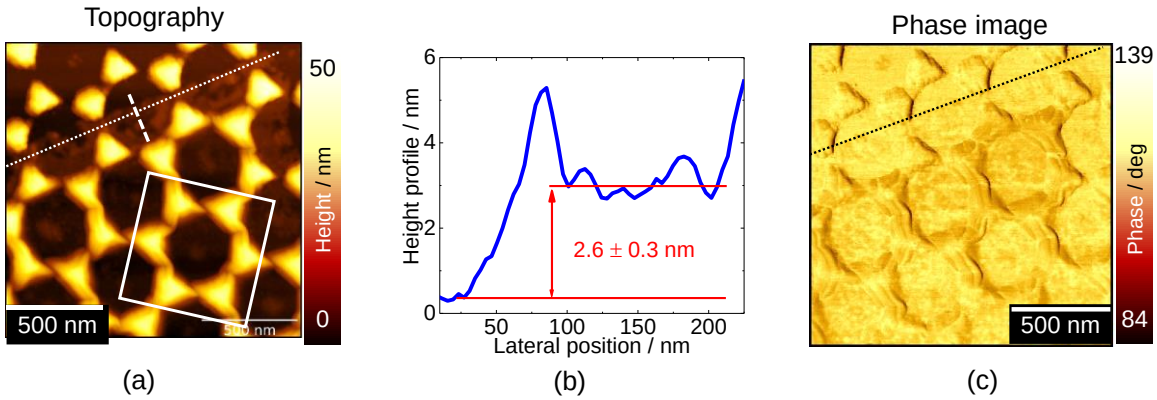

Figure 5.9: The AFM topography of the MoS_2/Au NTs heterostructure (a). The height profile of the flake along the white dashed line (b). The hump at the border is due to sharp edge created during exfoliation. Corresponding phase image of the heterostructure (c). The dotted lines in (a) and (c) are drawn as a guide for the eye to distinguish the border of MoS_2**.** The white rectangle is the area where TERS imaging is performed.

Determination of spectral resolution and fit parameters: In order to analyse the TERS spectra accurately, the spectral resolution of the experiment is determined. For that, the Rayleigh line is acquired using the same TERS experimental parameters. Figure 5.8a shows experimental and the Gaussian fit of the Rayleigh line. The $FWHM_G$ is determined to be 6.7 cm^{-1}, which is the spectral resolution for the TERS experiments. After that, using a Voigt function, a silicon peak is fitted from the same substrate using the same experimental parameters. In this fitting the Gaussian contribution is fixed to 6.7 cm^{-1}. Figure 5.8b represents the experimental and fitted silicon peak. The Lorentz contribution of the silicon peak is determined to be 3 cm^{-1} ($FWHM_L$). In the fitting process of this investigation, 6.7 cm^{-1} and 3 cm^{-1} are set as the base value of $FWHM_G$ and $FWHM_L$ respectively.

5.4: AFM study of the heterostructure

Figures 5.9 show the AFM topography, height profile, and phase image of the heterostructure. The optical image and the extended topography of the sample are presented in Figure 5.5. The gold nanotriangles (NTs) form an open hexagonal periodic array on the silicon substrate. Once MoS_2 is put on gold, it bridges the gap between gold triangles making closed hexagonal units visual in the AFM topography (see Figure 5.9a and also 5.5c). A white dotted line is drawn as a guide for the eye to distinguish the border of MoS_2 flake in Figure 5.9a. The height is measured to be (2.6 ± 0.3) nm

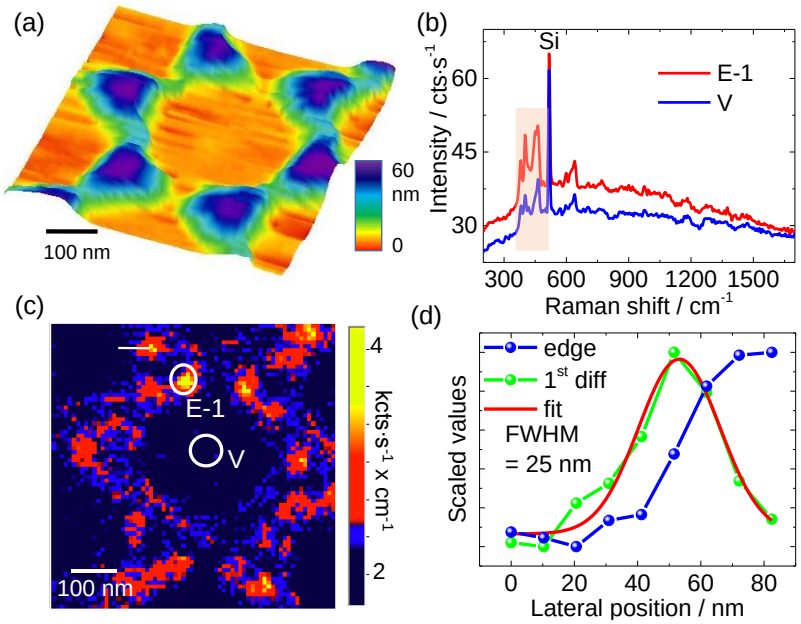

Figure 5.10: AFM topography of the area of interest (AOI) during TERS imaging (a). The AOI is marked by a rectangle in Figure 5.9a. The averaged TERS spectra (b) of the two different area noted in the TERS intensity image (c) of MoS_2 acquired from the spectral range 360 cm^{-1} to 480 cm^{-1}. Each area is averaged over 20 data points. The spectral range is marked by a shaded rectangle in (b). The circles are the areas from which Raman spectra are averaged to quantify the localized strain in MoS_2 discussed in section 5.6. The intensity profile of the cross section along the white solid line in the TERS image and the fitting to determine the spatial resolution (d).

along the white dashed line in the AFM topography, equivalent to 3 L of MoS_2. This is in good agreement with the Raman measurement discussed in Figure 5.6. As can be seen from the topography, the MoS_2 flake follows the shape of the gold nanotriangles and is sharply bent in between the triangles. Since the phase image is more sensitive to adhesion, the inhomogeneity is more clearly visible in Figure 5.9c. Both, topography and phase image show two distinct conditions of MoS_2: 1) at the valley with an unstrained planar surface and 2) on top and in between the gold NTs, where it is deformed.

5.5: TERS imaging of the heterostructure

The morphology of the heterostructure reveals the inhomogeneity in the MoS_2 film while following the hexagonal arrays of Au NTs. TERS imaging is performed on a single hexagonal unit shown in

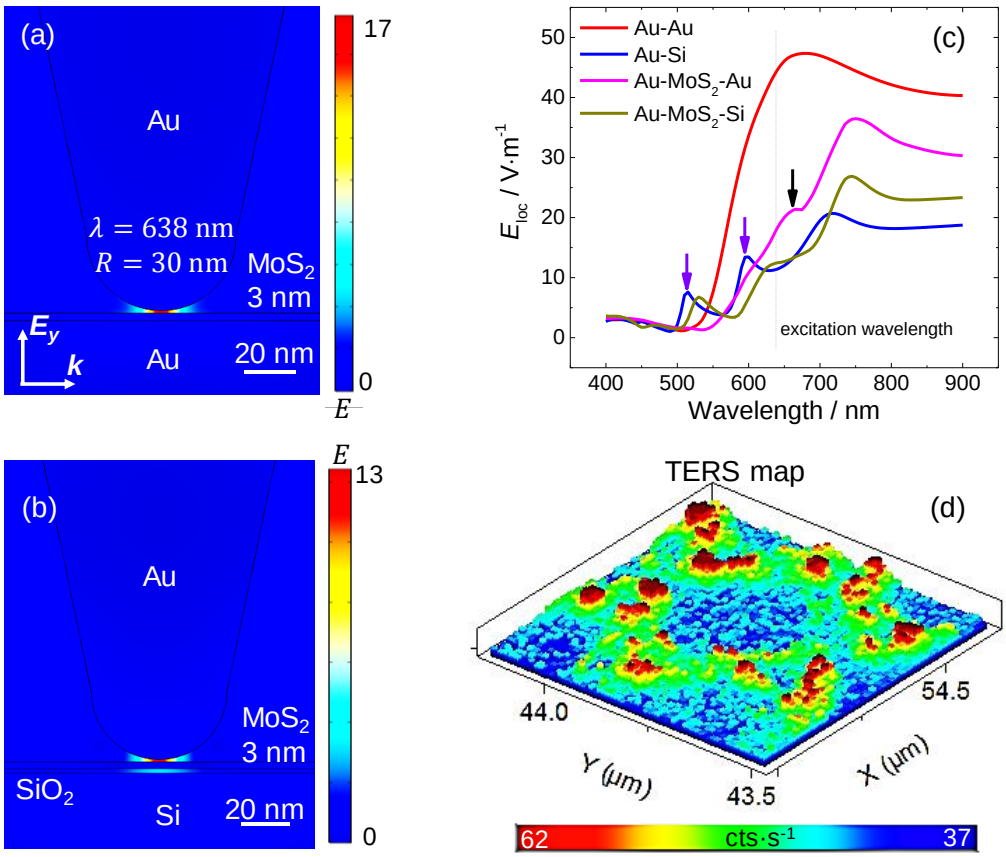

Figure 5.11: COMSOL simulation of experimental system shown in Figure 5.10. Au-MoS_2-Au (a) and Au-MoS_2-Si (b). The tip-sample gap is 1 nm. The definition of E is given in Figure 5.1. The amplitude of E_{loc} is similar in both (a), and (b). Wavelengths sweep of E_{loc} over a range of 400 – 900 nm. Violet arrows indicate the higher harmonics of the effective LSPR. The black arrow is the position of optical absorption of MoS_2. Pseudo 3D map of TERS image shown in 5.10c (d). The scale bar is adjusted to the TERS signal of MoS_2 on silicon substrate.

Figure 5.9a to study the heterogeneity of the MoS_2 film. The AFM topography, representative TERS spectra, and a Raman intensity map of the hexagon unit are shown in Figure 5.10a-c. The TERS image is taken with respect to the Raman signal of MoS_2 within the area of the shaded rectangular box in Figure 5.10b. The two TERS spectra are averaged within the circular areas E-1 and V marked in Figure 5.10c. As can be seen, the TERS image nicely follows the AFM topography. The highest Raman signal enhancement is observed at the corners of gold triangles. This can be understood by the strong electric field enhancement due to the coupling between the sharp metallic tip and the triangle's corners due to the lightening rod effect (independent of LSPR).[269-270] In order to determine the spatial resolution of the measurement, a cross section is taken at the edge of one of the enhanced spots as shown in the Figure 5.10c (the white solid line). The Raman intensity profile of the edge and the fitting of it is displayed in Figure 5.10d. The first-order derivative of the

intensity is a Gaussian profile and the full width at half maximum (FWHM) of the fit is determined to be (25 ± 3) nm. This is considerably larger than the theoretical prediction made in section 5.2 for gap mode TERS. The true spatial resolution of the TERS map could be determined from a sharp edge. In this case however, the edges of the gold triangles are smooth because of the deposition of the MoS_2 film. Hence the FWHM of the first order derivative of the intensity profile is limited by the size and shape of the edge and thus considerably larger than the expected value. The true spatial resolution of the TERS map is therefore smaller than 25 nm.

Another interesting observation of the TERS image in Figure 5.10c is that the Raman enhancements of MoS_2 on the flat surface of the gold triangles and on top of silicon at the valley are not significantly different. This is contradictory to the theory of gap mode TERS discussed in section 5.2, Figure 5.2. In order to understand the physics behind it, similar systems are modeled in COMSOL. The tip radius is assumed to be 30 nm and a 3 nm thick film of MoS_2 is considered as the top layer of the sample (similar thickness of the MoS_2 flake in the experiment). The tip-sample gap is 1 nm in the modelling. The dielectric functions of MoS_2 are adopted from Beal *et al.*[271] The 2D plots of calculated local electric field distribution of the two systems are presented in Figure 5.11a-b. It can be seen that the strongest electric fields are near the apex of the tip in both cases with similar amplitude. Therefore, the local field enhancement phenomena in both cases can be explained by the fact that the effective plasmonic response for both sets of geometries are dominated by the MoS_2 film of 3 nm. The TERS enhancement ratio of MoS_2 between the signals obtained on top of flat surface of gold triangles and on silicon at the valley is estimated by E^4 to be

$$ER = \left(\frac{E_{Au-MoS_2-Au}}{E_{Au-MoS_2-Si}}\right)^4 = 2.8 \qquad 5.11$$

Hence, the TERS signal on flat surface of gold triangles should be 2.8 times higher. To get a better understanding of the effective plasmonic response of the systems, wavelength dependent E_{loc} distribution is calculated over a range of (400 – 900) nm for all combinations of tip-sample systems. Figure 5.11c shows the calculated spectral dispersion of the local electric field. In the case of the Au-Au tip-sample system, the plasmonic resonance occurs around 680 nm. Whereas, for the Au-Si system the LSPR is 2.3 times weaker and shifted to red (around 710 nm). In addition to the LSPR, two higher modes of plasmon excitation around 600 nm and 510 nm are also observed. However, the effective LSPR is strongly influenced by the introduction of 3 nm MoS_2 in between the tip and the substrate. In the case of the Au-MoS_2-Au system, the effective LSPR is shifted to 749 nm and the amplitude of E_{loc} is also decreased. The spectral dispersion of E_{loc} is also red shifted for the Au-MoS_2-Si system with an increase of electric field. The effective LSPR for this system is

at 743 nm. The position of the effective LSPR in both cases is also a very good indication that the coupling between the tip and the sample is dominated by the trilayer MoS_2 film, since the LSPR is determined by,[259]

$$\omega_{LSPR} = \frac{\omega_p}{\sqrt{1 + 2\varepsilon_d}} \qquad 5.12$$

where, ω_p is the plasma frequency of the metal and $\varepsilon_d = \varepsilon_d' + i\varepsilon_d''$ is the dielectric function of the environment. As a result, the TERS enhancement of MoS_2 in both cases is similar. Figure 5.11d is a pseudo 3D map of the TERS image shown in Figure 5.10c. The scale bar is adjusted to the TERS signals of MoS_2 on silicon substrate at the valley. The TERS enhancement ratio is determined to be 1.6 by following equation:

$$E_{TERS} = \frac{I_{MoS_2/flat\ Au}}{I_{MoS_2/Si}} \qquad 5.13$$

The deviation between calculation and the experiment can be due to the fact that an ideal sphere is assumed at the tip apex in the simulation. Whereas, in the practical situation the tip shape is more uncertain which may lead to different plasmonic enhancement.

Determination of enhancement factor: According to equation 5.10, both near field and far field Raman signals are required to determine the real TERS enhancement. During the time of this investigation, it was not possible to acquire the far field Raman signal simultaneously due to instrumental limitations. However, the instrument was modified later to accommodate such experimental option which will be discussed in the next chapter. Thus, it is not practical to determine the true enhancement factor of the TERS measurement in this study. Nevertheless, the relative enhancement factor can be determined using TERS contrast (the ratio of Raman intensity of MoS_2 on the highest enhanced area to the valley (on silicon)). The TERS contrast is determined to be 2.5. The illuminated area is 1.7 μm^2 as discussed in section 5.3. The tip cross section is determined from πR^2, with $R = 30$ nm. The relative enhancement factor is therefore determined from equation 5.10 as

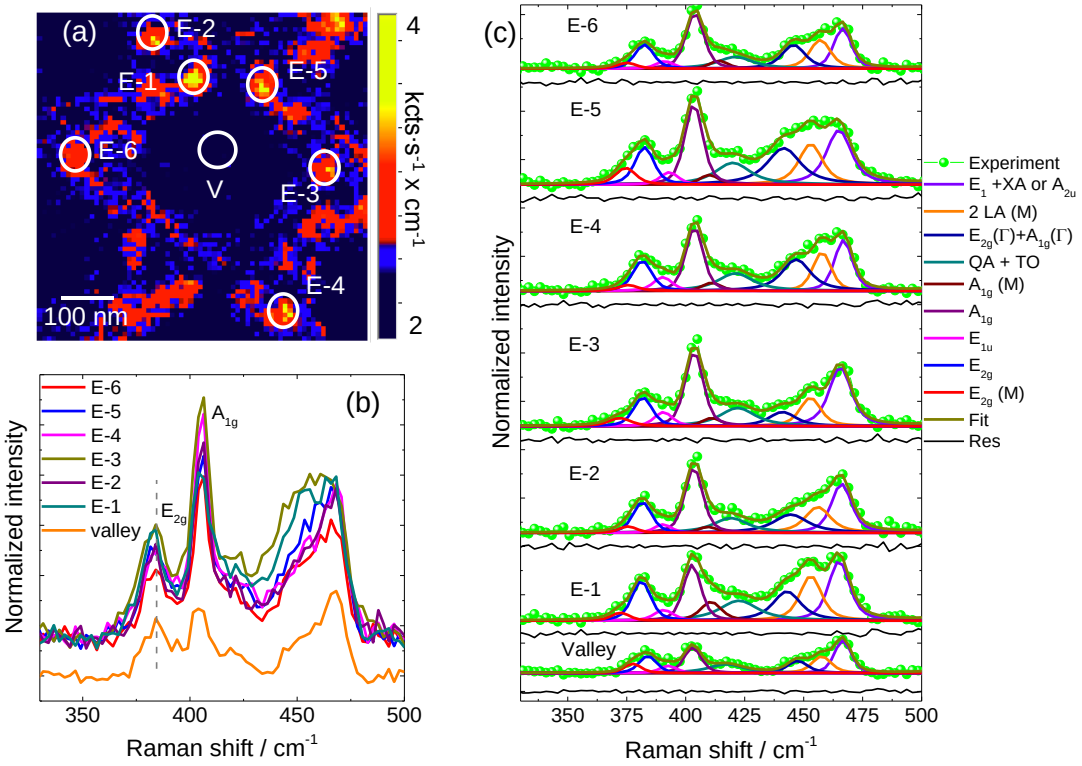

Figure 5.12: TERS image shown in Figure 5.10c (a). Raman spectra are taken from areas marked by circles and displayed in (b). The spectra are presented after background subtraction. Raman spectra are deconvoluted using Voigt functions (c). Fitting parameters are described in Figure 5.8.

$$EF_{relative} = 2.5\frac{1.7 \times 10^{-12} m^2}{2.8 \times 10^{-15} m^2} = 1517 \qquad 5.14$$

5.6: Investigation of localized strain

In order to quantify the strain in MoS_2 on top of gold triangles seven spectra are taken from the TERS image as shown in Figure 5.12a. Each spectrum is averaged over the circle areas on the triangles and the valley. TERS spectra are presented in Figure 5.12b after the background subtraction. Depending on the excitation wavelength, the Raman spectra of MoS_2 show different profiles. As discussed in section 5.3, 2H-MoS_2 has four first-order modes denoted by E^2_{2g}, E_{1g}, E^1_{2g}, and A_{1g}. However, in resonant Raman conditions (with excitation close to the optical band gap), a number of additional features are also excited. In this investigation, as many as seven second-order Raman modes are observed in the measured spectral range. Therefore, the TERS spectra

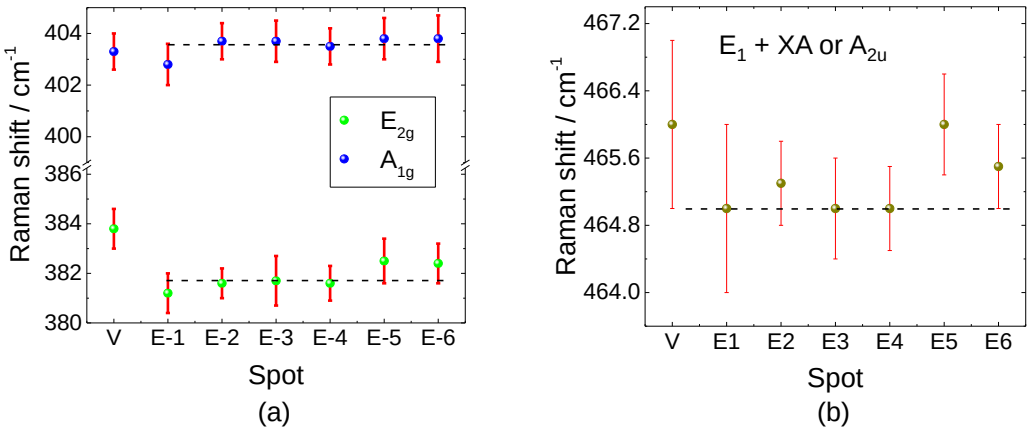

Figure 5.13: Fitted peak position of two first order Raman modes (a) and A_{2u} mode (b). The black dashed line is the averaged peak position in each case.

were deconvoluted with nine peaks. The as measured spectra and the fitted peaks are displayed in Figure 5.12c. The fitting procedure was carried out using a Voigt function with the base parameters determined in section 5.2, Figure 5.8. The additional features were measured previously and their origin was discussed.[113, 232, 272-276]The origin of the Raman band around 378 cm^{-1} is the in-plane phonon, E_{2g} at the M point of the Brillouin zone (BZ).[232, 272] Some reports also term it as the Davydov splitting of the phonon of E_{2g} (Γ) mode at 383 cm^{-1}.[113, 273-274] The band around 390 cm^{-1} is a Raman-inactive, E_{1u} mode in bulk MoS_2 excited due to resonant condition. The origin of the Raman band around 409 cm^{-1} is at the proximity of M point in the BZ scattering from A_{1g} phonon analogous to the mode E_{2g} (M) at 378 cm^{-1}.[113, 232, 274] The frequency around 420 cm^{-1} is attributed to a two phonon process involving a successive emission of a dispersive longitudinal quasi-acoustic (QA) phonon and a dispersionless transverse optical (TO) phonon along the c-axis.[275] The broad feature centered at 450 cm^{-1} is a convolution of three phonon vibrations. The mode around 440 cm^{-1} is attributed to E_{2g} (Γ) + A_{1g} (Γ).[232] Whereas, the frequency mode around 450 cm^{-1} involves two phonons of the longitudinal acoustic branch with opposite momenta at the M point of BZ; hence denoted by 2 LA (M).[276] The third mode around 466 cm^{-1} is assigned to the combined phonon of E_{1g} (Γ) + XA (M)[272] or infrared active A_{2u} mode.[277]

A notable observation about the fitting is the absence of the A_{1g} (M) mode in the valley. During fitting only peak intensities above the noise level are considered. Additionally, if the absence of any of the mode does not affect the fit convolution, then that particular peak is neglected in the fitting. In this regard, A_{1g} (M) is avoided in the vicinity of A_{1g} (Γ). This is probably because the enhancement in the valley is rather weak. Therefore, it is not possible to resolve the mode. But the

scenario changes in case of the enhanced spots, where both out-of-plane peaks are fitted. The fitted peak positions of both first-order Raman modes are displayed in Figure 5.13a. The averaged frequency shift of the E_{2g} (Γ) mode at the corners of the triangles with respect to the valley is measured to be (2.6 ± 0.7) cm^{-1}; equivalent to 0.9 % strain in the material.[71] The averaged frequency shift observed for A_{1g} (Γ) is 0.2 cm^{-1} and is within the error limit of the fitting. Therefore monitoring strain in MoS_2 using A_{1g} (Γ) mode was avoided in this study. As reported by Lloyd *et al.*,[71] the strain *vs.* A_{1g} (Γ) peak shift rate is -0.7 cm^{-1}/% for trilayer MoS_2, which is significantly less sensitive to the applied strain compared to in-plane E_{2g} (Γ) mode (-3 cm^{-1}/% for trilayer). Moreover, the out-of-plane A_{1g} (Γ) mode is more sensitive to doping *via* electron-phonon coupling (EPC) due to its phonon symmetry;[278] by contrast, the in-plane E_{2g} (Γ) shows low sensitivity to EPC due to doping. In this case, the MoS_2 film is deposited on gold nanotriangles and probed by a gold tip during TERS. It is known that both Raman and PL emission in MoS_2 are influenced by the choice of the substrate. Buscema *et al.*[279] showed that both the Raman mode A_{1g} (Γ) and the PL emission of MoS_2 on gold are blue shifted compared to an insulating substrate and related the effect to direct charge transfer from MoS_2 to gold. Therefore, it is possible that strain and doping effects partially cancel each other out in the frequency shift of A_{1g} (Γ) mode. The red shifting and the higher sensitivity to the biaxial tensile strain of the in-plane E_{2g} mode can be explained by the phonon mechanism of this peak. E_{2g} mode involves longitudinal motion of Mo and S atoms in opposite directions in the basal plane. With increasing strain, in-plane lattice constants are increased. As a consequence, the long-range coulomb interaction between Mo atoms decreases and thus the E_{2g} mode softens with increasing strain. Figure 5.13b shows the fitted position of the Raman mode around 465 cm^{-1}. This particular mode is important for the investigation discussed in the next chapter. The mode is shifted by 1 cm^{-1} under 0.9 % of biaxial strain.

The next task of this investigation is to study the strain distribution in the MoS_2 film. To accomplish this task, a second-order derivative (SOD) image is prepared from the AFM topography simultaneously obtained during TERS imaging (Figure 5.14). A freeware image processing software, gwyddion, [280] is used to obtain the SOD image by taking the second derivative along the 2D plane of the topography with respect to the height. Therefore, the SOD image corresponds to the local curvatures, *i.e.* the bending of the MoS_2 film. The brightest spots are representing the highest curvature and thus largest strain in the film. Figure 5.15a shows the averaged spectra taken from the circular spots shown in SOD image in Figure 5.14a. As can be seen, there is a red shift of the E_{2g} mode with respect to the valley that suggests larger strain on these bright spots. In order to quantify the strain, the spectra were deconvoluted using the same method as described above. The fitted spectra are presented in the Figure 5.15b. The deconvolution shows nice fitting of the as measured spectra. The fitted frequency positions of the two first-order modes are presented in Figure 5.15c. As expected, a larger frequency shift is observed in this case. The average frequency shift from area one to eight is (3.8 ± 0.7) cm^{-1}. This is higher than the shift observed on top of gold

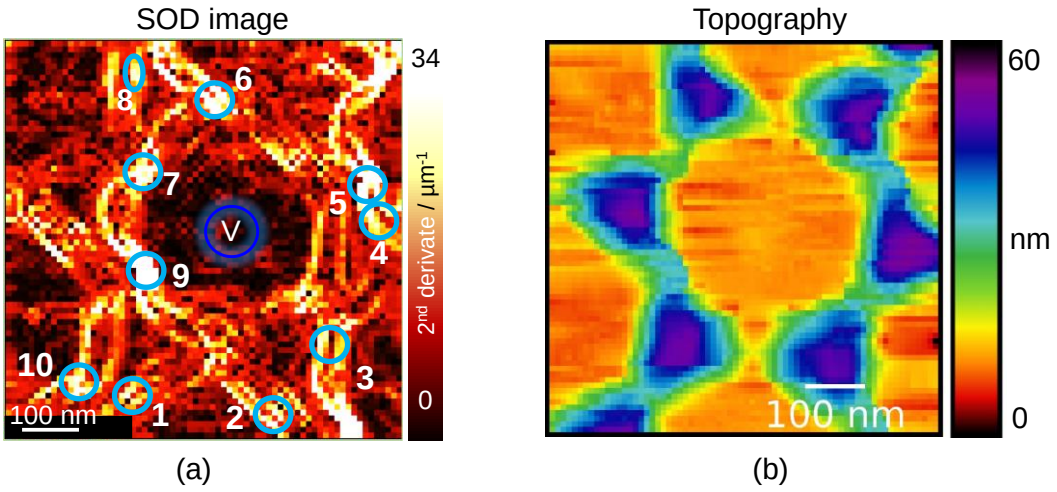

Figure 5.14: Second order derivative image (a) of the AFM topography simultaneously obtained during TERS imaging (b). A freeware image processing software, gwyddion is used to obtain SOD image. The topography image is differentiated along 2D plane with respect to the height using the formula, $SOD = \frac{d^2}{dx^2}, \frac{d^2}{dy^2}(z)$. The circles are the area from where Raman spectra are acquired to quantify strain in MoS_2 film (see Figure 5.15).

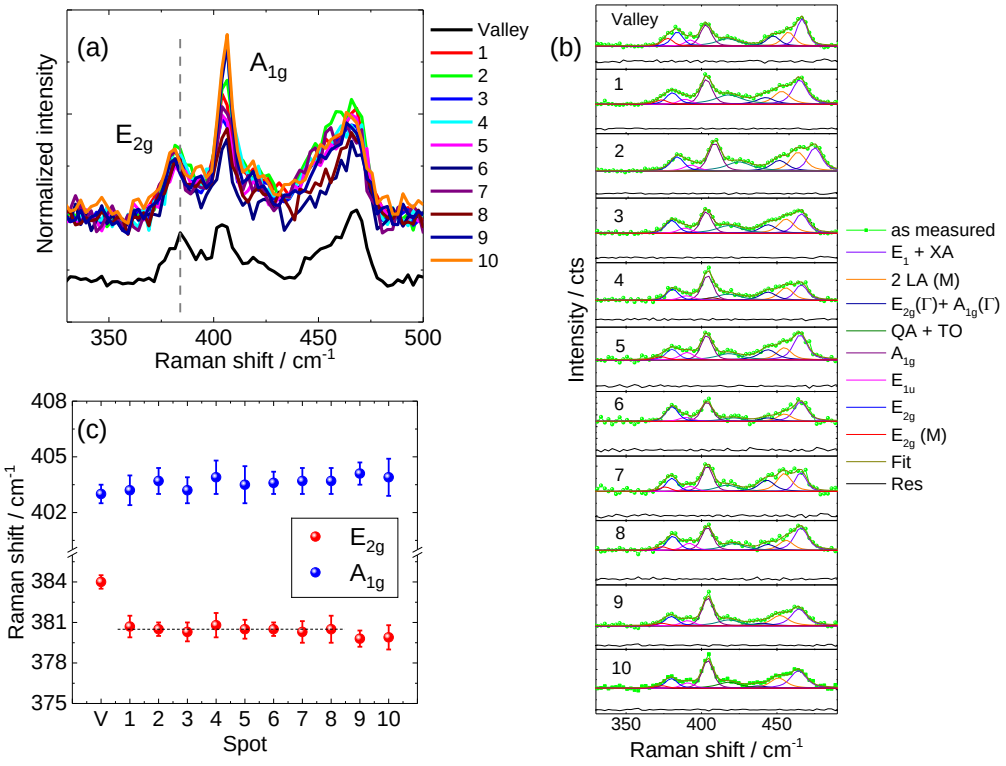

Figure 5.15: The TERS spectra (a) taken from the corresponding circles in the SOD image shown in Figure 5.14. The deconvoluted peaks of the spectra shown in (a) (b). The fitting procedure is the same as mentioned in previous subsection. The fitted peak position of the E_{2g} and A_{1g} mode (c). The black dashed line shows averaged peak position from area one to eight of E_{2g} mode).

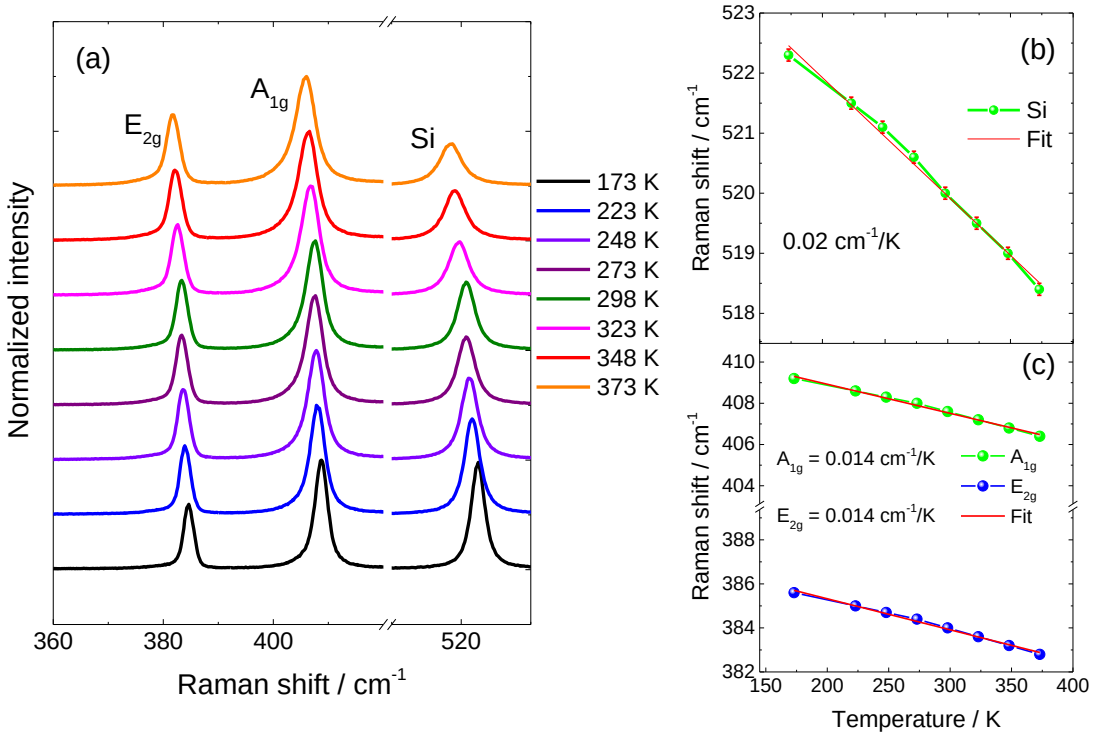

Figure 5.16: Temperature dependent Raman spectra of 3L MoS_2 on a SiO_2/Si substrate (a). As can be seen all modes shift to lower frequencies with increasing temperature. The fitted peak positions and the linear fit of the Si peak with respect to temperature (b). The fitted peak positions of MoS_2 peaks and the fitting with respect to temperature (c). A Voigt function is used for the fitting with a spectral resolution of 1 cm^{-1}.

triangles. The highest frequency shift is observed in case of spots 9 and 10. These two spots are brighter than others which implies a larger degree of curvature. On these two spots the frequency shift is (4.2 ± 0.8) cm^{-1} that is equivalent to 1.4 % strain in the film.

5.7: Influence of local heating in TERS spectra

One of the key parameters of a TERS measurement is to quantify the local heating effect which would cause an additional shift in the Raman spectra. Upon excitation, metal nanocrystals (NC) generate high energetic electrons. The oscillations of these electrons are called plasmons. These carriers are often termed as 'hot' electrons since their energy is larger than the thermal activation energy at room temperature. The hot electrons are confined in a small region of space in NCs due to the geometry of the system (also known as hot spots) and enhance the electric field strongly around it. The plasmonic relaxation is a non-radiative process and thus generates heat. Therefore,

these hot carriers stimulate heat generation in the hot spots leading to local heating. Hence, it is very much possible that the probed material undergoes local heating effects. The local temperature in a TERS experiment can rise up to 100 °C[281-282] even though theoretical simulations predicted as much as 300 °C.[283] In order to determine any local heating effect in this investigation, additional experiments were carried out to determine the temperature coefficient of MoS_2. For this purpose, a 3L-MoS_2 was prepared on a SiO_2 (280 nm) /Si substrate. Raman spectra of this sample were then acquired over a range of temperatures from 173 K to 373 K with a step size of 25 K. A THMS600 microscope stage from Linkam Scientific (operating range of -196 °C to 600 °C with an accuracy of 0.01 °C) was used for the temperature variation. The whole experiment was performed in nitrogen atmosphere. A LabRam HR 800 spectrometer was used for the experiment. The Raman spectra were acquired using the 514.7 nm excitation line and the scattered signals were dispersed onto a Symphony II CCD detector by a 2400 l/mm grating. The laser power was 940 μW determined under the 50x LWD objective. The measurement was performed starting from the lowest temperature and gradually increased to the highest point. During each incremental step, the waiting time was 10 minutes in order to stabilize the temperature. The measured Raman spectra of the sample at different temperatures are presented in Figure 5.16a. Parallel to the Raman modes of MoS_2, the TO phonon of Si was also recorded for calibration purposes. The frequency difference between the two modes of MoS_2 at room temperature was determined to be 24 cm^{-1}; an agreement with the presence of 3L as discussed above. As can been seen all the modes are softened as the temperature rises from 173 K to 373 K. Voigt functions were used to fit all the spectra using the spectral resolution of 1 cm^{-1}. The FWHM of the Si peak (Lorentzian peak) at room temperature is determined to be 2.6 cm^{-1}; in very good agreement with the result by Cardona *et al.* [284] Figure 5.16b shows the fitted peak position of Si with respect to temperature. The linear fit gives a slope of (0.02 ± 0.001) cm^{-1}/K. The temperature coefficient of the Si peak also agrees nicely with literature.[285] Figure 5.16c displays the fitted peak positions of MoS_2 and the linear fit of them. The slope of both fits gives an equal value of (0.014 ± 0.0001) cm^{-1}/K. Compared to the literature, in few layers MoS_2 it was rigorously established by several independent groups that the temperature coefficients for both modes E_{2g} and A_{1g} are in the same range (in the order of 1.5 x 10^{-2} cm^{-1}/ K). [286-290] This is due to the fact that TMDCs layers are held together by a weak van der Waals interaction. Therefore, with increasing temperature, interlayer coupling is affected in the same way to the lattice expansion. Thus, the temperature coefficients of the both the in-plane E_{2g} mode and the out-of-plane A_{1g} mode are in the same range.

If one now looks closely on the TERS image in Figure 5.12a, it is evident that the hot spots are created at the three corners of the gold NTs resulting in the strongest TERS intensities. Therefore, most local heating should be generated on those corners. If there is any local heating effect, then this must produce similar peak shifts for both modes. Figure 5.13a shows relatively large frequency shifts for the E_{2g} mode (2.6 cm^{-1}) but only negligible changes (within the error bar) of the A_{1g} mode

(0.2 cm^{-1}). Therefore, the thermal contribution to the frequency shifts should be negligible. Moreover, the shifts measured in the higher curvature areas of Figure 5.15 are valid points to discard the local heating effects as a significant contributor since hot electron induced thermal influence on those areas should be much less. Thus, one can conclude that local heating has a negligible impact on these tip-enhanced Raman spectroscopy results. Hence, the observed phenomenon is mainly dominated by the local strain which explains the selective shift of the E_{2g} mode. A similar conclusion can be made for the SOD image in Figure 5.14 and 5.15 where the frequency changes of E_{2g} mode are even larger than that for the A_{1g} mode. Therefore, it can be justified that the peak shifts are solely due to strain effects.

5.8: Summary

In summary, thanks to the remarkable spatial resolution of TERS, it is possible to map heterogeneous strain in MoS_2 mechanically deposited on a nanostructured Au substrate, with peak values reaching up to 1.4 %. It is found that the regions of maximum local strain correspond to the regions of maximum topographic curvature extracted from AFM measurements. These results imply that in optoelectronic device applications, beyond the energy level alignment in MoS_2/metal contacts, also the strain-induced effects induced by a patterned substrate must be taken into account, which will significantly impact the local properties of this promising 2D material.

Chapter 6

TERS study of local heterogeneities of MoS_2: Strain and doping

Most of the work discussed in this chapter is published in ***Nanoscale***, 10, 2018, 2755

This is the continuation of the previous chapter. With the help of the knowledge gathered in the previous chapter, a local doping effect in monolayer MoS_2 is decoupled from the biaxial strain. Instead of gold nanotriangles, gold nanocylinders of similar height on silicon are used as the plasmonic substrate. The combination of gold nanocylinders – gold tip gives a strong enhancement of the electric field in the hot spots using 785 nm excitation. This phenomenon induces unprecedented hot electron doping in 1L-MoS_2 leading to a structural change.

6.1: Introduction and motivation

The ability of noble metal nanostructures to manipulate the light at the nanoscale empowers them with high potential of applications in a wide range of disciplines (summarized in these reviews).[291-292] The light – matter interaction is performed in the form of collective oscillation of charge carriers in a confined system known as localized surface plasmon resonance (LSPR) in metal nanostructures. Once excited with a suitable laser, LSPR confines the electric field in a deep subwavelength scale leading to unprecedented enhancement of the local electric field. Therefore, plasmonic structures are used extensively in the field of amplification of fluorescence, infrared absorption, and Raman scattering. [293-294] As discussed in the previous chapter, the principle of TERS is based on LSPR of a sharp metallic tip which controls both the spatial resolution and the sensitivity of the measurement. However, while performing TERS by creating hot spots between tip and the sample substrate, both the sensitivity and spatial resolution can be drastically improved. Another parameter which also controls the sensitivity and spatial resolution in TERS is the molecular response to the confined field.[258] Therefore, this fairly new technique mainly focused on organic molecules [191, 295-298] which have high TERS cross-sections due to their superior absorption coefficient. An enhancement factor (EF) exceeding 10^7 was achieved in TERS experiments on certain sorts of organic compounds[299-301]. Also a lateral resolution below 2 nm

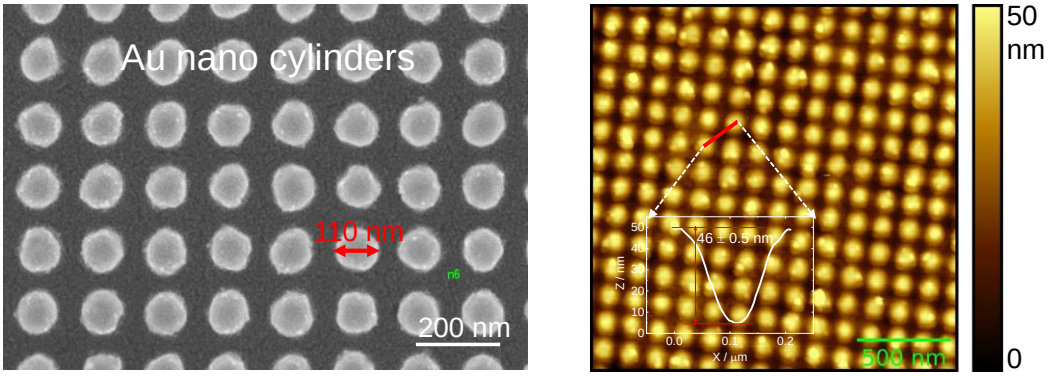

Figure 6.1: SEM image of the gold nanocylinders (a). The diameter of the cylinders is (110 ± 10) nm. The pitch is 150 nm. AFM topography of the nanocylinders (b). The height profile of the gold cylinder along the cross section marked by a red line is shown in the inset of the topography. The height of the cylinders is 50 nm approximately.

using ambient TERS[301-303] was demonstrated. However, also inorganic materials such as CdS,[304] Si [247, 305-308], GaN, [309] GeSi [310-311] GaAs, [312] Fe_2O_3, [313] and CdSe [314] were studied using TERS in the past few years.

Very recently, TMDCs also became the subject of tip enhanced optical spectroscopy.[315] Due to the strong confinement in monolayer thickness, structural inhomogeneities such as defects, doping, and strain can greatly influence their photoresponse as revealed by TERS.[249-250, 316-318] However, the TERS sensitivity is one of the major issues that may hinder the in-depth study of these materials. In this chapter, an approach to improve both the sensitivity and the spatial resolution of the TERS experiment are discussed. An array of gold nanocylinders on silicon was used as the substrate. The TERS tips were fabricated by in-house facilities. Coupling between a gold nanocylinder and the gold tip gives an unprecedented Raman enhancement from 1L-MoS_2 with a very high spatial resolution in TERS imaging.

Another important aspect of this study is the investigation of plasmonic hot electron induced structural phase transition in MoS_2. Due to the very unique physical properties, MoS_2 monolayers attracted intense interest in the field of optoelectronics.[135] However, the light matter interaction cross section is small due to its atomic layer thickness. Therefore, coupling with plasmonic antennas is a popular approach to enhance the photoresponse.[319-320] It is, however, shown in this investigation that plasmonic coupling not only increases the light sensitivity but also modifies the

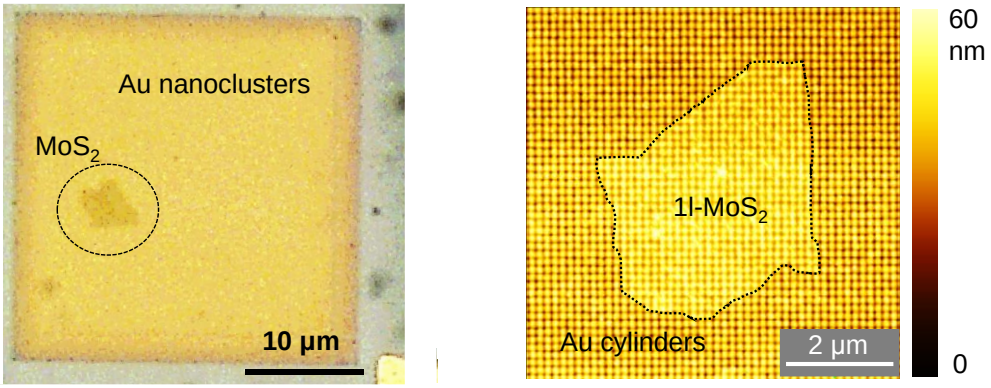

Figure 6.2: Optical image (a) and AFM topography (b) of the sample after transfer of a 1L-MoS_2 flake onto the plasmonic substrate (a). 1L-MoS_2 is marked by a circle in the optical image and a black dotted line is made along the border of the flake as the guide for the eye.

phase in MoS_2. Due to the strong interaction between the excitation wavelength and the effective LSPR in TERS, the monolayer MoS_2 undergoes a heavy plasmonic hot electron doping which induces a structural phase transition from semiconducting to metallic MoS_2. Owing to the very high spatial resolution in the TERS measurement, it is possible to locate those doping sites.

6.2: Experimental details

Preparation of plasmonic substrate: Uniform periodic gold nanocylinder arrays of a dimension of 10 x 10 µm² and a period of 150 nm were fabricated on (001) oriented silicon substrates by a direct write electron beam lithography process. The electron resist (polymethyl methacrylate 950 K) deposited on the silicon substrate was structured with an electron beam (20 kV, Raith-150, Germany). The patterned resist was then covered by a 5 nm thick film of titanium and 50 nm thick film of gold. The remaining resist was removed by a lift-off process in dimethylformamide to obtain isolated gold nanocylinders. Details of the preparation and characterization of the plasmonic substrate can be found in Sheremet *et al.* [314] The size, shape, and ordering of gold nanocylinders were determined by scanning electron microscopy (SEM) using the same Raith-150 system at an acceleration voltage of 10 kV, 30 µm aperture, and 6 mm working distance and atomic force microscopy (AFM) in tapping mode AFM. Commercially available Si tips (NSG10 series) from TipNano were used for the AFM characterization. The nanocylinders have a diameter of (110 ±10) nm and the height of 50 nm approximately. Figure 6.1 shows typical SEM

The plasmonic substrates were prepared in collaboration with Prof. Milekhin of Novosibrisk State University, Russia

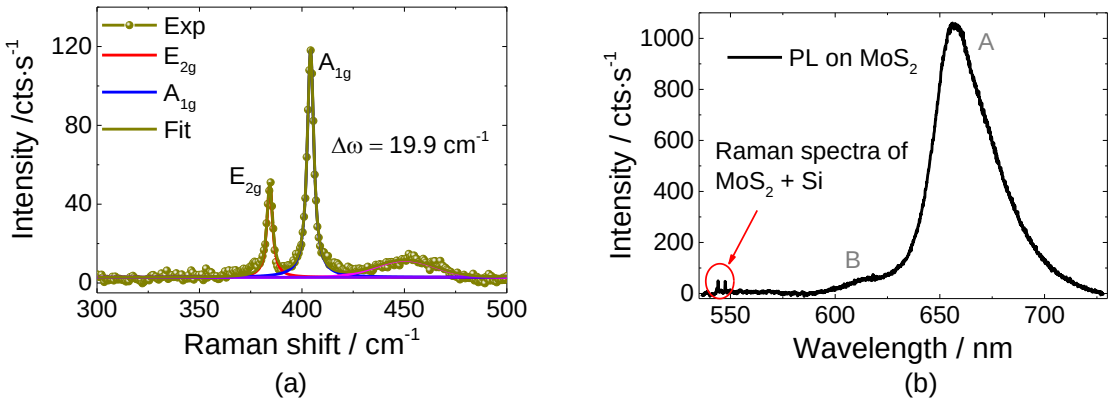

Figure 6.3: Raman spectrum of the 1L-MoS_2 sample (a). The frequency difference between the two modes of MoS_2 is determined to be 19.9 cm^{-1} and confirms the presence of 1L-MoS_2. Complementary PL spectra of the sample (b). The high PL yield is the confirmation of a direct band gap and thus also confirms presence of 1L-MoS_2. Both spectra are taken using 532 nm excitation of 105 µW power. For the Raman spectra a 2400 l/mm grating is used to disperse the Raman signal on an EMCCD.

and AFM topography images of the plasmonic structure. The height profile is shown in the inset of the topography.

Sample preparation: A monolayer MoS_2 is transferred on to the plasmonic substrate following the procedure described in section 5.3, Figure 5.5. Figure 6.2 displays the optical and AFM topography images of the monolayer MoS_2 transferred onto the plasmonic substrate.

Determination of layer thickness: Raman spectroscopy is a powerful technique to determine the layer thickness of graphene and TMDC materials. It was already discussed in the previous chapter that the Raman spectra of MoS_2 are strongly influenced by the variation of layer thickness. Therefore, by monitoring the frequency difference of the two first order Raman modes, (E_{2g} and A_{1g}) one can exactly determine the layer thickness. Figure 6.3a presents the Raman spectrum of the 1L-MoS_2 sample. The spectrum was acquired using a Xplora plus Raman microscope from HORIBA. The sample was illuminated by 532 nm excitation of 105 µW laser power measured at the sample surface focused by a 100x, 0.9 NA objective. The scattered Raman signals were dispersed onto an EMCCD by a 2400 l/mm grating giving a spectral resolution of 1 cm^{-1}. The two Raman modes of MoS_2 were fitted by Voigt functions using the spectral resolution. The frequency difference from the fitted positions is determined to be 19.9 cm^{-1} and confirms the presence of monolayer MoS_2.[321] Since MoS_2 has the very unique electronic property of changing the nature of the bandgap from indirect to direct in monolayer, a complementary photoluminescence (PL)

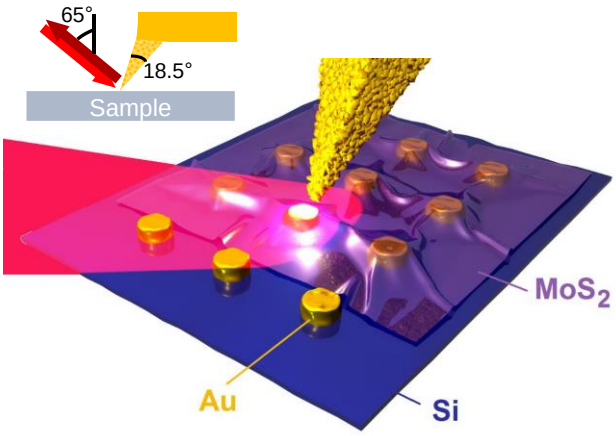

Figure 6.4: Schematic of the TERS set up for this investigation. Gold nanocylinders on a silicon is used as the substrate. Gold coated silicon cantilevers are used as TERS tips. Inset is the illumination/collection geometry with respect to the tip axis.

measurement was also performed to confirm the monolayer thickness. The sample was excited by the 532 nm laser of 105 μW power at the sample surface. Figure 6.3b shows the PL spectra of the sample. Monolayer MoS_2 is a direct band gap semiconductor with an optical band gap around 1.9 eV. In this spectrum the PL peak is centered around 660 nm equivalent to 1.87 eV. The fundamental emission peak is called *A* peak in MoS_2. Additionally, another peak called *B* peak is also observed originating from spin-orbit coupling and lies around 120 meV deeper than A peak.[46] The high PL yield confirms the nature of the direct bandgap, thus monolayer MoS_2.

TERS measurement: Measurements were performed on a NanoRaman Platform (HORIBA Scientific/former AIST-NT) consisting of an atomic force microscope (SmartSPM) combined with a Raman spectrometer (XploRA) in side-illumination geometry. The schematic of the TERS experiment is shown in Figure 6.4. Excitation and collection are realized through a long working distance objective (100×, 0.7 NA) in the side illumination geometry. The angle of the incident and collected light is 65°.The laser focus is, therefore, non-symmetric and enlarges the illuminated area up to approximately 1.7 μm². The incident light is *p*-polarized while non-polarized scattered light is detected. As discussed in the previous chapter, this geometry is favourable for TERS experiments because it provides stronger Raman scattering for vibrational modes polarized perpendicular to the surface [322] and oriented parallel with the tip axis. [323] TERS tips were prepared by in-house facilities and are discussed in section 6.3.

An excitation wavelength of 785 nm was used for TERS acquisition with an incident laser power of approximately 3 mW at the sample surface. The scattered light was detected by an electron

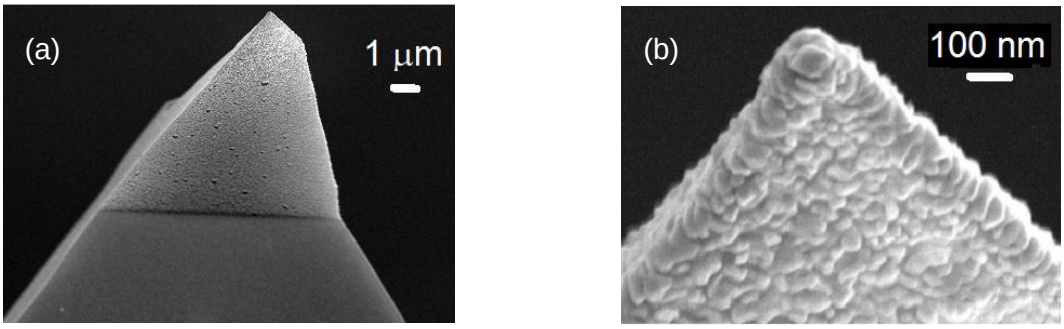

Figure 6.5: A typical SEM image of a TERS tip prepared by evaporating Au on a silicon cantilever (a). A magnified SEM image of a TERS tip revealing the formation of Au nanoclusters at and around the tip (b).

multiplying charge couple device (EMCCD) after dispersion using a 600 l/mm grating. The acquisition time for each TERS spectrum is 0.4 s or 0.5 s. In addition to the near field TERS mapping, the far field Raman signals were taken simultaneously using the same experimental parameters. This experimental condition was achieved via the "Dual spec" mode, a software modification of the instrument. In this mode, TERS spectra are acquired in the same way as described in the previous chapter. However, in each measurement point, immediately after acquiring the TERS spectra, the sample is brought down by 70 nm to acquire the far field Raman signal at that point. It was already discussed in the previous chapter that the evanescent field created at the tip apex due to the LSPR is exponentially decaying as the distance increases between the tip apex and the sample. Therefore, at 70 nm tip-sample distance, the near field contribution is negligible. On the other hand, the laser spot diameter is 1 μm approximately, meaning the sample is still in the focus center of it. Hence, the far field signal attenuation is minimal.

6.3: Preparation of TERS tips

One of the major issues of conducting TERS experiment, is the price of commercially available TERS tips. Due to their high cost, it is desirable to look for alternative options to prepare low cost highly reliable TERS tips. In this investigation, the TERS tips were prepared using in-house facilities. At first, commercially available Si cantilevers with a special tip orientation were bought from TipsNano (probe type: VIT_P series). The tips are oriented at an angle of 26° from the cantilever edge and are therefore suitable for laser alignment at the tip apex in the side illumination geometry. The average radius of the tip is 10 nm. The probes were coated with a gold film using a controlled evaporation in a high vacuum chamber. Gold deposition was performed by thermal

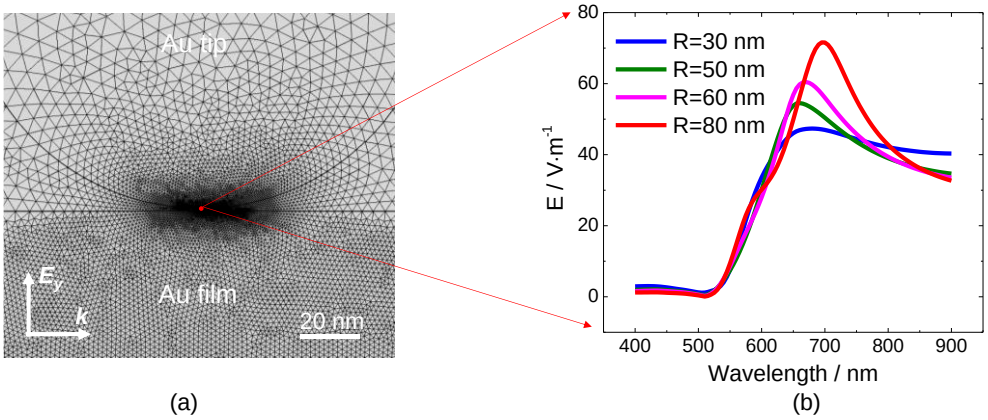

Figure 6.6: Mesh image of one the tip-sample systems used in the calculation (a). The red dot is the position 0.1 nm below the tip apex from where E_{loc} is calculated at each tip radius. The spectral response of E_{loc} at different tip radii (b). With increasing tip size, the LSPR shifts to higher wavelength. Additionally, the amplitude of the local electric field at LSPR also increases.

evaporation of gold from a boron nitride crucible. The base pressure in the vacuum chamber was kept at 10^{-6} mbar. The deposition rate was maintained at 10nm/min controlled by a quartz microbalance. The nominal thickness of the gold coverage was between 150 nm and 350 nm. No noticeable difference in TERS performance of the tips covered with different thicknesses of Au layers was found. Before Au evaporation, 20 nm of Ti was deposited on the Si tips. During the deposition processes the Si tips were heated up to 70 °C.

Figure 6.5 displays the SEM images of the tips after gold deposition. Evaporation of gold commonly results in randomly distributed nanoclusters around the tip as shown in the magnified image in Figure 6.5b. The average size of the nanoclusters at the apex varies from 70 – 90 nm. The localized surface plasmon of these nanoclusters at and around the tip apex therefore acts as the nano-optical source for TERS signals.[324]

Before performing TERS with these tips, it is essential to know how the tip size would influence the measurement. Especially the general understanding is that the local field enhancement has opposite trend to the size of the tip radius. Therefore, the spectral response of the local field distribution around the tip apex is calculated for various tip radii using the COMSOL simulation tool. The simulation was performed in the gap mode TERS configuration with a tip-sample gap of 1 nm. Figure 6.6a presents the mesh image of the tip-sample system used for the simulation. The meshing parameters are the same as discussed in the previous chapter. Due to the high meshing resolution in the narrow regime between the tip and the sample, the simulation can reliably

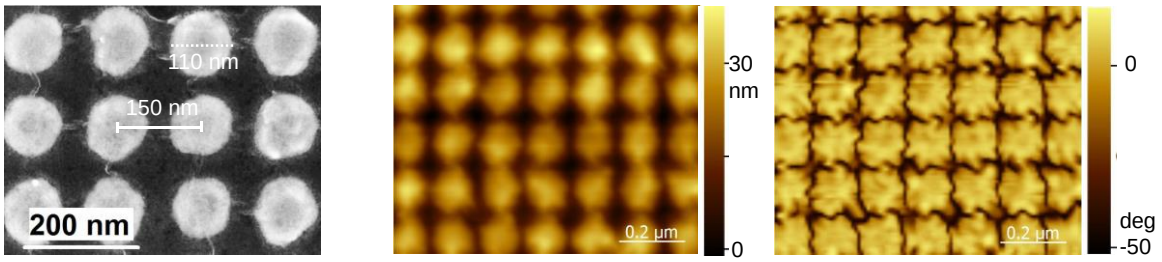

(a) (b) (c)

Figure 6.7: High resolution representative SEM images of the Au nanocluster array with monolayer MoS_2 stamped on the sample surface (a). The pitch is 150 nm (solid line) and the cluster diameter is 110 nm shown by a dashed line. Typical AFM topography (b) and phase images (c) of the same sample. The surface heterogeneities are clearer in the phase image than topography.

calculate the electric field in the gap. The spectral response of the electric field with respect to different tip radii is shown in Figure 6.6b. The electric field amplitude is taken 0.1 nm away from the tip apex towards the sample as shown by a red dot in the mesh image. Interestingly, the amplitude of the local electric field at resonance condition increases with increasing radius of the tip, even though the spectral position of the LSPR shifts towards the red region. The phenomena can be explained by surface scattering, and volume radiation damping. [325-327] In the case of a sharp metallic tip, the lightening rod effect dominates the local field enhancement (independent of LSPR).[328] With the increase of the tip radius, this effect weakens and both surface scattering and radiation damping start to increase. However, up to a certain tip radius surface scattering is stronger than radiation damping. Therefore, the local field enhances with increasing tip radius at LSPR. Additionally, due to dimensionality effects, the spectral position moves to larger wavelengths. In the case of a gold coated silicon tip and gold substrate system, Meng *et al.* [327] reported that the local field can continue to increase up to 80 nm of tip radius. A similar trend is also observed in this investigation. However, the local field enhancement with increasing tip radius comes with the sacrifice of spatial resolution as discussed in section 5.2 (equation 5.6). Thus, a compromise needs to be made between the enhancement and spatial resolution. In this investigation, therefore, home built TERS tips are used with an excitation wavelength of 785 nm to get the benefit of higher electric field enhancement as suggested by the simulation results. In total five tips were produced using the same preparation techniques mentioned above. All the tips showed similar TERS enhancement behaviour on the 1L-MoS_2/plasmonic heterostructure used in this investigation.

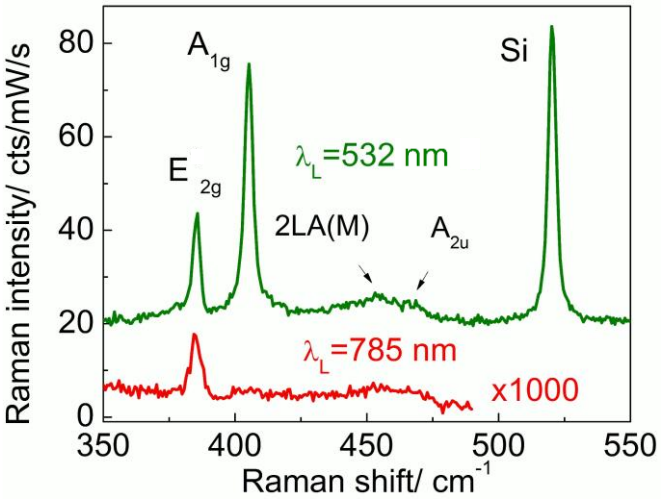

Figure 6.8: Micro-Raman spectra of monolayer MoS_2. The green spectra was acquired on the heterostructure excited by 532 nm and red spectra was acquired on Au substrate excited by 785 nm (see text). The Raman spectrum taken at 785 nm is multiplied 1000 times for better presentation.

6.4: Morphology study of the heterostructure

Fig. 6.7a presents a high-resolution SEM image of the MoS_2 monolayer deposited on an Au nanocylinder array by the deterministic transfer method. The period and the size of the Au nanocylinder pitch and diameters can be easily determined due to the transparency of the MoS_2 monolayer for the electron beam and amount to 150 nm and (110±10) nm, respectively. The SEM image reveals bright strands between the Au nanocylinders originated from MoS_2 monolayer wrinkles. The AFM topography and phase images of the MoS_2 monolayer are presented in Figure 6.7b-c, respectively. As one can see from the topography image, MoS_2 covers the Au nanoclusters array, precisely replicating the array morphology (in agreement with the SEM image). However, MoS_2 wrapped around Au nanocylinders causes uncertainties in size and shape of this cylinders and reduces the height contrast in the topography image to 35 nm in comparison with the value of 50 nm for bare Au nanocylinders. The phase image being very sensitive to mechanical properties of materials via adhesive interaction between tip and sample reveals the surface gradient representing the folding of MoS_2 monolayer in the areas between Au nanocylinders.

6.5: Micro Raman study of the heterostructure

The excitation wavelength of 785 nm (1.58 eV) used in TERS experiments is below the optical bandgap of monolayer MoS_2. Raman scattering from a monolayer MoS_2 under below bandgap

excitation can be significantly different than that for above bandgap excitation. Therefore, before performing TERS on such heterostructure, it is important to study the effect of excitation wavelength on the Raman spectra of MoS_2. The excitation energy dependent micro-Raman spectra of the heterostructure are presented in Figure 6.8. The strong peak around 520 cm^{-1} at 532 nm excitation is due to Raman scattering by the optical phonon in the Si substrate. The two other most pronounced modes in the Raman spectra are from monolayer MoS_2 and the origin of them was discussed in the previous chapter. The strong Raman band at 405.2 cm^{-1} refers to the out-of-plane A_{1g} mode and the weaker peak at 385.3 cm^{-1} is assigned to the in-plane E_{2g} mode. In addition to these well-known optical phonon modes, there are two weak second-order bands appearing near 455 cm^{-1} and 465 cm^{-1} originating due to resonance condition (above band gap excitation). The first second-order Raman process involves the longitudinal acoustic phonons at the *M* point of the Brillouin zone denoted by $2LA(M)$[277, 329] . The other mode at 465 cm^{-1} is a infrared active A_{2u} mode [277] or combinational $E_{1g}(\Gamma) + XA$ mode.[272]

When excited with 785 nm wavelength (below band gap excitation) no micro-Raman signals were observed from a monolayer MoS_2 either on Si substrate or gold nanocylinders. However, the situation changed when a gold substrate is used as shown in Figure 6.8. The E_{2g} mode can be seen in the Raman spectrum of 1L-MoS_2 while the intensity of the A_{1g} mode is significantly suppressed. Additionally, the intensity of the E_{2g} at this excitation is much weaker (by a factor of $2{\cdot}10^3$) compared to the intensity measured at the excitation wavelength of 532 nm. This can be understood by the fact that the 785 nm (1.58 eV) wavelength is smaller than the band gap of monolayer MoS_2 (1.87 eV) in accordance with the results reported in literature.[330] The reason of the supressed intensity of the A_{1g} mode can be related to the origin of this band. Yang *et al.*[331] reported that the A_{1g} mode can only be excited via electron-phonon exchange interplay. In the case of below band gap excitation such exchange interplay is avoided; therefore, A_{1g} is supressed.

6.6: TERS imaging of the heterostructure

A TERS spectrum of a monolayer MoS_2 on the heterostructure using 785 nm excitation is presented in Figure 6.9a. For comparison the magnified micro-Raman spectra using the same excitation laser line shown in Figure 6.8 is also included. As can be seen the Raman spectrum of a monolayer MoS_2 on the heterostructure changes dramatically in the TERS configuration. The E_{2g} mode, which is prominent in conventional Raman spectra under non-resonant conditions, vanishes in the TERS spectra. Whereas the intensity of the A_{1g} mode is strongly enhanced. This remarkable enhancement of the A_{1g} mode can be explained by 1) selection rules due to experimental configuration and 2) strong plasmonic coupling between MoS_2 and Au nanocylinders. In this TERS experiment, the polarization of the incident light is directed along the Au tip and predominantly perpendicular to the sample surface. Therefore, it only enhances out-of-plane modes (including the A_{1g} mode)

Raman tensors of both E_{2g} and A_{1g} modes of MoS_2 are discussed in Appendix A-3 to explain TERS selection rules.

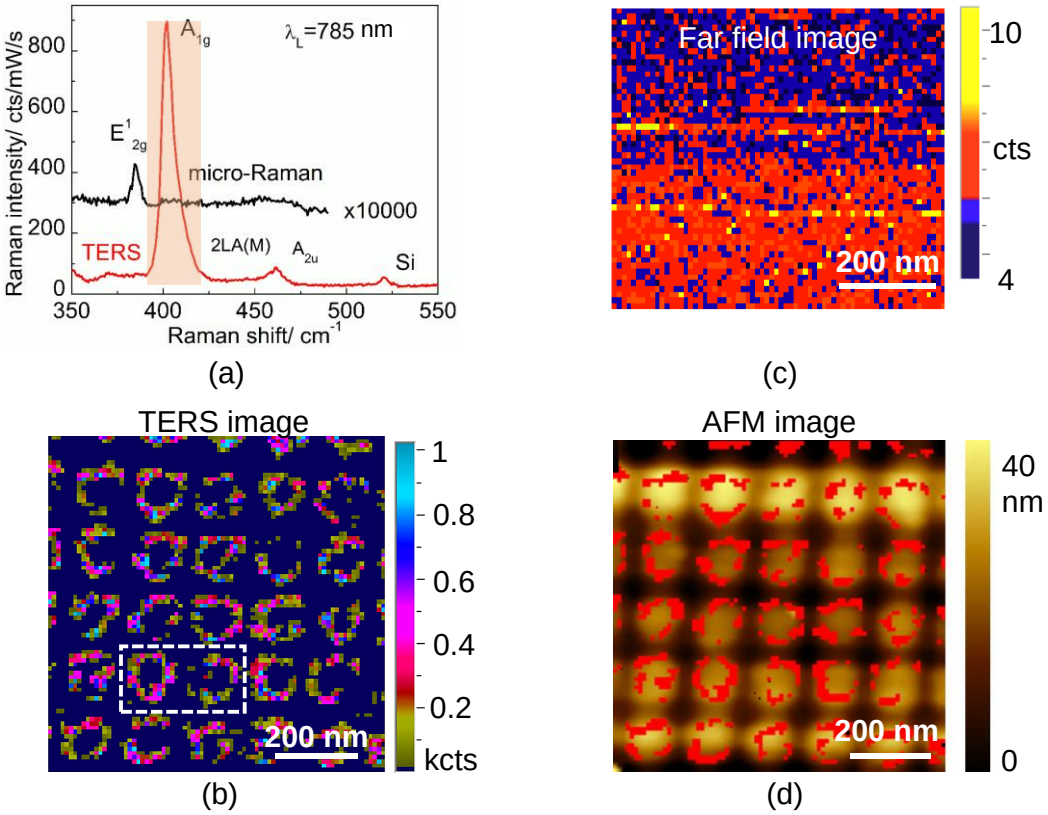

Figure 6.9: A representative TERS spectrum of 1L-MoS_2 on Au nanocluster array using 785 nm excitation and homemade Au coated silicon tips (a). For comparison 10000 times magnified micro-Raman spectrum of 1L-MoS_2 on flat Au surface using the same excitation is included. A spatial map of the Raman intensity of the A_{1g} mode (b) and far field Raman map of the same area taken simultaneously (c). Both TERS and far field maps are acquired within the area marked by a shaded rectangular box around A_{1g} mode in (a). The corresponding AFM topography of the TERS map (d). The topography is superimposed by the maximal intensity map shown in (b). The area marked by white dashed line in TERS image is used for higher resolution mapping shown in Figure 6.12.

according to the TERS selection rules.[323] On the other hand, it was already demonstrated by several groups that monolayer MoS_2 has a strong coupling to plasmonic nanostructures via hot electrons injection. [67, 209, 332-333] Due to the suitable barrier height at the Au/MoS_2 interface, plasmonic hot electrons can easily be injected into the conduction band of MoS_2.[67] This injection of electrons leads to the modification of photoluminescence, Raman spectra, and reversible structural change. However, hot electron doping is the most probable case which leads to strong electron-phonon coupling. Therefore, the A_{1g} mode can be excited via such exchange correlation. A strong

enhancement of the A_{1g} mode by a factor of 4x10^5 is obtained from the comparison of the mode intensity derived from TERS and micro-Raman spectra.

Additionally, another mode is enhanced at 461.7 cm^{-1}. The origin of this mode is debatable as different groups assigned this mode to either a combination of $E_{1g}(\Gamma) + XA$ [272]or infrared active A_{2u} mode.[277] However, the appearance of this mode in the TERS configuration indicates that the notation of infrared active A_{2u} mode is more probable. This is due to the fact that the infrared active A_{2u} mode can appear in the TERS spectra via a strong electric field gradient effect which leads to the activation of forbidden infrared modes in a material placed near a metal surface. [334-335]

To get detailed information about the heterostructure, a representative TERS image of the A_{1g} mode of the MoS_2 monolayer (shown in Figure 6.9a) is acquired and presented in Figure 6.9b. A far field Raman map is also acquired simultaneously and is shown in Figure 6.9c. The far field map is taken from the same area of the spectral dispersion in Raman spectra of the heterostructure as taken for the TERS map. No MoS_2 mode is observed under far field condition. This is understandable since the 785 nm excitation is below the band gap of 1L-MoS_2 as discussed in the previous section. The corresponding topography image is shown in Figure 6.9d. The spectral acquisition time is 0.4 s with a step size of 10 nm over an area of 0.7 x 0.7 μm^2. Figure 6.9b reveals that the TERS signal forms the pattern of ordered rings. A superposition of the TERS image on the corresponding topography shows that the rings perfectly coincide with the Au nanocylinders. This indicates that the TERS signal predominantly originates from the edges of the Au nanocylinders. The TERS signal from the ring areas is enhanced by a factor of 10^3 compared to the intensity of the TERS background signal which is taken from the area outside of the rings. Obviously, such a strong TERS contrast is due to a strong electromagnetic field localized near the edges of the Au nanocylinders induced by surface gap plasmon modes. The TERS enhancement is proportional to E^4, [336] (here $E = {E_{loc}}/{E_{far}}$) and corresponds to an amplification of the electric field magnitude in the gap between the AFM tip and the Au nanocylinder. The TERS images derived for the MoS_2 monolayer on Au nanocylinders correlate with the ring-like spatial distribution of plasmonic modes in Au nanocylinders calculated numerically[337] and determined using scanning near-field optical microscopy.[338-339]

6.6.1: Determination of spatial resolution:

To achieve an ultimate spatial resolution, an area of 200 nm x 200 nm with strong TERS signals in Figure 6.9b was chosen for high resolution TERS mapping. The step size of the mapping was 2 nm meaning each pixel size of the TERS image in Figure 6.10a is 2 x 2 nm^2. The spectral acquisition time was 0.5 s. The image represents the shape of an opened ring with a maximal TERS intensity

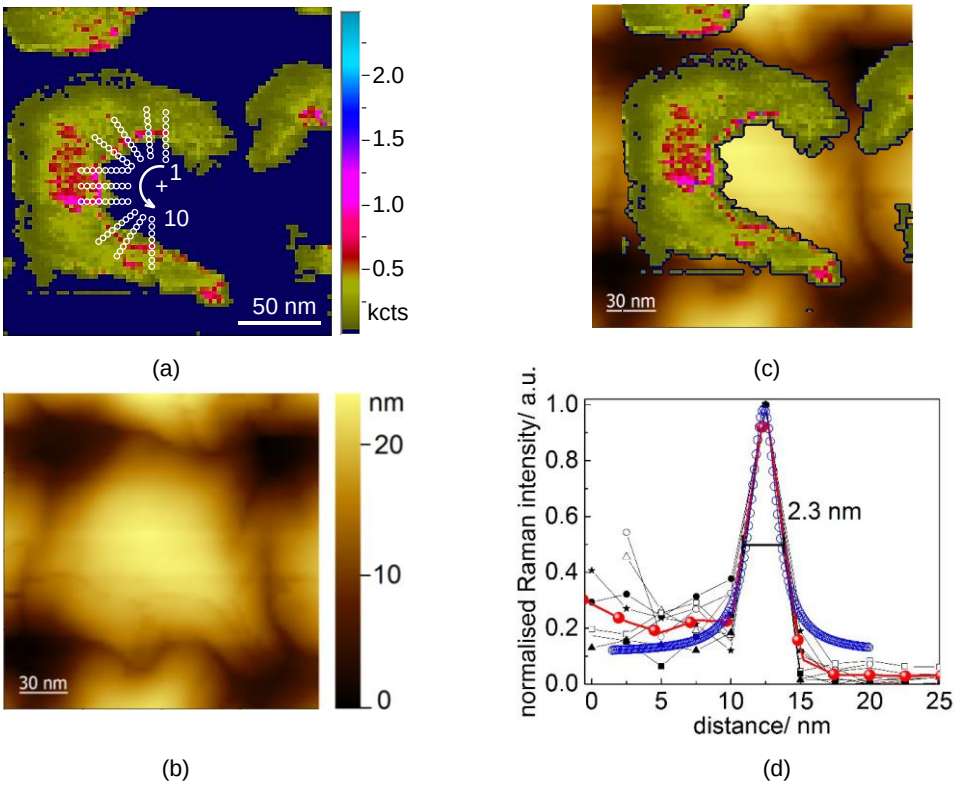

Figure 6.10: High resolution TERS map of the A_{1g} mode of 1L-MoS_2 on Au nanocylinders (a). A step size of 2 nm is used in the imaging. Corresponding AFM topography taken immediately after the TERS imaging (b). For better understanding of the TERS map, intensity image is superimposed on the topography (c). TERS profiles along the radial line of the inner circle (d). The profiles are taken along the lines marked by open circles in (a). The average line profile is shown by red balls joined by a red line and the Gaussian fit is shown by blue balls connected by blue line. The FWHM is determined to be 2.3 nm.

at the internal ring diameter. Deviation of the TERS image from the ring shape is most probably due to the surface topography of the MoS_2 monolayer covering the Au nanocylinder with a non-ideal cylindrical shape. A high-resolution AFM image was taken from the same area immediately after the TERS mapping (Figure 6.10b) to establish this hypothesis. As can be seen in the topography, MoS_2 reveals a deformed shape which deviates from the cylinder like structure. To better understand the effect, the TERS image is superimposed on the topography and presented in Figure 6.10c. The superimposed image reproduces nicely the main features of the TERS map and confirms this assumption. To determine the spatial resolution of the image, ten TERS profiles were taken along the radial line of the internal ring as shown in Figure 6.10a. The TERS profiles and their average are presented in Figure 6.10d. A FWHM of (2.3±0.3) nm is determined from the best

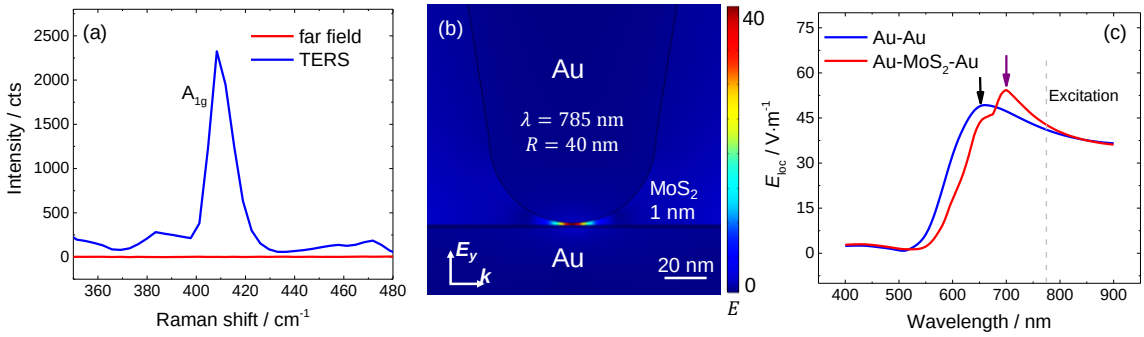

Figure 6.11: Comparison of TERS spectra taken from hot spots shown in Figure 6.10a and far field Raman signal. Calculated local electric field distribution around the tip for Au-1L-MoS_2-Au system at 785 nm excitation (b). The definition of E is given in Figure 5.1. Spectral response of the local field for the same system (c). The local field is taken from 0.1 nm below the tip apex for each wavelength. Black arrow is the position of dipole and violet arrow is the position of absorption edge of MoS_2. For comparison Au-Au system of 40 nm tip radius is included.

Gaussian fit of the averaged TERS profile. This is a very good TERS resolution considering the fact that the tip radius was in the range of 40 nm (cluster size 80 nm). According to equation 5.6, for an Au-Au system, the width of the confined electric field would be 12.7 nm for a tip-sample distance of 1 nm. Since the TERS intensity is approximated by E_{loc}^4 (see equation 5.8), the TERS spatial resolution can be calculated as $2\sqrt[4]{Rd} \approx 5$ nm for a tip-sample distance of 1 nm. This is a very good agreement to the experimentally determined spatial resolution. Note that, the slight deviation between the experiment and simulation can arise from several reasons. In this investigation TERS experiment were performed when the tip makes contact with the substrate. Therefore, the resolution should be higher. Moreover, the SEM image of the Au tip shown in Figure 6.5 reveals that Au forms clusters around the tip apex. Thus, the size and shape of the cluster participating in the TERS imaging may be smaller than the assumed size of 80 nm and can give better resolution.

6.6.2: Determination of enhancement factor:

The maximum TERS intensity of the A_{1g} mode of 1L-MoS_2 on the Au nanocylinder array derived from the TERS image (Fig. 6.10a) reaches a value of 1.6x10^3 cts/mW/s (2.4x10^3 cts per 0.5 s per 3 mW). Both maximum TERS intensity and the far field Raman signals are presented in Figure 6.11. A quantitative estimation of the TERS effect can be performed using the TERS contrast and the TERS enhancement factors defined previously.[298, 340-342] The TERS contrast which determines the quality of TERS images and evaluates the ratio of the local and far-field signals is estimated as the intensity ratio of the Raman signal with tip down (I_{TERS}) and tip up (I_{Raman}).[298] In this

investigation, tip down and up situations are altered by the sample in contact with tip and down by 70 nm, respectively. Thus,

$$Contrast_{TERS} = {}^{I_{TERS}}/_{I_{Raman}} = 1.6 \times 10^3 / 1.3 = 1.2 \times 10^3 \qquad 6.1$$

Now, using the equation 5.10, one can calculate the TERS enhancement factor (EF) as:

$$EF = Contrast_{TERS} \times \frac{A_{focus}}{A_{tip}} = 1.2 \times 10^3 \times \frac{1.7 \times 10^{-12}}{5 \times 10^{-15}} = 4.08 \times 10^5 \qquad 6.2$$

where R =40 nm. However, in this case, the TERS signal originates from the hot spots having a size of the pixel 2 nm approximately, which is much smaller than the tip diameter. Therefore, the TERS enhancement factor induced by a hot spot ($EF_{hot\ spot}$) can be estimated as,

$$EF_{hot\ spot} = Contrast_{\mathrm{TERS}} \times \frac{A_{focus}}{A_{hot\ spot}} = 5.1 \times 10^8 \qquad 6.3$$

This is a giant value of enhancement factor. Interestingly taking into account the thickness of the MoS_2 monolayer (0.7 nm) and the pixel size (2 nm), the scattering volume which induces such a strong TERS signal can be calculated and amounts to a tiny value of 2.8 nm^3 (2x2x0.7=2.8 (nm^3)). This scattering volume is much smaller than that of the majority of single inorganic nanostructures. This is very promising for studying vibrational properties of single nanocrystals, nanowires, nanorods *etc*. Moreover, the marked enhancement from this very small area indicates that there is a strong plasmonic interaction between the tip and the sample. Therefore, this is an ideal platform to study the plasmonic coupling effect in 1L-MoS_2 with an unprecedented spatial resolution of 2.3 nm achieved in this investigation.

In order to understand the TERS enhancement mechanism, the spectral response of the local electric field is calculated at the tip apex using the COMSOL simulation tool for a similar heterostructure. Figure 6.11b presents the local electric field distribution around the tip at 785 nm excitation and 6.11c displays the spectral response of the field for the same system. The tip radius was assumed to be 40 nm. For simplicity, the thickness of MoS_2 was taken as 1 nm. The local electric field was collected from 0.1 nm below the tip apex for every wavelength in Figure 6.11c. The applied electric field was 1 $V \cdot m^{-1}$ along the tip long axis and the local electric field was calculated at

every 5 nm step of excitation. The mesh parameter and the optical constants of the materials were the same as discussed in the previous chapter. As can be seen in Figure 6.11b-c, the local electric field is enhanced by a factor of 43 at the tip apex for 785 nm excitation. Comparing the plasmonic response of the two systems in Figure 6.11c one can see that the peak amplitude of the Au-MoS_2-Au is higher than the Au-Au tip-sample system. In the case of the Au-MoS_2-Au system two distinct features can be visible originated from the surface plasmon dipole (marked by a black arrow) and the fundamental absorption edge of MoS_2 – also known as *A* band (marked by a violet arrow). Even though the amplitude of the plasmon dipole of the Au-MoS_2-Au system decreases with slightly red shifted energy position compared to the Au-Au system, it is the coupling between the *A* band of MoS_2 and local field which increases the peak amplitude of the combined system. According to the equation 5.8, TERS enhancement is given by,

$$EF = E^4 = \left(\frac{E_{loc}}{E_{far}}\right)^4 = 43^4 = 3.4 \times 10^6 \qquad 6.4$$

This is a good agreement to the experimental enhancement factor calculated in equation 6.3. Important to note that, in the simulation the tip radius was assumed to be 40 nm. However, in experimental condition the randomness of the Au clusters at the tip apex makes it challenging to determine the exact size and shape of the cluster participating in the TERS measurement. Additionally, the TERS experiments were performed when the tip was in contact; whereas simulation was performed at a tip-sample distance of 1 nm. Therefore, all these experimental conditions will influence the measurements and thus can cause the deviation observed between experiments and simulations.

6.7: Investigation of local heterogeneities

Several high resolution TERS images of the heterostructure were acquired using a step size of 5 nm and 0.4 s of accumulation time. Figure 6.12a displays one of the images taken over an area marked by a rectangle in Figure 6.9a. As can be seen from the image, the TERS intensity is not homogeneous within a single ring and reveals strong local enhancement predominantly at the edges indicating the formation of the hot spots. Nine spectra along a line profile of the Raman intensity map crossing the ring (green dotted line in Figure 6.12a) are presented in Figure 6.12b. The intensities of both A_{1g} and A_{2u} modes around 400 cm^{-1} and 460 cm^{-1}, respectively, are steeply enhanced in the hot spot for pixel 5. The analysis of the phonon frequencies of the A_{1g} and A_{2u} modes show that they are site dependent. The frequency position of the A_{1g} mode varies from

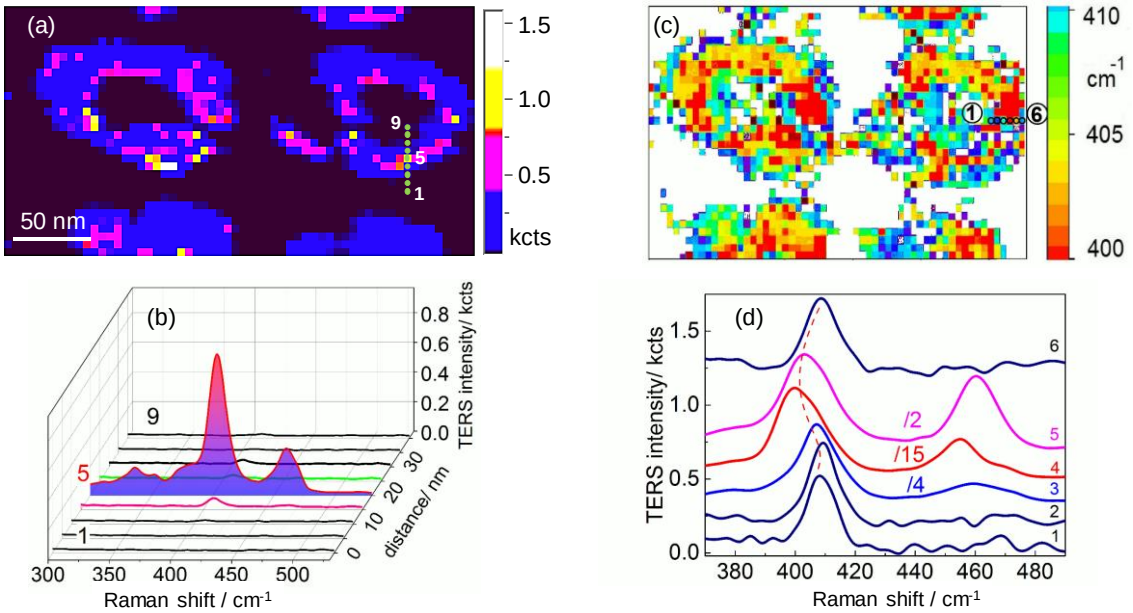

Figure 6.12: TERS image of the area indicated in Figure 6.9a by a rectangle (a). TERS spectra measured from pixels 1 to 9 along the vertical line indicated in TERS image (b). A frequency map of the A_{1g} mode of the same sample area (c). The white background shows the area where no phonon mode was detected. (d) TERS spectra measured from pixels 1 to 6 along the horizontal line indicated in image (c).

400 cm^{-1} to 410 cm^{-1} on and outside of the nanocylinders as shown in Figure 6.12c. Due to the weak plasmonic coupling between the Au tip and MoS_2 outside the Au cylinders, it is not possible to detect the Raman modes of MoS_2 (very weak S/N ratio of the Raman modes). Therefore, areas outside the Au cylinders are shown as the white background in Figure 6.12c. Moreover, as can be seen from comparison of Figures 6.12a and 6.12c, the modes having lowest frequencies are observed from the areas which reveal a strongest TERS signal. The lower frequency position of the Raman mode originating from the hot spots is most probable due to 1) the heating of the MoS_2 flake in an intense electromagnetic field localized between the tip apex and the Au nanocylinder edge, 2) hot electron doping via plasmonic coupling, and 3) biaxial strain due to morphological deformation. In order to quantify all effects, the Raman shift of A_{2u} mode is taken as the reference point of measure. This is because, firstly, temperature effects should be homogeneous for all peaks, and secondly, it is known for MoS_2 monolayer that the out-of-plane A_{1g} mode is strongly sensitive to electron phonon coupling due to its symmetry condition. Therefore, to simplify the situation the doping effect in A_{2u} mode can be excluded. Hence, the peak shifts observed for this mode are due to heating and strain effect. The effect of strain on optical properties of a MoS_2 monolayer in macro or micro scale has been studied extensively in the past few years. However, all the Raman studies

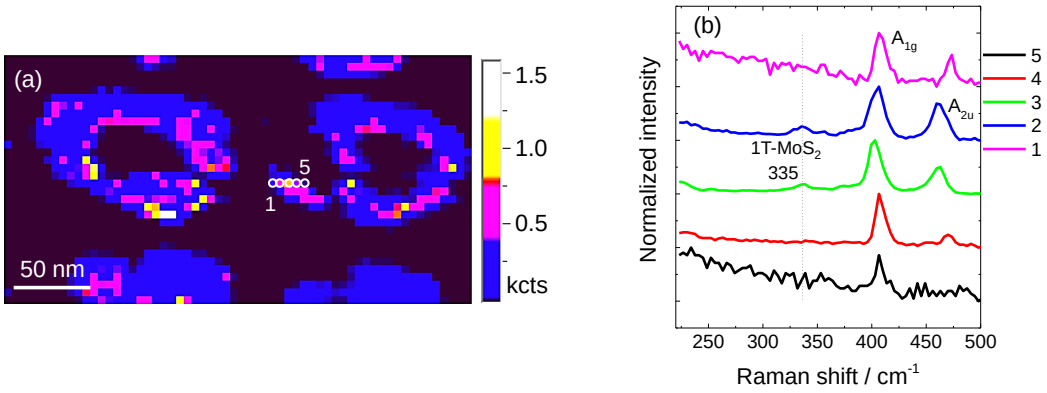

Figure 6.13: TERS image shown in 6.12a (a). Normalized TERS spectra recorded from pixels 1 to 5 marked by a white open circle (b). The Raman mode around 335 cm^{-1} indicating a phase transition in MoS_2.

mainly concentrated on in-plane E_{2g} and out-of-plane A_{1g} modes. In the previous chapter, highly localized strain in 3L MoS_2 in a MoS_2/Au nanotriangle heterostructure was investigated using TERS. It is observed that a biaxial tensile strain of 0.9 % is induced in 3L MoS_2 while following an edge of Au nanotriangle of a height of 50 nm. Since the height of the Au nanocylinders studied in the present case is the same as the nanotriangles, one can assume that the monolayer MoS_2 would experience similar amount of strain while follow the edge of these cylinders. At this strain, a peak shift of 1 cm^{-1} is found for the Raman mode around 460 cm^{-1}. Lloyd *et al.* [71] studied the biaxial strain gradient for different thicknesses of MoS_2. They observed that the strain gradient is 1.7 (2.4) times larger for the E_{2g} (A_{1g}) mode while thinning from 3L to 1L MoS_2. Since the A_{2u} mode is also an out-of-plane mode, we choose the ratio of 2.4. Using this strain gradient ratio for 3L to 1L conversion, a peak shift of 1 cm^{-1} in 3L becomes 2.4 cm^{-1} in 1L MoS_2. Now subtracting the strain contribution from the total peak shift of 4 cm^{-1} leaves a heat induced shift of 1.6 cm^{-1}. The temperature dependent Raman spectra of MoS_2 were discussed in section 5.7. It was observed that both in-plane and out-of-plane modes shift with the same rate with respect to temperature (0.014 cm^{-1}/K) in accordance with previous literature. [286-287, 289] Therefore, the temperature rise in the hot spot is determined to be 110 °C (approx.).

The strain induced A_{1g} mode shift rate for 1L MoS_2 is 1.7 cm^{-1}/%. Hence, the A_{1g} mode should shift by 1.5 cm^{-1} due to 0.9 % of biaxial strain. Now subtracting the strain + heating effect ((1.5 + 1.6) cm^{-1}) from the total peak shift of A_{1g} mode, we have an additional shift of 6.9 cm^{-1}. This amount of peak shift can be correlated to hot electron doping via strong plasmonic coupling between MoS_2 and Au nanocylinders. Using the doping gradient of 0.26 $\cdot 10^{13}$ cm^{-2}/cm^{-1} for the A_{1g} mode in MoS_2

monolayer reported by Chakraborty *et al.* [278], the carrier concentration in MoS_2 monolayer is therefore determined to be $1.8 \cdot 10^{13}$ cm^{-2}. This is 3.2 times larger than what Yu *et al.* [332] observed (an injected electron density of $5.6 \cdot 10^{12}$ cm^{-2}). This high value of electron density can be due to the different experimental configurations used in these two experiments. First, in this study, a MoS_2 monolayer is coupled to both Au nanocylinders and Au tip, meaning more probability of hot electron injection. Secondly in the case of Yu *et al.*, hot electron injection was monitored by conventional optical spectroscopy. Hence, the signal from the MoS_2 monolayer should be averaged over the area of the laser beam used. Therefore, it is possible to underestimate the value. One interesting observation of such doping in monolayer MoS_2 is the phase transition from trigonal prismatic (2H) to octahedral structure as reported by Kang *et al* [209]. In such case additional doping by hot electrons destabilizes the 2H crystal lattice and induces a reversible phase transition to the 1T phase. In this TERS investigation a Raman mode around 335 cm^{-1} is observed which does not belong to 2H-MoS_2. Moreover, the presence of this mode is site dependent as shown in Figure 6.12e (pixel 1 to 5 marked by open white circles). The highest intensity of this mode is observed at the positions where one can also observe highest intensity of A_{1g} mode and vanishes away from the bright spots. According to literature, the 1T-MoS_2 has Raman modes around 150 cm^{-1}, 226 cm^{-1} and 333 cm^{-1}. [343] In these TERS spectra, the Raman mode is observed only around 335 cm^{-1}. The other two modes are not detected due to the strong Rayleigh tail below 250 cm^{-1}. The observation of the 1T-phase is a clear indication that those sites (hot spots) act as electron donor. Thanks to the extreme spatial resolution achieved in this study, such doping sites can be resolved.

6.8: Summary

Gap- plasmon TERS imaging of a MoS_2 monolayer stamped on a gold nanocylinder array is studied using home-built TERS tips. A strong enhancement of the TERS signal of the A_{1g} peak from a monolayer MoS_2 is observed. The experimental enhancement factor is supported by theoretical simulation. However, the strongest enhancement factor of 5.1×10^8 is achieved at the circular ring of the cylinder where hot spots are created between tip and sample. An unprecedented spatial resolution of 2.3 nm is achieved in the TERS measurement. Due to strong coupling between 1L-MoS_2 and the hot spots, a doping in the order of 1.8×10^{13} cm^{-2} is observed in MoS_2 via plasmonic hot electrons. Such doping causes a structural shift from the 1H to 1T phase. Thanks to the extreme resolution, it is possible to probe these doping sites. This investigation may provide a path to the selective control of structural phase change in MoS_2 to reduce the contact resistance in a practical device application.

Chapter 7

Summary

Even though layered semiconductors are known for decades, their remarkable physical properties at atomic thickness (in 2D form) offer exciting potential in the field of nanotechnology. For device applications such as nanoelectronics and optoelectronics, the stability of the materials is a prerequisite. In chapter 4, the environmental stability of ε-GaSe is addressed. It is shown that exfoliated monolayer GaSe is oxidized almost immediately. The oxidation process is self-limiting with a penetration depth of 3 layers taking approximately a time of 5 hours to reach that thickness.

In chapter 5, heterogeneous strain in trilayer MoS_2 mechanically deposited on a nanostructured Au substrate is mapped. The peak values of strain reach up to 1.4 %. It is found that the regions of maximum local strain correspond to the regions of maximum topographic curvature extracted from AFM measurements. These results imply that in optoelectronic device applications, beyond the energy level alignment in MoS_2/metal contacts, also the strain-induced effects induced by a patterned substrate must be taken into account, which will significantly impact the local properties of this promising 2D material.

In chapter 6, the effect of local heterogeneities such as strain and doping in monolayer MoS_2 is studied. Due to strong plasmonic coupling between the tip and sample, 1L-MoS_2 experiences a doping in the order of 1.8×10^{13} cm^{-2} due to plasmonic hot electron doping. It is also observed that such doping in 1L-MoS_2 leads to a structural phase change from semiconducting 1H-MoS_2 to metallic 1T-MoS_2. Due to a superior spatial resolution of 2.3 nm with a giant enhancement factor of 5.1×10^8, it is possible to probe the doping sites. This investigation may provide a path to the selective control of structural phase change in MoS_2 to reduce the contact resistance in a practical device application.

Outlook

During my four years of endeavor in the Semiconductor Physics group at Chemnitz University of Technology, I have worked with 2D semiconductors, mainly GaSe and MoS_2. This works gave me an opportunity to gain plenty of knowledge and experience not only on these materials but also other related 2D semiconductors. From that perspective I can foresee a great potential of these materials in practical device applications.

Semiconductor p-n junctions are the fundamental building blocks for electronic and optoelectronic applications. Therefore, to realize complementary devices, both n and p-type 2D semiconductors are necessary. However, most of the TMDC materials are intrinsically n-type due to the chalcogen vacancies. Several approaches are engineered to change the doping type in TMDCs. Although obtaining a high-quality p-type semiconducting TMDC is turned out to be incredibly challenging.

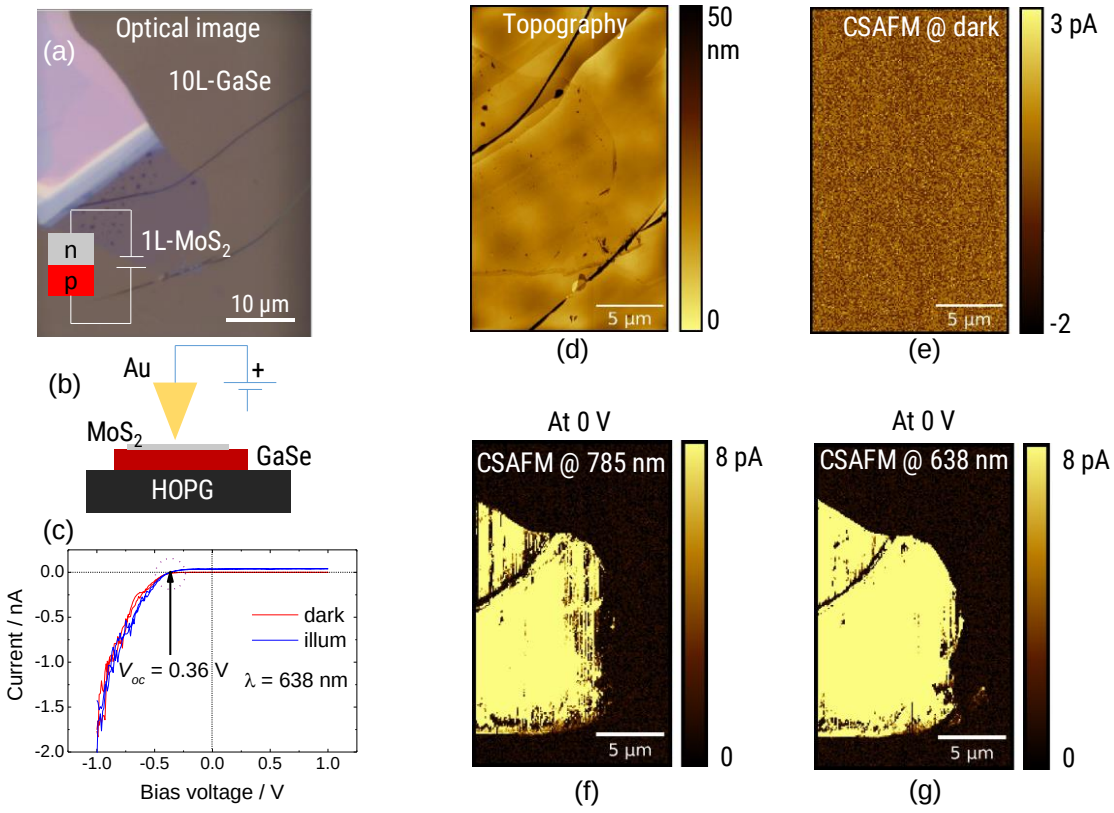

Figure I: Demonstration of vertical p-n junction made of few layer GaSe and 1L-MoS_2. The device shows a marked rectification ratio. Optical image (a) and the schematic (b) of the device. I – V characteristics of the junction in the dark and under 638 nm illumination. Topography (d), CSAFM image in dark (e), under illumination 785 nm of (f), and 638 nm (g). Both excitations are below the band gap of the materials.

Therefore, naturally available p-type GaSe can effectively complement such need. At the end of this thesis, the possibility of obtaining a vertical p-n heterojunction made of p-type GaSe and n-type MoS_2 was explored.

A p-n junction is realized by fabricating a vertical stack of few layer GaSe and a monolayer MoS_2 on a HOPG substrate. Monolayer GaSe is abstained in this investigation since it is not stable in air (as discussed in chapter 4). At least three heterojunctions are prepared for the investigation. All of them show similar I – V characteristics. Figure I shows a typical I – V characteristics of the heterojunction. The measurements were performed using AIST-NT scanning probe microscope in current sensing AFM mode. Home-built gold tips prepared by etching of a gold wire (method adopted from ref.[344]) were used for current measurement. As can be seen, the p-n junction shows a very good rectification behaviour with a rectification ratio of 10^4 at ±1 V. While illuminated with 638 nm and 785 nm excitations, the heterojunction shows a pronounced photovoltaic effect with an open circuit voltage of 0.36 V and a fill factor of 55. Interestingly both excitations are below the bandgap of the materials used in the heterojunction. Therefore, the photocurrent mechanism should be midgap assisted instead of conventional band to band transition. In order understand the current transport mechanism, temperature dependent I – V measurements and detailed theoretical calculation on the band structure of the heterostructure are required. The potential of the heterojunction will surely open up a new exciting field of research and application once the current transport mechanism is fully understood.

Appendix

A-1: Lennard – Jones potential model

Basic assumption for solving tip – sample interaction is taken from Lennard – Jones potential model,[174] which approximates the interaction between a pair of neutral atoms or molecules. Tip is assumed as a sphere of radius, R, and the sample is treated as a flat surface. Tip – sample system is modelled using two types of interactions according to the literature.[345-346] These are: 1) long range van der Waals attractive force, F_{vdW} and 2) elastic repulsive force, F_{rep} when tip is in contact. These forces are written as,

$$F_{vdW} = \begin{cases} \frac{-HR}{6d^2}, d > a_0 \\ \frac{-HR}{6a_0^2}, d > a_0 \end{cases} \quad \text{A-1}$$

$$F_{rep} = \frac{4}{3} E^* \sqrt{R} \left(a_0 - d\right)^{3/2}, \; d \le a_0 \quad \text{A-2}$$

where, H is the Hamakar constant, a_0 is the interatomic distance shown in Figure 3.2, and E^* is the effective Young modulus of the tip – sample system. Using the equation, A-1 and A-2, one can develop a force *vs* distance graph as shown in Figure 3.2a. Origin 2016 Pro data analysis software is used to solve the equation $F_{sum} = F_{vdW} + F_{rep}$ and plotted in Figure 3.2a.

A-2: Amplitude, phase *vs* distance curve

The cantilever was modelled as a harmonic oscillator described by: [347]

$$\frac{k_c}{\omega_0^2}\frac{d^2}{dt^2} z(t) + m^* \frac{\omega_0}{Q}\frac{d}{dt} z(t) + k_c z(t) - F_0 \cos\left(\omega_0 t\right) = F_{ts}(d) \quad \text{A-3}$$

where, $m^* = {k_c}/{\omega_0^2}$ is the effective mass of the tip-cantilever system, Q is the quality factor and $F_{ts}(d)$ is the instantaneous tip-sample interacting force given by:

$$F_{ts} = \begin{cases} d > a_0,\ F_{vdW} = -\left({HR}/{6(d+a_0)^2}\right) \\ d \le a_0,\ F_{rep} = {4}/{3} E^* \sqrt{Rd^3} - \left({HR}/{6a_0^2}\right) \end{cases} \qquad \text{A-4}$$

In equation A-4, an additional term of ${-HR}/{6a_0^2}$ is used as the constant adhesive force when the tip is in contact. The term a_o is an intermolecular distance of about 0.1 nm introduced to avoid the divergence of the adhesion force at contact.[346] By substituting equation A-4 into the equation A-3, the differential equation is solved numerically following a 4th order Runge-Kutta algorithm for a certain tip – sample distance. The solution gives an APD curve as shown in Figure 3.2b.

A-3: Raman tensors and TERS selection rules for MoS_2

Raman tensors of MoS_2 are studied by several groups (experimental and theoretical) and the summarized results can be found in this review article.[348] Raman intensity of any phonon mode in a material is given by,

$$I = |\boldsymbol{e}_s \cdot \Re \cdot \boldsymbol{e}_i|^2 \qquad \text{A-5}$$

Here, $\boldsymbol{e}_s$, and $\boldsymbol{e}_i$ are the polarization vector of scattered and incident light, and $\Re$ is the Raman tensor of a particular mode. Raman tensors of two dominant first order modes in MoS_2 are as follows:

$$A_{1g} = \begin{pmatrix} a & 0 & 0 \\ 0 & a & 0 \\ 0 & 0 & b \end{pmatrix} \qquad E_{2g} = \begin{pmatrix} 0 & d & 0 \\ d & 0 & 0 \\ 0 & 0 & 0 \end{pmatrix} \qquad \text{A-6}$$

Since, in TERS geometry, incident light is polarized along the direction of the plane of incidence (p-polarized), polarization vectors can be written as, $e_i = (sin\theta \quad cos\theta \quad 0)$ and $e_s = (0 \quad 1 \quad 0)$. Here θ is the angle between incidence and scattered light. Therefore, Raman intensities of A_{1g} and E_{2g} modes of MoS2 become, $I_{A_{1g}} = a^2 cos^2\theta$, and $I_{E_{2g}} = d^2$ (independent of θ). Hence, Raman intensity of A_{1g} mode strongly depends on the angle between incidence and scattered light and completely vanishes at orthogonal geometry. Though, E_{2g} mode remains constant. However, in TERS geometry, since tip is polarized perpendicular to the basal plane of the sample surface, it favours all the out-of-plane Raman modes including A_{1g} mode. On the other hand in-plane E_{2g} mode is comparatively less sensitive.

Bibliography

1. Golden, J.; McMillan, M.; Downs, R. T.; Hystad, G.; Goldstein, I.; Stein, H. J.; Zimmerman, A.; Sverjensky, D. A.; Armstrong, J. T.; Hazen, R. M., Rhenium variations in molybdenite (MoS2): Evidence for progressive subsurface oxidation. *Earth and Planetary Science Letters* **2013,** *366*, 1-5.

2. Brodie, B. C., On the Atomic Weight of Graphite. *Philosophical Transactions of the Royal Society of London* **1859,** *149*, 249-259.

3. Bhimanapati, G. R.; Lin, Z.; Meunier, V.; Jung, Y.; Cha, J.; Das, S.; Xiao, D.; Son, Y.; Strano, M. S.; Cooper, V. R.; Liang, L.; Louie, S. G.; Ringe, E.; Zhou, W.; Kim, S. S.; Naik, R. R.; Sumpter, B. G.; Terrones, H.; Xia, F.; Wang, Y.; Zhu, J.; Akinwande, D.; Alem, N.; Schuller, J. A.; Schaak, R. E.; Terrones, M.; Robinson, J. A., Recent Advances in Two-Dimensional Materials beyond Graphene. *ACS Nano* **2015,** *9* (12), 11509-11539.

4. Novoselov, K. S.; Geim, A. K.; Morozov, S. V.; Jiang, D.; Zhang, Y.; Dubonos, S. V.; Grigorieva, I. V.; Firsov, A. A., Electric Field Effect in Atomically Thin Carbon Films. *Science* **2004,** *306* (5696), 666-669.

5. Geim, A. K.; Novoselov, K. S., The rise of graphene. *Nat Mater* **2007,** *6* (3), 183-191.

6. Novoselov, K. S.; Geim, A. K.; Morozov, S. V.; Jiang, D.; Katsnelson, M. I.; Grigorieva, I. V.; Dubonos, S. V.; Firsov, A. A., Two-dimensional gas of massless Dirac fermions in graphene. *Nature* **2005,** *438* (7065), 197-200.

7. Zhang, Y.; Tan, Y.-W.; Stormer, H. L.; Kim, P., Experimental observation of the quantum Hall effect and Berry's phase in graphene. *Nature* **2005,** *438* (7065), 201-204.

8. Novoselov, K. S.; McCann, E.; Morozov, S. V.; Fal'ko, V. I.; Katsnelson, M. I.; Zeitler, U.; Jiang, D.; Schedin, F.; Geim, A. K., Unconventional quantum Hall effect and Berry/'s phase of 2pi in bilayer graphene. *Nat Phys* **2006,** *2* (3), 177-180.

9. Lui, C. H.; Li, Z.; Mak, K. F.; Cappelluti, E.; Heinz, T. F., Observation of an electrically tunable band gap in trilayer graphene. *Nat Phys* **2011,** *7* (12), 944-947.

10. Ling, X.; Wu, J.; Xie, L.; Zhang, J., Graphene-Thickness-Dependent Graphene-Enhanced Raman Scattering. *The Journal of Physical Chemistry C* **2013,** *117* (5), 2369-2376.

11. Zhou, S. Y.; Gweon, G. H.; Fedorov, A. V.; First, P. N.; de Heer, W. A.; Lee, D. H.; Guinea, F.; Castro Neto, A. H.; Lanzara, A., Substrate-induced bandgap opening in epitaxial graphene. *Nat Mater* **2007,** *6* (10), 770-775.

12. Wang, Q. H.; Kalantar-Zadeh, K.; Kis, A.; Coleman, J. N.; Strano, M. S., Electronics and optoelectronics of two-dimensional transition metal dichalcogenides. *Nat Nano* **2012,** *7* (11), 699-712.

13. Novoselov, K. S.; Jiang, D.; Schedin, F.; Booth, T. J.; Khotkevich, V. V.; Morozov, S. V.; Geim, A. K., Two-dimensional atomic crystals. *Proceedings of the National Academy of Sciences of the United States of America* **2005,** *102* (30), 10451-10453.

14. Kim, S.; Nah, J.; Jo, I.; Shahrjerdi, D.; Colombo, L.; Yao, Z.; Tutuc, E.; Banerjee, S. K., Realization of a high mobility dual-gated graphene field-effect transistor with Al2O3 dielectric. *Applied Physics Letters* **2009,** *94* (6), 062107.

15. Prezzi, D.; Varsano, D.; Ruini, A.; Marini, A.; Molinari, E., Optical properties of graphene nanoribbons: The role of many-body effects. *Physical Review B* **2008,** *77* (4), 041404.

16. Cuong, T. V.; Pham, V. H.; Tran, Q. T.; Chung, J. S.; Shin, E. W.; Kim, J. S.; Kim, E. J., Optoelectronic properties of graphene thin films prepared by thermal reduction of graphene oxide. *Materials Letters* **2010,** *64* (6), 765-767.

17. Bonaccorso, F.; Sun, Z.; Hasan, T.; Ferrari, A. C., Graphene photonics and optoelectronics. *Nat Photon* **2010,** *4* (9), 611-622.

18. Akinwande, D.; Petrone, N.; Hone, J., Two-dimensional flexible nanoelectronics. *Nature Communications* **2014,** *5*, 5678.

19. Han, M. Y.; Özyilmaz, B.; Zhang, Y.; Kim, P., Energy Band-Gap Engineering of Graphene Nanoribbons. *Physical Review Letters* **2007,** *98* (20), 206805.

20. Li, X.; Wang, X.; Zhang, L.; Lee, S.; Dai, H., Chemically Derived, Ultrasmooth Graphene Nanoribbon Semiconductors. *Science* **2008**.

21. Sahu, S.; Parashar, S. K. S.; Rout, G. C., Theoretical Study of Band Gap opening in AB- stacked Bi-layer Graphene by Impurity and Electric Field Effects. *Materials Today: Proceedings* **2016,** *3* (1), 39-44.

22. Jiao, L.; Zhang, L.; Wang, X.; Diankov, G.; Dai, H., Narrow graphene nanoribbons from carbon nanotubes. *Nature* **2009,** *458* (7240), 877-880.

23. Sols, F.; Guinea, F.; Neto, A. H. C., Coulomb Blockade in Graphene Nanoribbons. *Physical Review Letters* **2007,** *99* (16), 166803.

24. Yoon, Y.; Guo, J., Effect of edge roughness in graphene nanoribbon transistors. *Applied Physics Letters* **2007,** *91* (7), 073103.

25. Giovannetti, G.; Khomyakov, P. A.; Brocks, G.; Kelly, P. J.; van den Brink, J., Substrate-induced band gap in graphene on hexagonal boron nitride: Ab initio density functional calculations. *Physical Review B* **2007,** *76* (7), 073103.

26. Fan, X.; Shen, Z.; Liu, A. Q.; Kuo, J.-L., Band gap opening of graphene by doping small boron nitride domains. *Nanoscale* **2012,** *4* (6), 2157-2165.

27. Jung, J.; DaSilva, A. M.; MacDonald, A. H.; Adam, S., Origin of band gaps in graphene on hexagonal boron nitride. *Nature Communications* **2015,** *6*, 6308.

28. CassaboisG; ValvinP; GilB, Hexagonal boron nitride is an indirect bandgap semiconductor. *Nat Photon* **2016,** *10* (4), 262-266.

29. Mak, K. F.; Lee, C.; Hone, J.; Shan, J.; Heinz, T. F., Atomically Thin MoS_2: A New Direct-Gap Semiconductor. *Physical Review Letters* **2010,** *105* (13), 136805.

30. RadisavljevicB; RadenovicA; BrivioJ; GiacomettiV; KisA, Single-layer MoS2 transistors. *Nat Nano* **2011,** *6* (3), 147-150.

31. Fu, Y.; Long, M.; Gao, A.; Wang, Y.; Pan, C.; Liu, X.; Zeng, J.; Xu, K.; Zhang, L.; Liu, E.; Hu, W.; Wang, X.; Miao, F., Intrinsic p-type W-based transition metal dichalcogenide by substitutional Ta-doping. *Applied Physics Letters* **2017,** *111* (4), 043502.

32. Chuang, H.-J.; Tan, X.; Ghimire, N. J.; Perera, M. M.; Chamlagain, B.; Cheng, M. M.-C.; Yan, J.; Mandrus, D.; Tománek, D.; Zhou, Z., High Mobility WSe2 p- and n-Type Field-Effect Transistors Contacted by Highly Doped Graphene for Low-Resistance Contacts. *Nano Letters* **2014,** *14* (6), 3594-3601.

33. Zhang, Y. J.; Ye, J. T.; Yomogida, Y.; Takenobu, T.; Iwasa, Y., Formation of a Stable p–n Junction in a Liquid-Gated MoS2 Ambipolar Transistor. *Nano Letters* **2013,** *13* (7), 3023-3028.

34. Liu, X.; Qu, D.; Ryu, J.; Ahmed, F.; Yang, Z.; Lee, D.; Yoo, W. J., P-Type Polar Transition of Chemically Doped Multilayer MoS2 Transistor. *Advanced Materials* **2016,** *28* (12), 2345-2351.

35. Lei, S.; Ge, L.; Liu, Z.; Najmaei, S.; Shi, G.; You, G.; Lou, J.; Vajtai, R.; Ajayan, P. M., Synthesis and Photoresponse of Large GaSe Atomic Layers. *Nano Letters* **2013,** *13* (6), 2777-2781.

36. Hu, P.; Wen, Z.; Wang, L.; Tan, P.; Xiao, K., Synthesis of Few-Layer GaSe Nanosheets for High Performance Photodetectors. *ACS Nano* **2012,** *6* (7), 5988-5994.

37. Jin, H.; Li, J.; Dai, Y.; Wei, Y., Engineering the electronic and optoelectronic properties of InX (X = S, Se, Te) monolayers via strain. *Physical Chemistry Chemical Physics* **2017,** *19* (6), 4855-4860.

38. Ho, C. H.; Lin, S. L., Optical properties of the interband transitions of layered gallium sulfide. *Journal of Applied Physics* **2006,** *100* (8), 083508.

39. Bube, R. H.; Lind, E. L., Photoconductivity of Gallium Selenide Crystals. *Physical Review* **1959,** *115* (5), 1159-1164.

40. Nagai, Y.; Maeda, K.; Suzuki, K.; Oyama, Y., Comparative Study of Shallow Acceptor Levels in Unintentionally Doped p-Type GaSe Crystals Prepared by the Bridgman and Liquid Phase Solution Growth Methods. *Journal of Electronic Materials* **2014,** *43* (9), 3117-3120.

41. Tao, L.; Cinquanta, E.; Chiappe, D.; Grazianetti, C.; Fanciulli, M.; Dubey, M.; Molle, A.; Akinwande, D., Silicene field-effect transistors operating at room temperature. *Nat Nano* **2015,** *10* (3), 227-231.

42. Li, L.; Yu, Y.; Ye, G. J.; Ge, Q.; Ou, X.; Wu, H.; Feng, D.; Chen, X. H.; Zhang, Y., Black phosphorus field-effect transistors. *Nat Nano* **2014,** *9* (5), 372-377.

43. Zhang, L.; Bampoulis, P.; Rudenko, A. N.; Yao, Q.; van Houselt, A.; Poelsema, B.; Katsnelson, M. I.; Zandvliet, H. J. W., Structural and Electronic Properties of Germanene on MoS_2 *Physical Review Letters* **2016,** *116* (25), 256804.

44. Cai, Y.; Chuu, C.-P.; Wei, C. M.; Chou, M. Y., Stability and electronic properties of two-dimensional silicene and germanene on graphene. *Physical Review B* **2013,** *88* (24), 245408.

45. Joshua, O. I.; Gary, A. S.; Herre, S. J. v. d. Z.; Andres, C.-G., Environmental instability of few-layer black phosphorus. *2D Materials* **2015,** *2* (1), 011002.

46. Splendiani, A.; Sun, L.; Zhang, Y.; Li, T.; Kim, J.; Chim, C.-Y.; Galli, G.; Wang, F., Emerging Photoluminescence in Monolayer MoS2. *Nano Letters* **2010,** *10* (4), 1271-1275.

47. Mak, K. F.; He, K.; Lee, C.; Lee, G. H.; Hone, J.; Heinz, T. F.; Shan, J., Tightly bound trions in monolayer MoS2. *Nat Mater* **2013,** *12* (3), 207-211.

48. Peng, Q.; De, S., Outstanding mechanical properties of monolayer MoS2 and its application in elastic energy storage. *Physical Chemistry Chemical Physics* **2013,** *15* (44), 19427-19437.

49. Li, Z.; Ye, R.; Feng, R.; Kang, Y.; Zhu, X.; Tour, J. M.; Fang, Z., Graphene Quantum Dots Doping of MoS2 Monolayers. *Advanced Materials* **2015,** *27* (35), 5235-5240.

50. Bellus, M. Z.; Ceballos, F.; Chiu, H.-Y.; Zhao, H., Tightly Bound Trions in Transition Metal Dichalcogenide Heterostructures. *ACS Nano* **2015,** *9* (6), 6459-6464.

51. Mouri, S.; Miyauchi, Y.; Matsuda, K., Tunable Photoluminescence of Monolayer MoS_2 via Chemical Doping. *Nano Letters* **2013,** *13* (12), 5944-5948.

52. Lui, C. H.; Frenzel, A. J.; Pilon, D. V.; Lee, Y. H.; Ling, X.; Akselrod, G. M.; Kong, J.; Gedik, N., Trion-Induced Negative Photoconductivity in Monolayer MoS_2 *Physical Review Letters* **2014,** *113* (16), 166801.

53. Gomez, L.; Aberg, I.; Hoyt, J. L., Electron Transport in Strained-Silicon Directly on Insulator Ultrathin-Body n-MOSFETs With Body Thickness Ranging From 2 to 25 nm. *IEEE Electron Device Letters* **2007,** *28* (4), 285-287.

54. Radisavljevic B.; Radenovic A.; Brivio J.; Giacometti V.; Kis A., Single-layer MoS2 transistors. *Nat Nano* **2011,** *6* (3), 147-150.

55. Mai, C.; Barrette, A.; Yu, Y.; Semenov, Y. G.; Kim, K. W.; Cao, L.; Gundogdu, K., Many-Body Effects in Valleytronics: Direct Measurement of Valley Lifetimes in Single-Layer MoS2. *Nano Letters* **2014,** *14* (1), 202-206.

56. Zeng, H.; Dai, J.; Yao, W.; Xiao, D.; Cui, X., Valley polarization in MoS2 monolayers by optical pumping. *Nat Nano* **2012,** *7* (8), 490-493.

57. Karvonen, L.; Säynätjoki, A.; Mehravar, S.; Rodriguez, R. D.; Hartmann, S.; Zahn, D. R.; Honkanen, S.; Norwood, R. A.; Peyghambarian, N.; Kieu, K., Investigation of second-and third-

harmonic generation in few-layer gallium selenide by multiphoton microscopy. *Scientific reports* **2015,** *5*.

58. Rybkovskiy, D. V.; Arutyunyan, N. R.; Orekhov, A. S.; Gromchenko, I. A.; Vorobiev, I. V.; Osadchy, A. V.; Salaev, E. Y.; Baykara, T. K.; Allakhverdiev, K. R.; Obraztsova, E. D., Size-induced effects in gallium selenide electronic structure: The influence of interlayer interactions. *Physical Review B* **2011,** *84* (8), 085314.

59. Schwarz, S.; Dufferwiel, S.; Walker, P. M.; Withers, F.; Trichet, A. A. P.; Sich, M.; Li, F.; Chekhovich, E. A.; Borisenko, D. N.; Kolesnikov, N. N.; Novoselov, K. S.; Skolnick, M. S.; Smith, J. M.; Krizhanovskii, D. N.; Tartakovskii, A. I., Two-Dimensional Metal–Chalcogenide Films in Tunable Optical Microcavities. *Nano Letters* **2014,** *14* (12), 7003-7008.

60. Pozo-Zamudio, O. D.; Schwarz, S.; Sich, M.; Akimov, I. A.; Bayer, M.; Schofield, R. C.; Chekhovich, E. A.; Robinson, B. J.; Kay, N. D.; Kolosov, O. V.; Dmitriev, A. I.; Lashkarev, G. V.; Borisenko, D. N.; Kolesnikov, N. N.; Tartakovskii, A. I., Photoluminescence of two-dimensional GaTe and GaSe films. *2D Materials* **2015,** *2* (3), 035010.

61. Kim, W.; Li, C.; Chaves, F. A.; Jiménez, D.; Rodriguez, R. D.; Susoma, J.; Fenner, M. A.; Lipsanen, H.; Riikonen, J., Tunable Graphene–GaSe Dual Heterojunction Device. *Advanced Materials* **2016,** *28* (9), 1845-1852.

62. Wang, P.; Zhang, W.; Liang, O.; Pantoja, M.; Katzer, J.; Schroeder, T.; Xie, Y.-H., Giant Optical Response from Graphene–Plasmonic System. *ACS Nano* **2012,** *6* (7), 6244-6249.

63. Gan, X.; Mak, K. F.; Gao, Y.; You, Y.; Hatami, F.; Hone, J.; Heinz, T. F.; Englund, D., Strong Enhancement of Light–Matter Interaction in Graphene Coupled to a Photonic Crystal Nanocavity. *Nano Letters* **2012,** *12* (11), 5626-5631.

64. Wang, S.; Li, S.; Chervy, T.; Shalabney, A.; Azzini, S.; Orgiu, E.; Hutchison, J. A.; Genet, C.; Samorì, P.; Ebbesen, T. W., Coherent Coupling of WS2 Monolayers with Metallic Photonic Nanostructures at Room Temperature. *Nano Letters* **2016,** *16* (7), 4368-4374.

65. Sun, Z.; Martinez, A.; Wang, F., Optical modulators with 2D layered materials. *Nat Photon* **2016,** *10* (4), 227-238.

66. Xia, F.; Wang, H.; Xiao, D.; Dubey, M.; Ramasubramaniam, A., Two-dimensional material nanophotonics. *Nat Photon* **2014,** *8* (12), 899-907.

67. Li, Z.; Xiao, Y.; Gong, Y.; Wang, Z.; Kang, Y.; Zu, S.; Ajayan, P. M.; Nordlander, P.; Fang, Z., Active Light Control of the MoS2 Monolayer Exciton Binding Energy. *ACS Nano* **2015,** *9* (10), 10158-10164.

68. Smith, J. G.; Faucheaux, J. A.; Jain, P. K., Plasmon resonances for solar energy harvesting: A mechanistic outlook. *Nano Today* **2015,** *10* (1), 67-80.

69. Mousavi, S. S.; Stöhr, A.; Berini, P., Plasmonic photodetector with terahertz electrical bandwidth. *Applied Physics Letters* **2014,** *104* (14), 143112.

70. Ma, X.-C.; Dai, Y.; Yu, L.; Huang, B.-B., Energy transfer in plasmonic photocatalytic composites. *Light Sci Appl* **2016,** *5*, e16017.

71. Lloyd, D.; Liu, X.; Christopher, J. W.; Cantley, L.; Wadehra, A.; Kim, B. L.; Goldberg, B. B.; Swan, A. K.; Bunch, J. S., Band Gap Engineering with Ultralarge Biaxial Strains in Suspended Monolayer MoS2. *Nano Letters* **2016,** *16* (9), 5836-5841.

72. Tiwari, A. S. M., *Advanced 2D Materials*. Wiley Online Library: 2016.

73. Allakhverdiev, K. R.; Yetis, M. Ö.; Özbek, S.; Baykara, T. K.; Salaev, E. Y., Effective nonlinear GaSe crystal. Optical properties and applications. *Laser Physics* **2009,** *19* (5), 1092-1104.

74. Jie, W.; Chen, X.; Li, D.; Xie, L.; Hui, Y. Y.; Lau, S. P.; Cui, X.; Hao, J., Layer-Dependent Nonlinear Optical Properties and Stability of Non-Centrosymmetric Modification in Few-Layer GaSe Sheets. *Angewandte Chemie International Edition* **2015,** *54* (4), 1185-1189.

75. Zhou, X.; Cheng, J.; Zhou, Y.; Cao, T.; Hong, H.; Liao, Z.; Wu, S.; Peng, H.; Liu, K.; Yu, D., Strong Second-Harmonic Generation in Atomic Layered GaSe. *Journal of the American Chemical Society* **2015,** *137* (25), 7994-7997.

76. Karvonen, L.; Säynätjoki, A.; Mehravar, S.; Rodriguez, R. D.; Hartmann, S.; Zahn, D. R. T.; Honkanen, S.; Norwood, R. A.; Peyghambarian, N.; Kieu, K.; Lipsanen, H.; Riikonen, J., Investigation of Second- and Third-Harmonic Generation in Few-Layer Gallium Selenide by Multiphoton Microscopy. *Scientific Reports* **2015,** *5*, 10334.

77. Shi, W.; Ding, Y. J., A monochromatic and high-power terahertz source tunable in the ranges of 2.7–38.4 and 58.2–3540 μm for variety of potential applications. *Applied Physics Letters* **2004,** *84* (10), 1635-1637.

78. Zhou, Y.; Nie, Y.; Liu, Y.; Yan, K.; Hong, J.; Jin, C.; Zhou, Y.; Yin, J.; Liu, Z.; Peng, H., Epitaxy and Photoresponse of Two-Dimensional GaSe Crystals on Flexible Transparent Mica Sheets. *ACS Nano* **2014,** *8* (2), 1485-1490.

79. Segura, A.; Besson, J. M.; Chevy, A.; Martin, M. S., Photovoltaic properties of GaSe and InSe junctions. *Nuov Cim B* **1977,** *38* (2), 345-351.

80. Hui, C.; Jun, K.; Hasan, S.; Bin, C.; Aslihan, S.; Kedi, W.; Francois, P.; Xiuqing, M.; Sefaattin, T., Exciton pumping across type-I gallium chalcogenide heterojunctions. *Nanotechnology* **2016,** *27* (6), 065203.

81. Philipp, T.; Stefan, S.; Johannes, K.; Iris, N.; Osvaldo Del, P.-Z.; Alexander, I. D.; Anatoly, P. B.; Dmitry, N. B.; Nikolai, N. K.; Alexander, I. T.; Steffen Michaelis de, V.; Rudolf, B., Single-photon emitters in GaSe. *2D Materials* **2017,** *4* (2), 021010.

82. Savchyn, V. P.; Kytsai, V. B., Photoelectric properties of heterostructures based on thermo-oxidated GaSe and InSe crystals. *Thin Solid Films* **2000,** *361–362*, 123-125.

83. Late, D. J.; Liu, B.; Luo, J.; Yan, A.; Matte, H. S. S. R.; Grayson, M.; Rao, C. N. R.; Dravid, V. P., GaS and GaSe Ultrathin Layer Transistors. *Advanced Materials* **2012,** *24* (26), 3549-3554.

84. Plucinski, L.; Johnson, R. L.; Kowalski, B. J.; Kopalko, K.; Orlowski, B. A.; Kovalyuk, Z. D.; Lashkarev, G. V., Electronic band structure of GaSe(0001): Angle-resolved photoemission and ab initio theory. *Physical Review B* **2003,** *68* (12), 125304.

85. Kuhn, A.; Chevy, A.; Chevalier, R., Crystal structure and interatomic distances in GaSe. *physica status solidi (a)* **1975,** *31* (2), 469-475.

86. Yoshida, H.; Nakashima, S.; Mitsuishi, A., Phonon Raman spectra of layer compound GaSe. *physica status solidi (b)* **1973,** *59* (2), 655-666.

87. Allakhverdiev, K.; Baykara, T.; Ellialtioğlu, Ş.; Hashimzade, F.; Huseinova, D.; Kawamura, K.; Kaya, A. A.; Kulibekov, A. M.; Onari, S., Lattice vibrations of pure and doped GaSe. *Materials Research Bulletin* **2006,** *41* (4), 751-763.

88. Le Toullec, R.; Balkanski, M.; Besson, J. M.; Kuhn, A., Optical absorption edge of a new GaSe polytype. *Physics Letters A* **1975,** *55* (4), 245-246.

89. Aulich, E.; Brebner, J. L.; Mooser, E., Indirect Energy Gap in GaSe and GaS. *physica status solidi (b)* **1969,** *31* (1), 129-131.

90. Chiei, T.; Chihiro, H.; Hiroshi, T.; Junkichi, N., Electrical and Optical Properties of GaSe. *Japanese Journal of Applied Physics* **1971,** *10* (12), 1698.

91. Voevodin, V. G.; Voevodina, O. V.; Bereznaya, S. A.; Korotchenko, Z. V.; Morozov, A. N.; Sarkisov, S. Y.; Fernelius, N. C.; Goldstein, J. T., Large single crystals of gallium selenide: growing, doping by In and characterization. *Optical Materials* **2004,** *26* (4), 495-499.

92. Daniel, A.-P.; Ana, C.; Juan, P. M.-P.; Juan, F. S.-R., Quantum size confinement in gallium selenide nanosheets: band gap tunability versus stability limitation. *Nanotechnology* **2017,** *28* (17), 175701.

93. Jung, C. S.; Shojaei, F.; Park, K.; Oh, J. Y.; Im, H. S.; Jang, D. M.; Park, J.; Kang, H. S., Red-to-Ultraviolet Emission Tuning of Two-Dimensional Gallium Sulfide/Selenide. *ACS Nano* **2015,** *9* (10), 9585-9593.

94. Anis, M. K.; Piercy, A. R., Electrical conduction in p-GaSe. *Journal of Physics D: Applied Physics* **1984,** *17* (6), 1229.

95. Augelli, V.; Manfredotti, C.; Murri, R.; Vasanelli, L., Hall-mobility anisotropy in GaSe. *Physical Review B* **1978,** *17* (8), 3221-3226.

96. Schmid Ph., M. E., Anisotropy of Hole Mobility in GaSe. *Helvetica Physica Acta* **1972,** *45* (6), 870.

97. Cao, Y.; Cai, K.; Hu, P.; Zhao, L.; Yan, T.; Luo, W.; Zhang, X.; Wu, X.; Wang, K.; Zheng, H., Strong enhancement of photoresponsivity with shrinking the electrodes spacing in few layer GaSe photodetectors. *Scientific Reports* **2015,** *5*, 8130.

98. Mahfujur, R.; Raul, D. R.; Manuel, M.; Santos, A. L.-R.; Dietrich, R. T. Z., GaSe oxidation in air: from bulk to monolayers. *Semiconductor Science and Technology* **2017,** *32* (10), 105004.

99. Chhowalla, M.; Shin, H. S.; Eda, G.; Li, L.-J.; Loh, K. P.; Zhang, H., The chemistry of two-dimensional layered transition metal dichalcogenide nanosheets. *Nature Chemistry* **2013,** *5*, 263.

100. Nourbakhsh, A.; Zubair, A.; Sajjad, R. N.; Tavakkoli K. G, A.; Chen, W.; Fang, S.; Ling, X.; Kong, J.; Dresselhaus, M. S.; Kaxiras, E.; Berggren, K. K.; Antoniadis, D.; Palacios, T., MoS2 Field-Effect Transistor with Sub-10 nm Channel Length. *Nano Letters* **2016,** *16* (12), 7798-7806.

101. Lopez-Sanchez, O.; Lembke, D.; Kayci, M.; Radenovic, A.; Kis, A., Ultrasensitive photodetectors based on monolayer MoS2. *Nat Nano* **2013,** *8* (7), 497-501.

102. Tsai, M.-L.; Su, S.-H.; Chang, J.-K.; Tsai, D.-S.; Chen, C.-H.; Wu, C.-I.; Li, L.-J.; Chen, L.-J.; He, J.-H., Monolayer MoS2 Heterojunction Solar Cells. *ACS Nano* **2014**.

103. Parzinger, E.; Miller, B.; Blaschke, B.; Garrido, J. A.; Ager, J. W.; Holleitner, A.; Wurstbauer, U., Photocatalytic Stability of Single- and Few-Layer MoS2. *ACS Nano* **2015,** *9* (11), 11302-11309.

104. Plechinger, G.; Nagler, P.; Arora, A.; Schmidt, R.; Chernikov, A.; del Águila, A. G.; Christianen, P. C. M.; Bratschitsch, R.; Schüller, C.; Korn, T., Trion fine structure and coupled spin–valley dynamics in monolayer tungsten disulfide. *Nature Communications* **2016,** *7*, 12715.

105. Castellanos-Gomez, A., Why all the fuss about 2D semiconductors? *Nat Photon* **2016,** *10* (4), 202-204.

106. Wang M. Zhimming, W. A., Salamo Greg, Kishimoto Naoki, Bellucci Stefano, Park J. Young, Progress on the Theoretical Study

of Two-Dimensional MoS2 Monolayer and Nanoribbon. In *MoS2, Materials, Physics, and Devices*, Zhimming, W. M., Ed. Springer: 2014; Vol. 21.

107. Jiang, J.-W., Graphene versus MoS2: A short review. *Frontiers of Physics* **2015,** *10* (3), 287-302.

108. Liang, L.; Meunier, V., First-principles Raman spectra of MoS2, WS2 and their heterostructures. *Nanoscale* **2014,** *6* (10), 5394-5401.

109. Kappera, R.; Voiry, D.; Yalcin, S. E.; Jen, W.; Acerce, M.; Torrel, S.; Branch, B.; Lei, S.; Chen, W.; Najmaei, S.; Lou, J.; Ajayan, P. M.; Gupta, G.; Mohite, A. D.; Chhowalla, M., Metallic 1T phase source/drain electrodes for field effect transistors from chemical vapor deposited MoS2. *APL Materials* **2014,** *2* (9), 092516.

110. Kappera, R.; Voiry, D.; Yalcin, S. E.; Branch, B.; Gupta, G.; Mohite, A. D.; Chhowalla, M., Phase-engineered low-resistance contacts for ultrathin MoS2 transistors. *Nature Materials* **2014,** *13*, 1128.

111. Cho, S.; Kim, S.; Kim, J. H.; Zhao, J.; Seok, J.; Keum, D. H.; Baik, J.; Choe, D.-H.; Chang, K. J.; Suenaga, K.; Kim, S. W.; Lee, Y. H.; Yang, H., Phase patterning for ohmic homojunction contact in $MoTe_2$ *Science* **2015,** *349* (6248), 625-628.

112. Dendzik, M.; Fusté, A. B.; Michiardi, M.; Ngankeu, A. S.; Bianchi, M.; Miwa, J.; Hammer, B.; Hofmann, P.; Sanders, C., Contact-Induced Semiconductor-to-Metal Transition in Single-Layer WS_2. *Physical Review B* **2017,** *, in press*.

113. Tonndorf, P.; Schmidt, R.; Böttger, P.; Zhang, X.; Börner, J.; Liebig, A.; Albrecht, M.; Kloc, C.; Gordan, O.; Zahn, D. R. T.; Michaelis de Vasconcellos, S.; Bratschitsch, R., Photoluminescence emission and Raman response of monolayer MoS_2, $MoSe_2$, and WSe_2. *Opt. Express* **2013,** *21* (4), 4908-4916.

114. Kumar, A.; Ahluwalia, P. K., Electronic structure of transition metal dichalcogenides monolayers 1H-MX_2 (M = Mo, W; X = S, Se, Te) from ab-initio theory: new direct band gap semiconductors. *The European Physical Journal B* **2012,** *85* (6), 186.

115. Yun, W. S.; Han, S. W.; Hong, S. C.; Kim, I. G.; Lee, J. D., Thickness and strain effects on electronic structures of transition metal dichalcogenides: 2H-MX_2 semiconductors (M=Mo, W; X= S, Se, Te). *Physical Review B* **2012,** *85* (3), 033305.

116. Jin, W.; Yeh, P.-C.; Zaki, N.; Zhang, D.; Sadowski, J. T.; Al-Mahboob, A.; van der Zande, A. M.; Chenet, D. A.; Dadap, J. I.; Herman, I. P.; Sutter, P.; Hone, J.; Osgood, R. M., Direct Measurement of the Thickness-Dependent Electronic Band Structure of MoS_2 Using Angle-Resolved Photoemission Spectroscopy. *Physical Review Letters* **2013,** *111* (10), 106801.

117. Beal, A. R.; Knights, J. C.; Liang, W. Y., Transmission spectra of some transition metal dichalcogenides. II. Group VIA: trigonal prismatic coordination. *Journal of Physics C: Solid State Physics* **1972,** *5* (24), 3540.

118. Bordas, J.; Davis, E. A., Electromodulation Spectroscopy of Excitons: Molybdenum Disulphide. *physica status solidi (b)* **1973,** *60* (2), 505-510.

119. Goto, T.; Kato, Y.; Uchida, K.; Miura, N., Exciton absorption spectra of MoS 2 crystals in high magnetic fields up to 150 T. *Journal of Physics: Condensed Matter* **2000,** *12* (30), 6719.

120. Saigal, N.; Sugunakar, V.; Ghosh, S., Exciton binding energy in bulk MoS2: A reassessment. *Applied Physics Letters* **2016,** *108* (13), 132105.

121. Ramasubramaniam, A., Large excitonic effects in monolayers of molybdenum and tungsten dichalcogenides. *Physical Review B* **2012,** *86* (11), 115409.

122. Qiu, D. Y.; da Jornada, F. H.; Louie, S. G., Optical Spectrum of MoS_2: Many-Body Effects and Diversity of Exciton States. *Physical Review Letters* **2013,** *111* (21), 216805.

123. Konabe, S.; Okada, S., Effect of Coulomb interactions on optical properties of monolayer transition-metal dichalcogenides. *Physical Review B* **2014,** *90* (15), 155304.

124. Zhang, C.; Johnson, A.; Hsu, C.-L.; Li, L.-J.; Shih, C.-K., Direct Imaging of Band Profile in Single Layer MoS2 on Graphite: Quasiparticle Energy Gap, Metallic Edge States, and Edge Band Bending. *Nano Letters* **2014,** *14* (5), 2443-2447.

125. Klots, A. R.; Newaz, A. K. M.; Wang, B.; Prasai, D.; Krzyzanowska, H.; Lin, J.; Caudel, D.; Ghimire, N. J.; Yan, J.; Ivanov, B. L.; Velizhanin, K. A.; Burger, A.; Mandrus, D. G.; Tolk, N. H.; Pantelides, S. T.; Bolotin, K. I., Probing excitonic states in suspended two-dimensional semiconductors by photocurrent spectroscopy. *Scientific Reports* **2014,** *4*, 6608.

126. Hill, H. M.; Rigosi, A. F.; Roquelet, C.; Chernikov, A.; Berkelbach, T. C.; Reichman, D. R.; Hybertsen, M. S.; Brus, L. E.; Heinz, T. F., Observation of Excitonic Rydberg States in Monolayer MoS2 and WS2 by Photoluminescence Excitation Spectroscopy. *Nano Letters* **2015,** *15* (5), 2992-2997.

127. Kylänpää, I.; Komsa, H.-P., Binding energies of exciton complexes in transition metal dichalcogenide monolayers and effect of dielectric environment. *Physical Review B* **2015,** *92* (20), 205418.

128. Sie, E. J.; Frenzel, A. J.; Lee, Y.-H.; Kong, J.; Gedik, N., Intervalley biexcitons and many-body effects in monolayer MoS_2. *Physical Review B* **2015,** *92* (12), 125417.

129. Low, T.; Chaves, A.; Caldwell, J. D.; Kumar, A.; Fang, N. X.; Avouris, P.; Heinz, T. F.; Guinea, F.; Martin-Moreno, L.; Koppens, F., Polaritons in layered two-dimensional materials. *Nature Materials* **2016,** *16*, 182.

130. Qiu, H.; Xu, T.; Wang, Z.; Ren, W.; Nan, H.; Ni, Z.; Chen, Q.; Yuan, S.; Miao, F.; Song, F.; Long, G.; Shi, Y.; Sun, L.; Wang, J.; Wang, X., Hopping transport through defect-induced localized states in molybdenum disulphide. *Nature Communications* **2013,** *4*, 2642.

131. Tongay, S.; Suh, J.; Ataca, C.; Fan, W.; Luce, A.; Kang, J. S.; Liu, J.; Ko, C.; Raghunathanan, R.; Zhou, J.; Ogletree, F.; Li, J.; Grossman, J. C.; Wu, J., Defects activated photoluminescence in two-dimensional semiconductors: interplay between bound, charged, and free excitons. *Scientific Reports* **2013,** *3*, 2657.

132. Suh, J.; Park, T.-E.; Lin, D.-Y.; Fu, D.; Park, J.; Jung, H. J.; Chen, Y.; Ko, C.; Jang, C.; Sun, Y.; Sinclair, R.; Chang, J.; Tongay, S.; Wu, J., Doping against the Native Propensity of MoS2: Degenerate Hole Doping by Cation Substitution. *Nano Letters* **2014,** *14* (12), 6976-6982.

133. Kaasbjerg, K.; Thygesen, K. S.; Jacobsen, K. W., Phonon-limited mobility in n-type single-layer MoS${}_{2}$ from first principles. *Physical Review B* **2012,** *85* (11), 115317.

134. Baugher, B. W. H.; Churchill, H. O. H.; Yang, Y.; Jarillo-Herrero, P., Intrinsic Electronic Transport Properties of High-Quality Monolayer and Bilayer MoS2. *Nano Letters* **2013,** *13* (9), 4212-4216.

135. Ye, M.; Zhang, D.; Yap, Y., Recent Advances in Electronic and Optoelectronic Devices Based on Two-Dimensional Transition Metal Dichalcogenides. *Electronics* **2017,** *6* (2), 43.

136. Karim, G.; Mohamed, B.; Zhesheng, C.; Abhay, S., High quality 2D crystals made by anodic bonding: a general technique for layered materials. *Nanotechnology* **2012,** *23* (50), 505709.

137. Lee, Y.-H.; Yu, L.; Wang, H.; Fang, W.; Ling, X.; Shi, Y.; Lin, C.-T.; Huang, J.-K.; Chang, M.-T.; Chang, C.-S.; Dresselhaus, M.; Palacios, T.; Li, L.-J.; Kong, J., Synthesis and Transfer of Single-Layer Transition Metal Disulfides on Diverse Surfaces. *Nano Letters* **2013,** *13* (4), 1852-1857.

138. Andres, C.-G.; Michele, B.; Rianda, M.; Vibhor, S.; Laurens, J.; Herre, S. J. v. d. Z.; Gary, A. S., Deterministic transfer of two-dimensional materials by all-dry viscoelastic stamping. *2D Materials* **2014,** *1* (1), 011002.

139. Desai, S. B.; Madhvapathy, S. R.; Amani, M.; Kiriya, D.; Hettick, M.; Tosun, M.; Zhou, Y.; Dubey, M.; Ager, J. W.; Chrzan, D.; Javey, A., Gold-Mediated Exfoliation of Ultralarge Optoelectronically-Perfect Monolayers. *Advanced Materials* **2016,** *28* (21), 4053-4058.

140. Joensen, P.; Frindt, R. F.; Morrison, S. R., Single-layer MoS2. *Materials Research Bulletin* **1986,** *21* (4), 457-461.

141. Coleman, J. N.; Lotya, M.; O'Neill, A.; Bergin, S. D.; King, P. J.; Khan, U.; Young, K.; Gaucher, A.; De, S.; Smith, R. J.; Shvets, I. V.; Arora, S. K.; Stanton, G.; Kim, H.-Y.; Lee, K.; Kim, G. T.; Duesberg, G. S.; Hallam, T.; Boland, J. J.; Wang, J. J.; Donegan, J. F.; Grunlan, J. C.; Moriarty, G.; Shmeliov, A.; Nicholls, R. J.; Perkins, J. M.; Grieveson, E. M.; Theuwissen, K.; McComb, D. W.; Nellist, P. D.; Nicolosi, V., Two-Dimensional Nanosheets Produced by Liquid Exfoliation of Layered Materials. *Science* **2011,** *331* (6017), 568-571.

142. Zheng, J.; Zhang, H.; Dong, S.; Liu, Y.; Tai Nai, C.; Suk Shin, H.; Young Jeong, H.; Liu, B.; Ping Loh, K., High yield exfoliation of two-dimensional chalcogenides using sodium naphthalenide. *Nature Communications* **2014,** *5*, 2995.

143. Yazyev, O. V.; Kis, A., MoS2 and semiconductors in the flatland. *Materials Today* **2015,** *18* (1), 20-30.

144. Py, M. A.; Haering, R. R., Structural destabilization induced by lithium intercalation in MoS2 and related compounds. *Canadian Journal of Physics* **1983,** *61* (1), 76-84.

145. Eda, G.; Yamaguchi, H.; Voiry, D.; Fujita, T.; Chen, M.; Chhowalla, M., Photoluminescence from Chemically Exfoliated MoS2. *Nano Letters* **2011,** *11* (12), 5111-5116.

146. Ramakrishna Matte, H. S. S.; Gomathi, A.; Manna, A. K.; Late, D. J.; Datta, R.; Pati, S. K.; Rao, C. N. R., MoS2 and WS2 Analogues of Graphene. *Angewandte Chemie International Edition* **2010,** *49* (24), 4059-4062.

147. Smith, R. J.; King, P. J.; Lotya, M.; Wirtz, C.; Khan, U.; De, S.; O'Neill, A.; Duesberg, G. S.; Grunlan, J. C.; Moriarty, G.; Chen, J.; Wang, J.; Minett, A. I.; Nicolosi, V.; Coleman, J. N., Large-Scale Exfoliation of Inorganic Layered Compounds in Aqueous Surfactant Solutions. *Advanced Materials* **2011,** *23* (34), 3944-3948.

148. Zhan, Y.; Liu, Z.; Najmaei, S.; Ajayan, P. M.; Lou, J., Large-Area Vapor-Phase Growth and Characterization of MoS2 Atomic Layers on a SiO2 Substrate. *Small* **2012,** *8* (7), 966-971.

149. Liu, K.-K.; Zhang, W.; Lee, Y.-H.; Lin, Y.-C.; Chang, M.-T.; Su, C.-Y.; Chang, C.-S.; Li, H.; Shi, Y.; Zhang, H.; Lai, C.-S.; Li, L.-J., Growth of Large-Area and Highly Crystalline MoS2 Thin Layers on Insulating Substrates. *Nano Letters* **2012,** *12* (3), 1538-1544.

150. Lee, Y.-H.; Zhang, X.-Q.; Zhang, W.; Chang, M.-T.; Lin, C.-T.; Chang, K.-D.; Yu, Y.-C.; Wang, J. T.-W.; Chang, C.-S.; Li, L.-J.; Lin, T.-W., Synthesis of Large-Area MoS2 Atomic Layers with Chemical Vapor Deposition. *Advanced Materials* **2012,** *24* (17), 2320-2325.

151. van der Zande, A. M.; Huang, P. Y.; Chenet, D. A.; Berkelbach, T. C.; You, Y.; Lee, G.-H.; Heinz, T. F.; Reichman, D. R.; Muller, D. A.; Hone, J. C., Grains and grain boundaries in highly crystalline monolayer molybdenum disulphide. *Nature Materials* **2013,** *12*, 554.

152. Najmaei, S.; Liu, Z.; Zhou, W.; Zou, X.; Shi, G.; Lei, S.; Yakobson, B. I.; Idrobo, J.-C.; Ajayan, P. M.; Lou, J., Vapour phase growth and grain boundary structure of molybdenum disulphide atomic layers. *Nature Materials* **2013,** *12*, 754.

153. Kang, K.; Xie, S.; Huang, L.; Han, Y.; Huang, P. Y.; Mak, K. F.; Kim, C.-J.; Muller, D.; Park, J., High-mobility three-atom-thick semiconducting films with wafer-scale homogeneity. *Nature* **2015,** *520*, 656.

154. Lee, C.-H.; Lee, G.-H.; van der Zande, A. M.; Chen, W.; Li, Y.; Han, M.; Cui, X.; Arefe, G.; Nuckolls, C.; Heinz, T. F.; Guo, J.; Hone, J.; Kim, P., Atomically thin p–n junctions with van der Waals heterointerfaces. *Nature Nanotechnology* **2014,** *9*, 676.

155. Geim, A. K.; Grigorieva, I. V., Van der Waals heterostructures. *Nature* **2013,** *499*, 419.

156. Novoselov, K. S.; Mishchenko, A.; Carvalho, A.; Castro Neto, A. H., 2D materials and van der Waals heterostructures. *Science* **2016,** *353* (6298).

157. Calman, E. V.; Dorow, C. J.; Fogler, M. M.; Butov, L. V.; Hu, S.; Mishchenko, A.; Geim, A. K., Control of excitons in multi-layer van der Waals heterostructures. *Applied Physics Letters* **2016,** *108* (10), 101901.

158. Chao, L.; Peng, Z.; David Wei, Z., Devices and applications of van der Waals heterostructures. *Journal of Semiconductors* **2017,** *38* (3), 031005.

159. Shi, Y.; Zhou, W.; Lu, A.-Y.; Fang, W.; Lee, Y.-H.; Hsu, A. L.; Kim, S. M.; Kim, K. K.; Yang, H. Y.; Li, L.-J.; Idrobo, J.-C.; Kong, J., van der Waals Epitaxy of MoS2 Layers Using Graphene As Growth Templates. *Nano Letters* **2012,** *12* (6), 2784-2791.

160. Li, X.; Lin, M.-W.; Lin, J.; Huang, B.; Puretzky, A. A.; Ma, C.; Wang, K.; Zhou, W.; Pantelides, S. T.; Chi, M.; Kravchenko, I.; Fowlkes, J.; Rouleau, C. M.; Geohegan, D. B.; Xiao, K., Two-dimensional GaSe/$MoSe_2$ misfit bilayer heterojunctions by van der Waals epitaxy. *Science Advances* **2016,** *2* (4).

161. Ben Aziza, Z.; Henck, H.; Pierucci, D.; Silly, M. G.; Lhuillier, E.; Patriarche, G.; Sirotti, F.; Eddrief, M.; Ouerghi, A., van der Waals Epitaxy of GaSe/Graphene Heterostructure: Electronic and Interfacial Properties. *ACS Nano* **2016,** *10* (10), 9679-9686.

162. Yuan, X.; Tang, L.; Liu, S.; Wang, P.; Chen, Z.; Zhang, C.; Liu, Y.; Wang, W.; Zou, Y.; Liu, C.; Guo, N.; Zou, J.; Zhou, P.; Hu, W.; Xiu, F., Arrayed van der Waals Vertical Heterostructures Based on 2D GaSe Grown by Molecular Beam Epitaxy. *Nano Letters* **2015,** *15* (5), 3571-3577.

163. Yang, T.; Zheng, B.; Wang, Z.; Xu, T.; Pan, C.; Zou, J.; Zhang, X.; Qi, Z.; Liu, H.; Feng, Y.; Hu, W.; Miao, F.; Sun, L.; Duan, X.; Pan, A., Van der Waals epitaxial growth and optoelectronics of large-scale WSe_2/SnS_2 vertical bilayer p–n junctions. *Nature Communications* **2017,** *8* (1), 1906.

164. Fu, D.; Zhao, X.; Zhang, Y.-Y.; Li, L.; Xu, H.; Jang, A. R.; Yoon, S. I.; Song, P.; Poh, S. M.; Ren, T.; Ding, Z.; Fu, W.; Shin, T. J.; Shin, H. S.; Pantelides, S. T.; Zhou, W.; Loh, K. P., Molecular Beam Epitaxy of Highly Crystalline Monolayer Molybdenum Disulfide on Hexagonal Boron Nitride. *Journal of the American Chemical Society* **2017,** *139* (27), 9392-9400.

165. Song, J.-G.; Park, J.; Lee, W.; Choi, T.; Jung, H.; Lee, C. W.; Hwang, S.-H.; Myoung, J. M.; Jung, J.-H.; Kim, S.-H.; Lansalot-Matras, C.; Kim, H., Layer-Controlled, Wafer-Scale, and Conformal Synthesis of Tungsten Disulfide Nanosheets Using Atomic Layer Deposition. *ACS Nano* **2013,** *7* (12), 11333-11340.

166. Tan, L. K.; Liu, B.; Teng, J. H.; Guo, S.; Low, H. Y.; Loh, K. P., Atomic layer deposition of a MoS2 film. *Nanoscale* **2014,** *6* (18), 10584-10588.

167. Liu, H., Recent Progress in Atomic Layer Deposition of Multifunctional Oxides and Two-Dimensional Transition Metal Dichalcogenides. *Journal of Molecular and Engineering Materials* **2016,** *04* (04), 1640010.

168. Valdivia, A.; Tweet, D. J.; Jr., J. F. C., Atomic layer deposition of two dimensional MoS2 on 150 mm substrates. *Journal of Vacuum Science & Technology A: Vacuum, Surfaces, and Films* **2016,** *34* (2), 021515.

169. Jurca, T.; Moody, M. J.; Henning, A.; Emery, J. D.; Wang, B.; Tan, J. M.; Lohr, T. L.; Lauhon, L. J.; Marks, T. J., Low-Temperature Atomic Layer Deposition of MoS_2 Films. *Angewandte Chemie International Edition* **2017,** *56* (18), 4991-4995.

170. Bennig, G. K., Atomic force microscope and method for imaging surfaces with atomic resolution. Google Patents: 1988.

171. Binnig, G.; Rohrer, H.; Gerber, C.; Weibel, E., 7 x 7 Reconstruction on Si(111) Resolved in Real Space. *Physical Review Letters* **1983,** *50* (2), 120-123.

172. Rugar, D.; Hansma, P., Atomic force microscopy. *Physics today* **1990,** *43* (10), 23-30.

173. Meyer, E., Atomic force microscopy. *Progress in Surface Science* **1992,** *41* (1), 3-49.

174. Lennard-Jones, J. E., On the determination of molecular fields. —II. From the equation of state of a gas. *Proceedings of the Royal Society of London. Series A* **1924,** *106* (738), 463-477.

175. James, P. J.; Antognozzi, M.; Tamayo, J.; McMaster, T. J.; Newton, J. M.; Miles, M. J., Interpretation of Contrast in Tapping Mode AFM and Shear Force Microscopy. A Study of Nafion. *Langmuir* **2001,** *17* (2), 349-360.

176. Ye, Z.; Zhao, X., Phase imaging atomic force microscopy in the characterization of biomaterials. *Journal of Microscopy* **2010,** *238* (1), 27-35.

177. Houmadi, S.; Rodriguez, R. D.; Longobardi, S.; Giardina, P.; Fauré, M. C.; Giocondo, M.; Lacaze, E., Self-Assembly of Hydrophobin Protein Rodlets Studied with Atomic Force Spectroscopy in Dynamic Mode. *Langmuir* **2012,** *28* (5), 2551-2557.

178. Rodriguez, R. D.; Lacaze, E.; Jupille, J., Probing the probe: AFM tip-profiling via nanotemplates to determine Hamaker constants from phase–distance curves. *Ultramicroscopy* **2012,** *121* (Supplement C), 25-30.

179. Smekal, A., Zur Quantentheorie der Dispersion. *Naturwissenschaften* **1923,** *11* (43), 873-875.

180. Raman, C. V.; Krishnan, K. S., A New Type of Secondary Radiation. *Nature* **1928,** *121*, 501.

181. Smith, E.; Dent, G., Introduction, Basic Theory and Principles. In *Modern Raman Spectroscopy – A Practical Approach*, John Wiley & Sons, Ltd: 2005; pp 1-21.

182. Loudon, R., The Raman effect in crystals. *Advances in Physics* **1964,** *13* (52), 423-482.

183. Zhang, H.; Ma, Y.; Wan, Y.; Rong, X.; Xie, Z.; Wang, W.; Dai, L., Measuring the Refractive Index of Highly Crystalline Monolayer MoS2 with High Confidence. *Scientific Reports* **2015,** *5*, 8440.

184. Thomsen, C.; Reich, S.; Maultzsch, J., Raman Scattering. In *Carbon Nanotubes*, Wiley-VCH Verlag GmbH: 2007; pp 115-133.

185. Tuinstra, F.; Koenig, J. L., Raman Spectrum of Graphite. *The Journal of Chemical Physics* **1970,** *53* (3), 1126-1130.

186. Long, D. A., Classical Theory of Rayleigh and Raman Scattering. In *The Raman Effect*, John Wiley & Sons, Ltd: 2002; pp 31-48.

187. Long, D. A., Quantum Mechanical Theory of Rayleigh and Raman Scattering. In *The Raman Effect*, John Wiley & Sons, Ltd: 2002; pp 49-84.

188. Smith, E.; Dent, G., The Theory of Raman Spectroscopy. In *Modern Raman Spectroscopy – A Practical Approach*, John Wiley & Sons, Ltd: 2005; pp 71-92.

189. YU, P.; Cardona, M., *Fundamentals of Semiconductors: Physics and Materials Properties*. Springer Berlin Heidelberg: 2010.

190. Loudon, R., Theory of the resonance Raman effect in crystals. *J. Phys. France* **1965,** *26* (11), 677-683.

191. Zrimsek, A. B.; Chiang, N.; Mattei, M.; Zaleski, S.; McAnally, M. O.; Chapman, C. T.; Henry, A.-I.; Schatz, G. C.; Van Duyne, R. P., Single-Molecule Chemistry with Surface- and Tip-Enhanced Raman Spectroscopy. *Chemical Reviews* **2017,** *117* (11), 7583-7613.

192. Wessel, J., Surface-enhanced optical microscopy. *J. Opt. Soc. Am. B* **1985,** *2* (9), 1538-1541.

193. Mauser, N.; Hartschuh, A., Tip-enhanced near-field optical microscopy. *Chemical Society Reviews* **2014,** *43* (4), 1248-1262.

194. Claesson, P. M.; van der Wal, A.; Fogden, A., 8 - New Techniques for Optimization of Particulate Cleaning A2 - Johansson, Ingegärd. In *Handbook for Cleaning/Decontamination of Surfaces*, Somasundaran, P., Ed. Elsevier Science B.V.: Amsterdam, 2007; pp 885-927.

195. Drapak, S. I.; Gavrylyuk, S. V.; Kovalyuk, Z. D.; Lytvyn, O. S., Native oxide emerging of the cleavage surface of gallium selenide due to prolonged storage. *Semiconductors* **2008,** *42* (4), 414-421.

196. Balitskii, O.; Savchyn, V.; Yukhymchuk, V., Raman investigation of InSe and GaSe single-crystals oxidation. *Semiconductor science and technology* **2002,** *17* (2), L1.

197. Pozo-Zamudio, O. D. S., S.; Sich, M.; Akimov, I. A.; Bayer, M.; Schofield, R. C.; Chekhovich, E. A.; Robinson, B. J.; Kay, N. D.; Kolosov, O. V.; Dmitriev, A. I.; Lashkarev, G. V.; Borisenko, D. N.; Kolesnikov, N. N.; Tartakovskii, A. I. , Photoluminescence and Raman investigation of stability of InSe and GaSe thin films. *arXiv:1506.05619* **2015**.

198. Beechem, T. E.; Kowalski, B. M.; Brumbach, M. T.; McDonald, A. E.; Spataru, C. D.; Howell, S. W.; Ohta, T.; Pask, J. A.; Kalugin, N. G., Oxidation of ultrathin GaSe. *Applied Physics Letters* **2015,** *107* (17), 173103.

199. Alaric Bergeron, J. I., Richard Leonelli, Sébastien Francoeur, *arXiv:1612.06907*.

200. Rodriguez, R. D.; Müller, S.; Sheremet, E.; Zahn, D. R.; Villabona, A.; Lopez-Rivera, S. A.; Tonndorf, P.; de Vasconcellos, S. M.; Bratschitsch, R., Selective Raman modes and strong photoluminescence of gallium selenide flakes on sp2 carbon. *Journal of Vacuum Science & Technology B* **2014,** *32* (4), 04E106.

201. Märkl, A.; von der Emde, M.; Nowak, C.; Richter, W.; Zahn, D. R. T., Investigation of Se capping of epitaxial Ga2Se3 layers. *Surface Science* **1995,** *331*, 631-635.

202. Akira, Y.; Nobuaki, K.; Kiyoshi, T.; Tamotsu, O.; Makoto, K., Raman Study of Epitaxial Ga 2 Se 3 Films Grown by Molecular Beam Epitaxy. *Japanese Journal of Applied Physics* **1992,** *31* (2B), L186.

203. Carroll, P. J.; Lannin, J. S., Raman Scattering of amorphous selenium films. *Solid State Communications* **1981,** *40* (1), 81-84.

204. Lucovsky, G.; Mooradian, A.; Taylor, W.; Wright, G. B.; Keezer, R. C., Identification of the fundamental vibrational modes of trigonal, α - monoclinic and amorphous selenium. *Solid State Communications* **1967,** *5* (2), 113-117.

205. Benkhedir, M. L.; Brinza, M.; Adriaenssens, G. J., Electronic density of states in amorphous selenium. *Journal of Physics: Condensed Matter* **2004,** *16* (44), S5253.

206. Chaudhuri, S.; Biswas, S. K.; Choudhury, A.; Goswami, K., Variation of optical gap of thick amorphous selenium film on heat treatment. *Journal of Non-Crystalline Solids* **1983,** *54* (1), 179-182.

207. Lukács, R.; Veres, M.; Shimakawa, K.; Kugler, S., On photoinduced volume change in amorphous selenium: Quantum chemical calculation and Raman spectroscopy. *Journal of Applied Physics* **2010,** *107* (7), 073517.

208. Wang, G.; Pandey, R.; Karna, S. P., Physics and chemistry of oxidation of two-dimensional nanomaterials by molecular oxygen. *Wiley Interdisciplinary Reviews: Computational Molecular Science* **2017,** *7* (1), e1280-n/a.

209. Kang, Y.; Najmaei, S.; Liu, Z.; Bao, Y.; Wang, Y.; Zhu, X.; Halas, N. J.; Nordlander, P.; Ajayan, P. M.; Lou, J.; Fang, Z., Plasmonic Hot Electron Induced Structural Phase Transition in a MoS2 Monolayer. *Advanced Materials* **2014,** *26* (37), 6467-6471.

210. Gao, J.; Li, B.; Tan, J.; Chow, P.; Lu, T.-M.; Koratkar, N., Aging of Transition Metal Dichalcogenide Monolayers. *ACS Nano* **2016,** *10* (2), 2628-2635.

211. Tsai, M.-L.; Su, S.-H.; Chang, J.-K.; Tsai, D.-S.; Chen, C.-H.; Wu, C.-I.; Li, L.-J.; Chen, L.-J.; He, J.-H., Monolayer MoS2 Heterojunction Solar Cells. *ACS Nano* **2014,** *8* (8), 8317-8322.

212. Xiao, D.; Liu, G.-B.; Feng, W.; Xu, X.; Yao, W., Coupled Spin and Valley Physics in Monolayers of MoS_2 and Other Group-VI Dichalcogenides. *Physical Review Letters* **2012,** *108* (19), 196802.

213. Mak, K. F.; He, K.; Shan, J.; Heinz, T. F., Control of valley polarization in monolayer MoS2 by optical helicity. *Nat Nano* **2012,** *7* (8), 494-498.

214. Wang, W.; Narayan, A.; Tang, L.; Dolui, K.; Liu, Y.; Yuan, X.; Jin, Y.; Wu, Y.; Rungger, I.; Sanvito, S.; Xiu, F., Spin-Valve Effect in NiFe/MoS_2/NiFe Junctions. *Nano Letters* **2015,** *15* (8), 5261-5267.

215. Wu, W.; Wang, L.; Li, Y.; Zhang, F.; Lin, L.; Niu, S.; Chenet, D.; Zhang, X.; Hao, Y.; Heinz, T. F.; Hone, J.; Wang, Z. L., Piezoelectricity of single-atomic-layer MoS_2 for energy conversion and piezotronics. *Nature* **2014,** *514* (7523), 470-474.

216. Ye, Y.; Wong, Z. J.; Lu, X.; Ni, X.; Zhu, H.; Chen, X.; Wang, Y.; Zhang, X., Monolayer excitonic laser. *Nat Photon* **2015,** *9* (11), 733-737.

217. Xu, X.; Yao, W.; Xiao, D.; Heinz, T. F., Spin and pseudospins in layered transition metal dichalcogenides. *Nat Phys* **2014,** *10* (5), 343-350.

218. Poellmann, C.; Steinleitner, P.; Leierseder, U.; Nagler, P.; Plechinger, G.; Porer, M.; Bratschitsch, R.; Schuller, C.; Korn, T.; Huber, R., Resonant internal quantum transitions and femtosecond radiative decay of excitons in monolayer WSe_2. *Nat Mater* **2015,** *14* (9), 889-893.

219. Cao, T.; Wang, G.; Han, W.; Ye, H.; Zhu, C.; Shi, J.; Niu, Q.; Tan, P.; Wang, E.; Liu, B.; Feng, J., Valley-selective circular dichroism of monolayer molybdenum disulphide. *Nature Communications* **2012,** *3*, 887.

220. Plechinger, G.; Nagler, P.; Kraus, J.; Paradiso, N.; Strunk, C.; Schüller, C.; Korn, T., Identification of excitons, trions and biexcitons in single-layer WS_2. *physica status solidi (RRL) – Rapid Research Letters* **2015,** *9* (8), 457-461.

221. Weismann, M.; Panoiu, N. C., Theoretical and computational analysis of second- and third-harmonic generation in periodically patterned graphene and transition-metal dichalcogenide monolayers. *Physical Review B* **2016,** *94* (3), 035435.

222. Wang, G.; Marie, X.; Gerber, I.; Amand, T.; Lagarde, D.; Bouet, L.; Vidal, M.; Balocchi, A.; Urbaszek, B., Giant Enhancement of the Optical Second-Harmonic Emission of WSe_2 Monolayers by Laser Excitation at Exciton Resonances. *Physical Review Letters* **2015,** *114* (9), 097403.

223. Dybała, F.; Polak, M. P.; Kopaczek, J.; Scharoch, P.; Wu, K.; Tongay, S.; Kudrawiec, R., Pressure coefficients for direct optical transitions in MoS_2, $MoSe_2$, WS_2, and WSe_2 crystals and semiconductor to metal transitions. *Scientific Reports* **2016,** *6*, 26663.

224. Bhattacharyya, S.; Singh, A. K., Semiconductor-metal transition in semiconducting bilayer sheets of transition-metal dichalcogenides. *Physical Review B* **2012,** *86* (7), 075454.

225. Nguyen, C. V.; Hieu, N. N.; Ilyasov, V. V., Band Gap Modulation of Bilayer MoS_2 Under Strain Engineering and Electric Field: A Density Functional Theory. *Journal of Electronic Materials* **2016,** *45* (8), 4038-4043.

226. Yue, Q.; Kang, J.; Shao, Z.; Zhang, X.; Chang, S.; Wang, G.; Qin, S.; Li, J., Mechanical and electronic properties of monolayer MoS_2 under elastic strain. *Physics Letters A* **2012,** *376* (12–13), 1166-1170.

227. Ghorbani-Asl, M.; Borini, S.; Kuc, A.; Heine, T., Strain-dependent modulation of conductivity in single-layer transition-metal dichalcogenides. *Physical Review B* **2013,** *87* (23), 235434.

228. He, K.; Poole, C.; Mak, K. F.; Shan, J., Experimental Demonstration of Continuous Electronic Structure Tuning via Strain in Atomically Thin MoS_2. *Nano Letters* **2013,** *13* (6), 2931-2936.

229. Conley, H. J.; Wang, B.; Ziegler, J. I.; Haglund, R. F.; Pantelides, S. T.; Bolotin, K. I., Bandgap Engineering of Strained Monolayer and Bilayer MoS_2. *Nano Letters* **2013,** *13* (8), 3626-3630.

230. Scalise, E.; Houssa, M.; Pourtois, G.; Afanas'ev, V.; Stesmans, A., Strain-induced semiconductor to metal transition in the two-dimensional honeycomb structure of MoS_2. *Nano Research* **2012,** *5* (1), 43-48.

231. Plechinger, G.; Castellanos-Gomez, A.; Buscema, M.; S. J. van der Zant, H.; A. Steele, G.; Kuc, A.; Heine, T.; Schüller, C.; Korn, T., Control of biaxial strain in single-layer molybdenite using local thermal expansion of the substrate. *2D Materials* **2015,** *2* (1), 015006.

232. Peña-Álvarez, M.; del Corro, E.; Morales-García, Á.; Kavan, L.; Kalbac, M.; Frank, O., Single Layer Molybdenum Disulfide under Direct Out-of-Plane Compression: Low-Stress Band-Gap Engineering. *Nano Letters* **2015,** *15* (5), 3139-3146.

233. Hui, Y. Y.; Liu, X.; Jie, W.; Chan, N. Y.; Hao, J.; Hsu, Y.-T.; Li, L.-J.; Guo, W.; Lau, S. P., Exceptional Tunability of Band Energy in a Compressively Strained Trilayer MoS2 Sheet. *ACS Nano* **2013,** *7* (8), 7126-7131.

234. McCreary, A.; Ghosh, R.; Amani, M.; Wang, J.; Duerloo, K.-A. N.; Sharma, A.; Jarvis, K.; Reed, E. J.; Dongare, A. M.; Banerjee, S. K.; Terrones, M.; Namburu, R. R.; Dubey, M., Effects of Uniaxial and Biaxial Strain on Few-Layered Terrace Structures of MoS2 Grown by Vapor Transport. *ACS Nano* **2016,** *10* (3), 3186-3197.

235. López-Suárez, M.; Neri, I.; Rurali, R., Band gap engineering of MoS_2 upon compression. *Journal of Applied Physics* **2016,** *119* (16), 165105.

236. Castellanos-Gomez, A.; Roldán, R.; Cappelluti, E.; Buscema, M.; Guinea, F.; van der Zant, H. S. J.; Steele, G. A., Local Strain Engineering in Atomically Thin MoS_2. *Nano Letters* **2013,** *13* (11), 5361-5366.

237. Kern, J.; Niehues, I.; Tonndorf, P.; Schmidt, R.; Wigger, D.; Schneider, R.; Stiehm, T.; Michaelis de Vasconcellos, S.; Reiter, D. E.; Kuhn, T.; Bratschitsch, R., Nanoscale Positioning of Single-Photon Emitters in Atomically Thin WSe_2. *Advanced Materials* **2016,** *28* (33), 7101-7105.

238. Bertolazzi, S.; Brivio, J.; Kis, A., Stretching and Breaking of Ultrathin MoS_2. *ACS Nano* **2011,** *5* (12), 9703-9709.

239. Brunner, K.; Abstreiter, G.; Kolbesen, B. O.; Meul, H. W., Strain at Si□SiO2 interfaces studied by Micron-Raman spectroscopy. *Applied Surface Science* **1989,** *39* (1), 116-126.

240. Mohiuddin, T. M. G.; Lombardo, A.; Nair, R. R.; Bonetti, A.; Savini, G.; Jalil, R.; Bonini, N.; Basko, D. M.; Galiotis, C.; Marzari, N.; Novoselov, K. S.; Geim, A. K.; Ferrari, A. C., Uniaxial strain in graphene by Raman spectroscopy: G peak splitting, Gr\"uneisen parameters, and sample orientation. *Physical Review B* **2009,** *79* (20), 205433.

241. Jiang, N.; Kurouski, D.; Pozzi, E. A.; Chiang, N.; Hersam, M. C.; Van Duyne, R. P., Tip-enhanced Raman spectroscopy: From concepts to practical applications. *Chemical Physics Letters* **2016,** *659*, 16-24.

242. Zhong, J.-H.; Jin, X.; Meng, L.; Wang, X.; Su, H.-S.; Yang, Z.-L.; Williams, C. T.; Ren, B., Probing the electronic and catalytic properties of a bimetallic surface with 3 nm resolution. *Nat Nano* **2017,** *12* (2), 132-136.

243. Chen, C.; Hayazawa, N.; Kawata, S., A 1.7 nm resolution chemical analysis of carbon nanotubes by tip-enhanced Raman imaging in the ambient. *Nature Communications* **2014,** *5*, 3312.

244. Sheremet, E.; Rodriguez, R. D.; Agapov, A. L.; Sokolov, A. P.; Hietschold, M.; Zahn, D. R. T., Nanoscale imaging and identification of a four-component carbon sample. *Carbon* **2016,** *96*, 588-593.

245. Shiotari, A.; Kumagai, T.; Wolf, M., Tip-Enhanced Raman Spectroscopy of Graphene Nanoribbons on Au(111). *The Journal of Physical Chemistry C* **2014,** *118* (22), 11806-11812.

246. Stadler, J.; Schmid, T.; Zenobi, R., Nanoscale chemical imaging of single-layer graphene. *ACS Nano* **2011,** *5*.

247. Hayazawa, N.; Motohashi, M.; Saito, Y.; Ishitobi, H.; Ono, A.; Ichimura, T.; Verma, P.; Kawata, S., Visualization of localized strain of a crystalline thin layer at the nanoscale by tip-enhanced Raman spectroscopy and microscopy. *Journal of Raman Spectroscopy* **2007,** *38* (6), 684-696.

248. Zhang, Y.; Voronine, D. V.; Qiu, S.; Sinyukov, A. M.; Hamilton, M.; Liege, Z.; Sokolov, A. V.; Zhang, Z.; Scully, M. O., Improving resolution in quantum subnanometre-gap tip-enhanced Raman nanoimaging. *Scientific Reports* **2016,** *6*, 25788.

249. Su, W.; Kumar, N.; Mignuzzi, S.; Crain, J.; Roy, D., Nanoscale mapping of excitonic processes in single-layer MoS2 using tip-enhanced photoluminescence microscopy. *Nanoscale* **2016,** *8* (20), 10564-10569.

250. Park, K.-D.; Khatib, O.; Kravtsov, V.; Clark, G.; Xu, X.; Raschke, M. B., Hybrid Tip-Enhanced Nanospectroscopy and Nanoimaging of Monolayer WSe2 with Local Strain Control. *Nano Letters* **2016,** *16* (4), 2621-2627.

251. Fleischmann, M.; Hendra, P. J.; McQuillan, A. J., Raman spectra of pyridine adsorbed at a silver electrode. *Chemical Physics Letters* **1974,** *26* (2), 163-166.

252. Jeanmaire, D. L.; Van Duyne, R. P., Surface raman spectroelectrochemistry. *Journal of Electroanalytical Chemistry and Interfacial Electrochemistry* **1977,** *84* (1), 1-20.

253. Nie, S.; Emory, S. R., Probing Single Molecules and Single Nanoparticles by Surface-Enhanced Raman Scattering. *Science* **1997,** *275* (5303), 1102.

254. Kneipp, K.; Wang, Y.; Kneipp, H.; Perelman, L. T.; Itzkan, I.; Dasari, R. R.; Feld, M. S., Single Molecule Detection Using Surface-Enhanced Raman Scattering (SERS). *Physical Review Letters* **1997,** *78* (9), 1667-1670.

255. Schlücker, S., Surface-Enhanced Raman Spectroscopy: Concepts and Chemical Applications. *Angewandte Chemie International Edition* **2014,** *53* (19), 4756-4795.

256. Stöckle, R. M.; Suh, Y. D.; Deckert, V.; Zenobi, R., Nanoscale chemical analysis by tip-enhanced Raman spectroscopy. *Chemical Physics Letters* **2000,** *318* (1–3), 131-136.

257. Johnson, P. B.; Christy, R. W., Optical Constants of the Noble Metals. *Physical Review B* **1972,** *6* (12), 4370-4379.

258. Richard-Lacroix, M.; Zhang, Y.; Dong, Z.; Deckert, V., Mastering high resolution tip-enhanced Raman spectroscopy: towards a shift of perception. *Chemical Society Reviews* **2017,** *46* (13), 3922-3944.

259. Novotny, L.; Hecht, B., *Principles of Nano-Optics*. Cambridge University Press: Cambridge, 2006.

260. Gunnarsson, L.; Bjerneld, E. J.; Xu, H.; Petronis, S.; Kasemo, B.; Käll, M., Interparticle coupling effects in nanofabricated substrates for surface-enhanced Raman scattering. *Applied Physics Letters* **2001,** *78* (6), 802-804.

261. Sattler, K. D., *Handbook of Nanophysics: Nanoparticles and Quantum Dots*. ed.; CRC press: Vol. 3.

262. Esteban, R.; Borisov, A. G.; Nordlander, P.; Aizpurua, J., Bridging quantum and classical plasmonics with a quantum-corrected model. *Nature Communications* **2012,** *3*, 825.

263. Savage, K. J.; Hawkeye, M. M.; Esteban, R.; Borisov, A. G.; Aizpurua, J.; Baumberg, J. J., Revealing the quantum regime in tunnelling plasmonics. *Nature* **2012,** *491*, 574.

264. Zhu, W.; Esteban, R.; Borisov, A. G.; Baumberg, J. J.; Nordlander, P.; Lezec, H. J.; Aizpurua, J.; Crozier, K. B., Quantum mechanical effects in plasmonic structures with subnanometre gaps. *Nature Communications* **2016,** *7*, 11495.

265. Vogel, N.; Goerres, S.; Landfester, K.; Weiss, C. K., A Convenient Method to Produce Close- and Non-close-Packed Monolayers using Direct Assembly at the Air–Water Interface and Subsequent Plasma-Induced Size Reduction. *Macromolecular Chemistry and Physics* **2011,** *212* (16), 1719-1734.

266. Castellanos-Gomez, A.; Buscema, M.; Molenaar, R.; Singh, V.; Janssen, L.; S. J. van der Zant, H.; A. Steele, G., Deterministic transfer of two-dimensional materials by all-dry viscoelastic stamping. *2D Materials* **2014,** *1* (1), 011002.

267. Chakraborty, B.; Matte, H. S. S. R.; Sood, A. K.; Rao, C. N. R., Layer-dependent resonant Raman scattering of a few layer MoS_2. *Journal of Raman Spectroscopy* **2013,** *44* (1), 92-96.

268. Lee, C.; Yan, H.; Brus, L. E.; Heinz, T. F.; Hone, J.; Ryu, S., Anomalous Lattice Vibrations of Single- and Few-Layer MoS_2. *ACS Nano* **2010,** *4* (5), 2695-2700.

269. Kumar, N.; Mignuzzi, S.; Su, W.; Roy, D., Tip-enhanced Raman spectroscopy: principles and applications. *EPJ Techniques and Instrumentation* **2015,** *2* (1), 9.

270. Kim, D.-S.; Kim, Z. H., Role of in-plane polarizability of the tip in scattering near-field microscopy of a plasmonic nanoparticle. *Opt. Express* **2012,** *20* (8), 8689-8699.

271. Beal, A. R.; Hughes, H. P., Kramers-Kronig analysis of the reflectivity spectra of 2H-MoS_2 , 2H-$MoSe_2$ and 2H-$MoTe_2$. *Journal of Physics C: Solid State Physics* **1979,** *12* (5), 881.

272. Gołasa, K.; Grzeszczyk, M.; Leszczyński, P.; Faugeras, C.; Nicolet, A. A. L.; Wysmołek, A.; Potemski, M.; Babiński, A., Multiphonon resonant Raman scattering in MoS2. *Applied Physics Letters* **2014,** *104* (9), 092106.

273. Molina-Sánchez, A.; Wirtz, L., Phonons in single-layer and few-layer MoS_2 and WS_2. *Physical Review B* **2011,** *84* (15), 155413.

274. Verble, J. L.; Wieting, T. J., Lattice Mode Degeneracy in MoS_2 and Other Layer Compounds. *Physical Review Letters* **1970,** *25* (6), 362-365.

275. Tomoyuki Sekine, K. U., ; Tsuneo Nakashizu,; Etsuyuki Matsuura,; Ryozo Yoshizaki, Dispersive Raman Mode of Layered Compound 2H-MoS_2 under the Resonant Condition. *Journal of the Physical Society of Japan* **1984,** *53* (2), 811-818.

276. Pimenta, M. A.; del Corro, E.; Carvalho, B. R.; Fantini, C.; Malard, L. M., Comparative Study of Raman Spectroscopy in Graphene and MoS_2-type Transition Metal Dichalcogenides. *Accounts of Chemical Research* **2015,** *48* (1), 41-47.

277. Frey, G. L.; Tenne, R.; Matthews, M. J.; Dresselhaus, M. S.; Dresselhaus, G., Raman and resonance Raman investigation of MoS_2 nanoparticles. *Physical Review B* **1999,** *60* (4), 2883-2892.

278. Chakraborty, B.; Bera, A.; Muthu, D. V. S.; Bhowmick, S.; Waghmare, U. V.; Sood, A. K., Symmetry-dependent phonon renormalization in monolayer MoS_2 transistor. *Physical Review B* **2012,** *85* (16), 161403.

279. Buscema, M.; Steele, G. A.; van der Zant, H. S. J.; Castellanos-Gomez, A., The effect of the substrate on the Raman and photoluminescence emission of single-layer MoS_2. *Nano Research* **2014,** *7* (4), 561-571.

280. Gwyddion http://gwyddion.net.

281. Balois, M. V.; Hayazawa, N.; Catalan, F. C.; Kawata, S.; Yano, T.-a.; Hayashi, T., Tip-enhanced THz Raman spectroscopy for local temperature determination at the nanoscale. *Analytical and Bioanalytical Chemistry* **2015,** *407* (27), 8205-8213.

282. Milekhin, A. G.; Rahaman, M.; Rodyakina, E. E.; Latyshev, A. V.; Dzhagan, V. M.; Zahn, D. R. T., Giant gap-plasmon tip-enhanced Raman scattering of MoS_2 monolayers on Au nanocluster arrays. *Nanoscale* **2018**.

283. Downes, A.; Salter, D.; Elfick, A., Heating effects in tip-enhanced optical microscopy. *Opt. Express* **2006,** *14* (12), 5216-5222.

284. Menéndez, J.; Cardona, M., Temperature dependence of the first-order Raman scattering by phonons in Si, Ge, and α-Sn: Anharmonic effects. *Physical Review B* **1984,** *29* (4), 2051-2059.

285. Hart, T. R.; Aggarwal, R. L.; Lax, B., Temperature Dependence of Raman Scattering in Silicon. *Physical Review B* **1970,** *1* (2), 638-642.

286. Li, X.; Li, J.; Wang, K.; Wang, X.; Wang, S.; Chu, X.; Xu, M.; Fang, X.; Wei, Z.; Zhai, Y.; Zou, B., Pressure and temperature-dependent Raman spectra of MoS_2 film. *Applied Physics Letters* **2016,** *109* (24), 242101.

287. Yan, R.; Simpson, J. R.; Bertolazzi, S.; Brivio, J.; Watson, M.; Wu, X.; Kis, A.; Luo, T.; Hight Walker, A. R.; Xing, H. G., Thermal Conductivity of Monolayer Molybdenum Disulfide Obtained from Temperature-Dependent Raman Spectroscopy. *ACS Nano* **2014,** *8* (1), 986-993.

288. Thripuranthaka, M.; Kashid, R. V.; Rout, C. S.; Late, D. J., Temperature dependent Raman spectroscopy of chemically derived few layer MoS_2 and WS_2 nanosheets. *Applied Physics Letters* **2014,** *104* (8), 081911.

289. Sahoo, S.; Gaur, A. P. S.; Ahmadi, M.; Guinel, M. J. F.; Katiyar, R. S., Temperature-Dependent Raman Studies and Thermal Conductivity of Few-Layer MoS_2. *The Journal of Physical Chemistry C* **2013,** *117* (17), 9042-9047.

290. Lanzillo, N. A.; Birdwell, A. G.; Amani, M.; Crowne, F. J.; Shah, P. B.; Najmaei, S.; Liu, Z.; Ajayan, P. M.; Lou, J.; Dubey, M.; Nayak, S. K.; O'Regan, T. P., Temperature-dependent phonon shifts in monolayer MoS_2. *Applied Physics Letters* **2013,** *103* (9), 093102.

291. Brongersma, M. L., Plasmonic Photodetectors, Photovoltaics, and Hot-Electron Devices. *Proceedings of the IEEE* **2016,** *104* (12), 2349-2361.

292. Jiang, N.; Zhuo, X.; Wang, J., Active Plasmonics: Principles, Structures, and Applications. *Chemical Reviews* **2017**.

293. Chursanova, M. V.; Dzhagan, V. M.; Yukhymchuk, V. O.; Lytvyn, O. S.; Valakh, M. Y.; Khodasevich, I. A.; Lehmann, D.; Zahn, D. R. T.; Waurisch, C.; Hickey, S. G., Nanostructured Silver Substrates With Stable and Universal SERS Properties: Application to Organic Molecules and Semiconductor Nanoparticles. *Nanoscale Research Letters* **2009,** *5* (2), 403.

294. Halas, N. J.; Lal, S.; Chang, W.-S.; Link, S.; Nordlander, P., Plasmons in Strongly Coupled Metallic Nanostructures. *Chemical Reviews* **2011,** *111* (6), 3913-3961.

295. Pozzi, E. A.; Goubert, G.; Chiang, N.; Jiang, N.; Chapman, C. T.; McAnally, M. O.; Henry, A.-I.; Seideman, T.; Schatz, G. C.; Hersam, M. C.; Duyne, R. P. V., Ultrahigh-Vacuum Tip-Enhanced Raman Spectroscopy. *Chemical Reviews* **2017,** *117* (7), 4961-4982.

296. Deckert-Gaudig, T.; Deckert, V., Nanoscale structural analysis using tip-enhanced Raman spectroscopy. *Curr Opin Chem Biol* **2011,** *15* (5), 719-724.

297. Shi, X.; Coca-López, N.; Janik, J.; Hartschuh, A., Advances in Tip-Enhanced Near-Field Raman Microscopy Using Nanoantennas. *Chemical Reviews* **2017,** *117* (7), 4945-4960.

298. Stadler, J.; Schmid, T.; Zenobi, R., Developments in and practical guidelines for tip-enhanced Raman spectroscopy. *Nanoscale* **2012,** *4* (6), 1856-1870.

299. Neacsu, C. C.; Dreyer, J.; Behr, N.; Raschke, M. B., Scanning-probe Raman spectroscopy with single-molecule sensitivity. *Physical Review B* **2006,** *73* (19), 193406.

300. Zhang, W.; Yeo, B. S.; Schmid, T.; Zenobi, R., Single Molecule Tip-Enhanced Raman Spectroscopy with Silver Tips. *The Journal of Physical Chemistry C* **2007,** *111* (4), 1733-1738.

301. Deckert, V.; Deckert-Gaudig, T.; Diegel, M.; Gotz, I.; Langeluddecke, L.; Schneidewind, H.; Sharma, G.; Singh, P.; Singh, P.; Trautmann, S.; Zeisberger, M.; Zhang, Z., Spatial resolution in Raman spectroscopy. *Faraday Discussions* **2015,** *177* (0), 9-20.

302. Deckert-Gaudig, T.; Kämmer, E.; Deckert, V., Tracking of nanoscale structural variations on a single amyloid fibril with tip-enhanced Raman scattering. *Journal of Biophotonics* **2012,** *5* (3), 215-219.

303. Chen, C.; Hayazawa, N.; Kawata, S., A 1.7 nm resolution chemical analysis of carbon nanotubes by tip-enhanced Raman imaging in the ambient. **2014,** *5*, 3312.

304. Mehtani, D.; Lee, N.; Hartschuh, R. D.; Kisliuk, A.; Foster, M. D.; Sokolov, A. P.; Maguire, J. F., Nano-Raman spectroscopy with side-illumination optics. *Journal of Raman Spectroscopy* **2005,** *36* (11), 1068-1075.

305. Sun, W. X.; Shen, Z. X., Apertureless near-field scanning Raman microscopy using reflection scattering geometry. *Ultramicroscopy* **2003,** *94* (3), 237-244.

306. Tarun, A.; Hayazawa, N.; Motohashi, M.; Kawata, S., Highly efficient tip-enhanced Raman spectroscopy and microscopy of strained silicon. *Review of Scientific Instruments* **2008,** *79* (1), 013706.

307. Yoshikawa, M.; Murakami, M.; Ishida, H., Highly sensitive detection of near-field Raman scattered light from strained Si/SiGe heterostructures by scanning near-field optical Raman microscope using ultraviolet resonant Raman scattering. *Applied Physics Letters* **2008,** *92* (9), 091903.

308. Saito, Y.; Motohashi, M.; Hayazawa, N.; Iyoki, M.; Kawata, S., Nanoscale characterization of strained silicon by tip-enhanced Raman spectroscope in reflection mode. *Applied Physics Letters* **2006,** *88* (14), 143109.

309. Matsui, R.; Verma, P.; Ichimura, T.; Inouye, Y.; Kawata, S., Nanoanalysis of crystalline properties of GaN thin film using tip-enhanced Raman spectroscopy. *Applied Physics Letters* **2007,** *90* (6), 061906.

310. Kazemi-Zanjani, N.; Kergrene, E.; Liu, L.; Sham, T.-K.; Lagugné-Labarthet, F., Tip-Enhanced Raman Imaging and Nano Spectroscopy of Etched Silicon Nanowires. *Sensors* **2013,** *13* (10), 12744.

311. Hermann, P.; Hecker, M.; Chumakov, D.; Weisheit, M.; Rinderknecht, J.; Shelaev, A.; Dorozhkin, P.; Eng, L. M., Imaging and strain analysis of nano-scale SiGe structures by tip-enhanced Raman spectroscopy. *Ultramicroscopy* **2011,** *111* (11), 1630-1635.

312. Gucciardi, P. G.; Valmalette, J.-C., Different longitudinal optical—transverse optical mode amplification in tip enhanced Raman spectroscopy of GaAs(001). *Applied Physics Letters* **2010,** *97* (26), 263104.

313. Rodriguez, R. D.; Sheremet, E.; Deckert-Gaudig, T.; Chaneac, C.; Hietschold, M.; Deckert, V.; Zahn, D. R. T., Surface- and tip-enhanced Raman spectroscopy reveals spin-waves in iron oxide nanoparticles. *Nanoscale* **2015,** *7* (21), 9545-9551.

314. Sheremet, E.; Milekhin, A. G.; Rodriguez, R. D.; Weiss, T.; Nesterov, M.; Rodyakina, E. E.; Gordan, O. D.; Sveshnikova, L. L.; Duda, T. A.; Gridchin, V. A.; Dzhagan, V. M.; Hietschold, M.; Zahn, D. R. T., Surface- and tip-enhanced resonant Raman scattering from CdSe nanocrystals. *Physical Chemistry Chemical Physics* **2015,** *17* (33), 21198-21203.

315. Rahaman, M.; Rodriguez, R. D.; Plechinger, G.; Moras, S.; Schüller, C.; Korn, T.; Zahn, D. R. T., Highly Localized Strain in a MoS_2/Au Heterostructure Revealed by Tip-Enhanced Raman Spectroscopy. *Nano Letters* **2017,** *17* (10), 6027-6033.

316. Su, W.; Kumar, N.; Spencer, S. J.; Dai, N.; Roy, D., Transforming bilayer MoS2 into single-layer with strong photoluminescence using UV-ozone oxidation. *Nano Research* **2015,** *8* (12), 3878-3886.

317. Bao, W.; Borys, N. J.; Ko, C.; Suh, J.; Fan, W.; Thron, A.; Zhang, Y.; Buyanin, A.; Zhang, J.; Cabrini, S.; Ashby, P. D.; Weber-Bargioni, A.; Tongay, S.; Aloni, S.; Ogletree, D. F.; Wu, J.; Salmeron, M. B.; Schuck, P. J., Visualizing nanoscale excitonic relaxation properties of disordered edges and grain boundaries in monolayer molybdenum disulfide. *Nature Communications* **2015,** *6*, 7993.

318. C. Tang; S. Jia; W. Chen; J. Lou; Voronine, D. V., Nano-optical imaging of monolayer $MoSe_2$ using tip-enhanced photoluminescence *arXiv:1704.02396* **2017**.

319. Butun, S.; Tongay, S.; Aydin, K., Enhanced Light Emission from Large-Area Monolayer MoS_2 Using Plasmonic Nanodisc Arrays. *Nano Letters* **2015,** *15* (4), 2700-2704.

320. Li, J.; Ji, Q.; Chu, S.; Zhang, Y.; Li, Y.; Gong, Q.; Liu, K.; Shi, K., Tuning the photo-response in monolayer MoS2 by plasmonic nano-antenna. *Scientific Reports* **2016,** *6*, 23626.

321. Li, H.; Zhang, Q.; Yap, C. C. R.; Tay, B. K.; Edwin, T. H. T.; Olivier, A.; Baillargeat, D., From Bulk to Monolayer MoS2: Evolution of Raman Scattering. *Advanced Functional Materials* **2012,** *22* (7), 1385-1390.

322. Jiang, N.; Chiang, N.; Madison, L. R.; Pozzi, E. A.; Wasielewski, M. R.; Seideman, T.; Ratner, M. A.; Hersam, M. C.; Schatz, G. C.; Van Duyne, R. P., Nanoscale Chemical Imaging of a Dynamic Molecular Phase Boundary with Ultrahigh Vacuum Tip-Enhanced Raman Spectroscopy. *Nano Letters* **2016,** *16* (6), 3898-3904.

323. Neacsu, C. C.; Berweger, S.; Raschke, M. B., Tip-Enhanced Raman Imaging and Nanospectroscopy: Sensitivity, Symmetry, and Selection Rules. *NanoBiotechnology* **2007,** *3* (3), 172-196.

324. Hayazawa, N.; Yano, T.-a.; Kawata, S., Highly reproducible tip-enhanced Raman scattering using an oxidized and metallized silicon cantilever tip as a tool for everyone. *Journal of Raman Spectroscopy* **2012,** *43* (9), 1177-1182.

325. Wokaun, A.; Gordon, J. P.; Liao, P. F., Radiation Damping in Surface-Enhanced Raman Scattering. *Physical Review Letters* **1982,** *48* (14), 957-960.

326. Kolwas, K.; Derkachova, A., Damping rates of surface plasmons for particles of size from nano- to micrometers; reduction of the nonradiative decay. *Journal of Quantitative Spectroscopy and Radiative Transfer* **2013,** *114*, 45-55.

327. Meng, L.; Huang, T.; Wang, X.; Chen, S.; Yang, Z.; Ren, B., Gold-coated AFM tips for tip-enhanced Raman spectroscopy: theoretical calculation and experimental demonstration. *Opt. Express* **2015,** *23* (11), 13804-13813.

328. Yang, Z.; Aizpurua, J.; Xu, H., Electromagnetic field enhancement in TERS configurations. *Journal of Raman Spectroscopy* **2009,** *40* (10), 1343-1348.

329. Sekine, T.; Uchinokura, K.; Nakashizu, T.; Matsuura, E.; Yoshizaki, R., Dispersive Raman Mode of Layered Compound 2H-MoS2 under the Resonant Condition. *Journal of the Physical Society of Japan* **1984,** *53* (2), 811-818.

330. Liu, H.-L.; Guo, H.; Yang, T.; Zhang, Z.; Kumamoto, Y.; Shen, C.-C.; Hsu, Y.-T.; Li, L.-J.; Saito, R.; Kawata, S., Anomalous lattice vibrations of monolayer MoS_2 probed by ultraviolet Raman scattering. *Physical Chemistry Chemical Physics* **2015,** *17* (22), 14561-14568.

331. Yang, T.; Huang, X.; Zhou, H.; Wu, G.; Lai, T., Excitation mechanism of A1g mode and origin of nonlinear temperature dependence of Raman shift of CVD-grown mono- and few-layer MoS_2 films. *Opt. Express* **2016,** *24* (11), 12281-12292.

332. Yu, Y.; Ji, Z.; Zu, S.; Du, B.; Kang, Y.; Li, Z.; Zhou, Z.; Shi, K.; Fang, Z., Ultrafast Plasmonic Hot Electron Transfer in Au Nanoantenna/MoS_2 Heterostructures. *Advanced Functional Materials* **2016,** *26* (35), 6394-6401.

333. Najmaei, S.; Mlayah, A.; Arbouet, A.; Girard, C.; Léotin, J.; Lou, J., Plasmonic Pumping of Excitonic Photoluminescence in Hybrid MoS_2–Au Nanostructures. *ACS Nano* **2014,** *8* (12), 12682-12689.

334. Ayars, E. J.; Hallen, H. D.; Jahncke, C. L., Electric Field Gradient Effects in Raman Spectroscopy. *Physical Review Letters* **2000,** *85* (19), 4180-4183.

335. Meng, L.; Yang, Z.; Chen, J.; Sun, M., Effect of Electric Field Gradient on Sub-nanometer Spatial Resolution of Tip-enhanced Raman Spectroscopy. *Scientific Reports* **2015,** *5*, 9240.

336. Stiles, P. L.; Dieringer, J. A.; Shah, N. C.; Duyne, R. P. V., Surface-Enhanced Raman Spectroscopy. *Annual Review of Analytical Chemistry* **2008,** *1* (1), 601-626.

337. Meneses-Rodríguez, D.; Ferreiro-Vila, E.; Prieto, P.; Anguita, J.; González, M. U.; García-Martín, J. M.; Cebollada, A.; García-Martín, A.; Armelles, G., Probing the Electromagnetic Field Distribution within a Metallic Nanodisk. *Small* **2011,** *7* (23), 3317-3323.

338. García-Etxarri, A.; Romero, I.; García de Abajo, F. J.; Hillenbrand, R.; Aizpurua, J., Influence of the tip in near-field imaging of nanoparticle plasmonic modes: Weak and strong coupling regimes. *Physical Review B* **2009,** *79* (12), 125439.

339. Habteyes, T. G.; Dhuey, S.; Kiesow, K. I.; Vold, A., Probe-sample optical interaction: size and wavelength dependence in localized plasmon near-field imaging. *Opt. Express* **2013,** *21* (18), 21607-21617.

340. Schmid, T.; Messmer, A.; Yeo, B.-S.; Zhang, W.; Zenobi, R., Towards chemical analysis of nanostructures in biofilms II: tip-enhanced Raman spectroscopy of alginates. *Analytical and Bioanalytical Chemistry* **2008,** *391* (5), 1907-1916.

341. Schmid, T.; Yeo, B.-S.; Leong, G.; Stadler, J.; Zenobi, R., Performing tip-enhanced Raman spectroscopy in liquids. *Journal of Raman Spectroscopy* **2009,** *40* (10), 1392-1399.

342. Kumar, N.; Rae, A.; Roy, D., Accurate measurement of enhancement factor in tip-enhanced Raman spectroscopy through elimination of far-field artefacts. *Applied Physics Letters* **2014,** *104* (12), 123106.

343. Jiménez Sandoval, S.; Yang, D.; Frindt, R. F.; Irwin, J. C., Raman study and lattice dynamics of single molecular layers of MoS_2 *Physical Review B* **1991,** *44* (8), 3955-3962.

344. Rodriguez, R. D.; Anne, A.; Cambril, E.; Demaille, C., Optimized hand fabricated AFM probes for simultaneous topographical and electrochemical tapping mode imaging. *Ultramicroscopy* **2011,** *111* (8), 973-981.

345. Zitzler, L.; Herminghaus, S.; Mugele, F., Capillary forces in tapping mode atomic force microscopy. *Physical Review B* **2002,** *66* (15), 155436.

346. Barcons, V.; Verdaguer, A.; Font, J.; Chiesa, M.; Santos, S., Nanoscale Capillary Interactions in Dynamic Atomic Force Microscopy. *The Journal of Physical Chemistry C* **2012,** *116* (14), 7757-7766.

347. Rodriguez, R. D.; Lacaze, E.; Jupille, J., Probing the probe: AFM tip-profiling via nanotemplates to determine Hamaker constants from phase–distance curves. *Ultramicroscopy* **2012,** *121*, 25-30.

348. Zhang, X.; Qiao, X.-F.; Shi, W.; Wu, J.-B.; Jiang, D.-S.; Tan, P.-H., Phonon and Raman scattering of two-dimensional transition metal dichalcogenides from monolayer, multilayer to bulk material. *Chemical Society Reviews* **2015,** *44* (9), 2757-2785.

Acknowledgements

All my effort would not be complete without the contribution, support and inspiration from people who have been indifferent to me all this time.

Foremost, I would like to thank my supervisor, Professor Dr. Dr. h. c. Dietrich R. T. Zahn for granting me the opportunity to work under his supervision in the group of Semiconductor Physics. I am grateful for his guidance, advice, patience, and all-important teaching of ethics in science. I cordially thank him to trust on me and give me the chance to achieve my dream.

I would like to thank Professor Dr. Raul D Rodriguez, my Master thesis mentor for all his guidance, knowledge sharing and technical help which helped me a lot to prepare myself to take this challenge.

I would like to thank my former colleague Ashutosh Mukherjee for his insights in COMSOL simulation and useful discussion about the simulation results.

I would like to thank Dr. Volodymyr Dzhagan for enduring all of my important or silly scientific questions and answer with a big smile.

I would like to thanks Dr. Jacek Gasiorowski for all fruitful discussions and scientific debates which enriched my knowledge and helped to organize my experiments.

I would like to thank my external collaborators, Professor Alexander G. Milekhin, Tobias Korn, Profesor Olivia Pulci and Professor Sibylle Gemming for their kind support.

I would like to thank former colleague Stefan Moras for his insights into plasmonics and hands on training on sample preparation.

I would like to thank my funding agencies, German Science Foundation DFG via KO3612/1-1, the Research Units Zwillingpolymersation FOR1497, and the Cluster of Excellence “Center for Advancing Electronics Dresden” (cfaed)

I thank my all present and former colleagues in Semiconductor Physics who contributed to my efforts, by knowledge sharing, technical support and keeping a friendly enjoyable workplace

Finally, I would like to thank my family, my parents who have a big contribution in all of achievements, their endless support, patience, trust and letting me to run after my dreams.

Lastly, to my wife, Fatema Tuz Zohra, for sacrificing her wishes and letting me fulfil this achievement. I owe her every single moments of her loneliness.

Lebenslauf

Mahfujur Rahaman

Education

- **Since December 2014 – PhD candidate**

  Semiconductor Physics, Institute of Physics, Chemnitz University of Technology, Chemnitz, Germany

- **October 2011 – November 2014 – Master of Science (M. Sc.)**

  Micro and Nano System, Chemnitz University of Technology, Chemnitz, Germany

- **February 2004 – July 2008 – Bachelor of Science (B. Sc.)**

  Electrical and Electronic Engineering, Chittagong University of Engineering and Technology, Chittagong, Bangladesh

- **September 2003 – Secondary education**

  City: Narshingdi, Dhaka, Bangladesh

Experience

- **Since December 2014 – Scientific employee**

  Semiconductor Physics, Institute of physics, Chemnitz University of Technology, Chemnitz, Germany

- **October 2013 – January 2014 – Internship**
  Global Foundries, Dresden, Germany

- **June 2010 – October 2011 – Engineer**
  RahimAfrooz Batteries Ltd. Dhaka Bangladesh

Awards

- **Young Scientist Award – in EMRS Spring meeting 2015**

Publications

[1] A. G. Milekhin, M. Rahaman, E. E. Rodyakina, A. V. Latyshev, V. M. Dzhagan, and D. R. T. Zahn, "Giant Gap – Plasmon Tip-Enhanced Raman Scattering of MoS_2 Monolayers on Au nanoclusters Arrays, *Nanoscale, 10, (2018), 2755*.

[2] M. Rahaman, R. D. Rodriguez, G. Plechinger, S. Moras, C. Schüller, T. Korn, and D. R. T. Zahn, "Highly Localized Strain in a MoS_2/Au Heterostructure Revealed by Tip-Enhanced Raman Spectroscopy", *Nano Letters, 17, (2017), 6027*

[3] M. Rahaman, R. D. Rodriguez, M. Monecke, S. A. Lopez-Rivera, D. R. T. Zahn, "GaSe oxidation in Air: From Bulk to Monolayers", *Semiconductor Science and Technology, 32, (2017), 105004*

[4] V. N. Bliznyuk, J. Gasiorowski, A. A. Ishchenko, G. V. Bulavko, M. Rahaman, K. Hingerl, D. R. T. Zahn, "Photovoltaic cells based on ternary P3HT:PCBM:polymethine dye active layer transparent in the visible range of light", *Applied Surface Science 389 (2016), 419*

[5] L. Kaβner, A. Knoblauch, A. Seifert, R. E. Grützner, G. Cox, A. Lange, S. Csihony, F. Simon, S. Anders, L. Kroll, M. Rahaman, D. R. T. Zahn, L. Mertens, M. Weber, M. Mehring, S. Spange, "Nanostructured Aniline Formaldehyde Resin/ Polysilazane Hybrid Materials by Twin Polymerization", *Macromolecular Chemistry and Physics, 217 (2016), 2462*

[6] R. D. Rodriguez, E. Sheremet, M. Nesterov, S. Moras, M. Rahaman, T. Weiss, M. Hietschold, D. R. T. Zahn, "Aluminum and Copper Nanostructures for Surface-enhanced Raman Spectroscopy: A One-to-one Comparison to Silver and Gold", *Sensors and Actuators B: Chemical, Just Accepted manuscript,* https://doi.org/10.1016/j.snb.2018.02.006

Manuscripts under preparation:

[1] M. Rahaman, A. G. Milekhin, A. Mukherjee, E. E. Rodyakina, A. V. Latyshev, V. M. Dzhagan, and D. R. T. Zahn, "The role of a plasmonic substrate on the enhancement and spatial resolution of tip-enhanced Raman scattering"

[2] M. Rahaman, C. Wagner, A. Mukherjhee, S. Gemming, and D. R. T. Zahn, "Probing interlayer excitons in a vertical van der Waals p-n junction using scanning probe microscopy"

[3] M. Rahaman, M. Bejani. G. Salvan, S. A. Lopez-Rivera, O. Pulci, F. Bechstedt, and D. R. T. Zahn, “Vibrational Properties of GaSe: a Layer Dependent Study from Experiments to Theory”

Erklärung

Ich erkläre, dass ich die vorliegende Arbeit selbständig und nur unter Verwendung der angegebenen Literatur und Hilfsmittel angefertigt habe.

Februar 2018

M.Sc. Mahfujur Rahaman